UNIVERSITÀ
DEGLI STUDI
DI PADOVA

Sede Amministrativa: Università degli Studi di Padova

Dipartimento di Fisica ed Astronomia “Galileo Galilei”

SCUOLA DI DOTTORATO DI RICERCA IN: Scienza ed Ingegneria dai Materiali
INDIRIZZO: Unico
CICLO: XXVII°

DOPING OF GERMANIUM BY ION-IMPLANTATION AND LASER ANNEALING IN THE MELTING REGIME

Direttore della Scuola: Ch.mo Prof. Gaetano Granozzi
Supervisore: Prof. Enrico Napolitani
Co-supervisore: Prof. Davide De Salvador

Dottorando: Ruggero Milazzo

To Gelindo

Doping of Germanium by ion-implantation

and Laser Annealing in the melting regime

Ruggero Milazzo

Ph.D. Thesis – University of Padova

Printed the 2nd of February 2015

Es ist nicht das Ziel der Wissenschaft,

der unendlichen Weisheit eine Tür zu öffnen,

sondern eine Grenze zu setzen dem unendlichen Irrtum.

(Leben des Galilei - Bertold Brecht)

This work has been carried out at the *Department of Physics and Astronomy of Padova* (Italy) in association with *Institute of Microelectronics & Microsystems* (IMM) within the *National Research Council* (CNR-IMM), and in collaboration with several CNR-IMM units, namely IMM MATIS-Catania University, IMM-Catania Headquarters, IMM-Rome, and with the *Institut Matériaux Microélectronique Nanosciences de Provence* (IM2NP) unit within the *National Center for Scientific Research* (CNRS) of Marseille (France).

ABSTRACT

Germanium is the main candidate for replacing silicon in active regions in future complementary metal-oxide transistors (CMOSs) devices due to: (i) its higher mobility of charge carriers that makes it able to attain higher drive current;[Clays2007, Pillarisetty2011] (ii) the availability of high-k materials, excellent substitutes for unstable GeO_2[Clays2007, Simoen2012] and (iii) its lower melting point that allows lower processing temperatures.[Clays2008] However, a downscaling beyond 15-nm necessarily requires higher doping levels (higher than $1\times10^{20}cm^{-3}$) beyond the solid solubility of most of the dopants.[ITRS2013] In particular, *n*-type ultra-shallow junctions (USJs) are the most challenging, because of the lower solid solubility and higher diffusivity of V-group elements in Ge[Simoen2006] which make the required shallow doping profiles hard to achieve.

For these reasons, laser thermal annealing (LTA) in the melting regime is a promising advanced activation technology of implanted dopants in Ge for USJs formation.[ITRS2013] In fact, it has a potential capability of increasing the dopant solubility as well as of confining the diffusion processes into the molten layer, whose depth can be controlled by choosing adequate energy density in turn.[Poate1982] Thanks to this technique, donor concentration far exceeding the theoretical maximum solid solubility limits after LTA in Ge are reported in literature for implanted phosphorous[Heo2006] and antimony,[Bruno2012] pushing the doping limits for these systems above to $1\times10^{21}cm^{-3}$.

Despite the above encouraging results, melting LTA on Ge doped with arsenic as well as with acceptors was still unexplored. Therefore, the aim of this work was the investigation of the LTA process applied to both the *n*-type and *p*-type doping of Ge after As or boron implantation. In particular, experiments on diffusion, contamination, thermal stability, residual strain and clustering were performed in order to study mechanisms influencing the resulting electrical activation.

RIASSUNTO

Il germanio è il principale candidato a sostituire il silicio come substrato per i futuri dispositivi elettronici ultra-scalati, poiché: (i) la sua superiore mobilità di portatori di carica consente correnti maggiori;[Clays2007,Pillarisetty2011] (ii) la possibilità di crescere ossidi alternativi ad alta capacità dielettrica (high-k), consente di aggirare i problemi legati all'ossido nativo[Clays2007, Simoen2012] e (iii) la sua minore temperatura di fusione lo rende più facilmente processabile. [Clays2008] Tuttavia, miniaturizzazioni che soddisfano i futuri nodi tecnologici (in particolare al di sotto dei 15-nm) necessariamente richiedono livelli di drogaggio più alti di $1\times10^{20}cm^{-3}$, oltre cioè le solubilità solide della maggior parte dei droganti. In particolare, le più problematiche sono le giunzioni ultra-sottili (USJ) di tipo-*n*, date le basse solubilità e le alte diffusività degli elementi del V gruppo in Ge[Simoen2006] che rendono gli alti livelli di drogaggio richiesti ardui da ottenere.

A questo scopo, il laser thermal annealing (LTA) in regime di fusione rappresenta una promettente avanzata tecnologia di attivazione elettrica dei droganti impiantati,[ITRS2013] data la sua potenziali capacità di aumentare le solubilità dei droganti, conseguente alla rapidissima ricrescita epitassiale da fase liquida indotta (LPER), e di confinare i processi diffusivi nella regione liquefatta, la quale viene a sua volta controllata, modulando opportunamente la densità d'energia.[Poate1982] Grazie a questa tecnica si sono infatti ottenute in Ge concentrazioni attive che superano ampiamente le rispettive solubilità solide, sia di fosforo impiantato[Heo2006] che di antimonio[Bruno2012] dove si è ottenuto l'impressionante record di $1\times10^{21}cm^{-3}$.

Nonostante questi incoraggianti risultati, il LTA nel caso di Ge drogato con arsenico o con accettori non è stato ancora sperimentato. Inoltre, quanto si impiantano grandi fluenze di droganti, si ottengono solo parziali attivazioni elettriche e una profonda comprensione della fenomenologia che avviene durante una così estrema LPER è ancora mancante. Perciò, lo scopo di questo lavoro è stato lo studio del processo di LTA applicato sia per drogaggio di tipo-n che –p di Ge dopo l'impianto di arsenico o boro. In particolare si sono svolti esperimenti svolti sulla diffusione, contaminazione, stabilità termica, stato di deformazione residuo e formazione di clusters al fine di studiarne l'influenza sulla attivazione elettrica risultante.

CONTENTS

INTRODUCTION

The replacement of silicon with an higher mobility substrate would allow further downscaling of electronic devices, with advantages in terms of higher performance as well as improved energy efficiency. For this reason, there has been a renewed interest in germanium in recent years, which is promising both for *n*- and *p*- type carriers, compared with Si. Nonetheless, the future technology nodes for Ultra-Shallow Junctions (USJs) essentially require the fulfillment of doping level higher than solid solubility limit, as specified by the International Technology Road Map for Semiconductors (ITRS).

Among different approaches, ion-implantation followed by melting laser thermal annealing (LTA) is studied as a technique capable of introducing an high quantity of dopants and to potentially increase their electrical activation. The LTA technique consists of irradiating the implanted sample with a pulsed laser beam, so that the surface layer is melted to a depth controlled by the laser pulse energy. In this way, an homogeneous redistribution of dopants confined within the molten layer can be obtained, because of the order of magnitude larger diffusivity in the liquid with respect the solid phase. Then, the rapid (~m/s) Liquid Phase Epitaxial Regrowth (LPER) results in the formation of high quality crystalline material with a high fraction of dopant incorporation.

Thanks to this method, metastable Ge layers with carrier concentrations well above the solid solubility have been already demonstrated for phosphorus and antimony, even though those systems results only partially active and the understanding of limiting mechanisms is lacking. In particular, little is known on several crucial phenomena such as the formation of residual defects, the junction stability upon further processing, and the comprehension of the basic phenomena occurring during LTA of Ge that govern dopant diffusion and electrical activation.

Therefore, a complete study about ion-implantation and subsequent melting LTA of Ge doped with unexplored elements, i.e. arsenic and boron, is presented. Experiments on diffusion, contamination, thermal stability, residual strain and clustering have been performed on varying the implanted fluence (atom/cm^2) as well as the laser energy density and the number of pulses. So, the mechanisms influencing the resulting electrical activation have been characterized in a wide range of experimental conditions for both of the elements.

The research activity object of this thesis has been performed at the Dipartimento di Fisica e Astronomia of the Università di Padova, Italy where the SIMS and HRXRD laboratories are located, in association with the Istituto per la Microelettronica e i Microsistemi of the italian Consiglio Nazionale delle Ricerche (CNR-IMM). The activity have been performed in collaboration with several CNR-IMM units, namely IMM MATIS-Catania University (Ion implantation), IMM-Catania Headquarters (SRP, TEM, modelling of the melting regime) , IMM-Rome (LTA), and with the *Institut Matériaux Microélectronique Nanosciences de Provence* (IM2NP) unit within the *National Center for Scientific Research* (CNRS) of Marseille (France).

During my three years of Ph.D., I started by investigating B-doping of Ge by LTA where I participated to the SIMS measurements and carried out the data analysis, discussion and interpretation of results. In addition, I proposed and carried out all the HRXRD characterization and their analysis. Afterwards, I actively contributed in designing the experiments on arsenic, and participated to SIMS and performed myself HRXRD measurements. Moreover, I analyzed all the collected data from the different techniques, which I combined with kinetic considerations to reach a consistent interpretation. Finally, I carried out the thermal stability experiments performed in-situ by HRXRD.

This thesis is organized as following.

Chapter 1 briefly reviews the features that make germanium an attractive material for the progress of devices. The principal issues on the high doping are introduced, namely solid phase dopant diffusion and clustering, and the state of the art about Ge doping is reviewed, with focus on the benchmarks for B and As in Ge. The proposed solution of LTA is then presented with focus on the melting regime, and on the main advances in the laser annealing for junction formation technology, which has been mainly investigated on Si, but that represents the starting point which inspired this work.

In chapter 2, the sample preparation as well as the characterization techniques are described.

The chapter 3 reports the description of the five main experiments performed in this study. Namely on the diffusion as well as on the activation of B induced by LTA, on the analogous mechanisms for

As, on the dopant-oxygen correlation, on the residual strain characterization and on the thermal stability.

In chapter 4 all the results obtained will be summarized and some perspective will be given for future work and possible implementation of LTA in junction fabrication processes for advanced scaled Ge-based devices.

Finally, in appendix, an experiment aimed at investigating the self-diffusion of silicon under melting laser annealing is described as being a study that I contributed to design during the Ph.D. Such experiment is still work-in-progress , the sample have been grown and processed and only preliminary characterizations are available

I presented those results with oral contributions to the following conferences: European Material Research Society (EMRS) Spring Meeting 2013 – Symposium K "*N-type Doping of Ge by As Implantation and Excimer Laser annaling" where I have been awarded with the prize....*; the International Conference on Diffusion in Materials (DIMAT) 2014 "*Dopant diffusion and electrical activation in Ge during pulsed melting laser thermal annealing"*; the 19th International Conference on Ion Beam Modification of Materials 2014 "*Ge doping by ion implantation and melting Laser Thermal Annealing"* and the Nanotechnology Materials and Devices Conference (IEEE-NMDC) 2014 "*Dopant diffusion and activation in Ge by ion implantation and pulsed melting Laser Thermal Annealing"*.

CHAPTER 1

BACKGROUND AND STATE OF THE ART

1.1 Germanium as higher mobility substrate

Germanium is the first semiconductor that was used in the first field-effect transistors in 1948 and it has been the workhorse substrate for bipolar devices till late of '50s.[Simoen2007] Thereafter, it was taken over by silicon in planar Metal-Oxide Field-Effect Transistors (MOSFETs)[Kahng1991] (fig.1.1), because of the better native oxide passivation employed in the gate.[Atalla1959, Prabhakaran1995]

Since early '60s, silicon has become the dominant material in semiconductor industry and the improvements in manufacturing has brought Si-based devices to a continues miniaturization. From then on, the number of transistors on integrated circuits has doubled every 2 years according to the 'so called' Moore law, up to over than 1 billion nowadays. As a result, modern integrated circuits operate with clock frequencies several order of magnitude higher than the early microprocessors.[Moore2003]

Among the latest improvement steps, the introduction of high-κ materials in 2007 allowed to meet the 45-nm technology node (i.e. half the distance between identical features in the array of transistors).[Mistry2007] The replacement of SiO_2 with those higher dielectric constant materials in the gate provided higher scalability and performances of Si-based solid-state devices, but also renewed the interest in germanium as it allows to overcome issues concerning its native oxide. In the latter way, i.e. replacing Si with Ge, transistors could be further downscaled or improved by reducing power consumption. In fact, Ge is able to attain higher drive currents between source and drain due to its superior carrier mobility μ, which is the highest of all the know *p*-doped semiconductors [Pillarisetty2011] (see fig.1.2), as well as it is compatible with already existing Si-based technology. Last but not least, Ge has lower melting temperature (1211K) than Si (1687K), which allows faster and less-consuming production steps.

However, a complete non-silicon Ge-based MOSFET has not been achieved yet in production, even though considerable research progresses has been made recently by industry and academia towards germanium integration on Si technology. This is essentially because the knowledge of many fundamental properties of Ge is still lacking, for example dopant-defects interactions are less understood as compared with silicon. As it will discussed in the following chapter, these features are crucial in order to form well-defined and highly-doped Ultra Shallow Junction (USJ), i.e. regions forming source and drain.

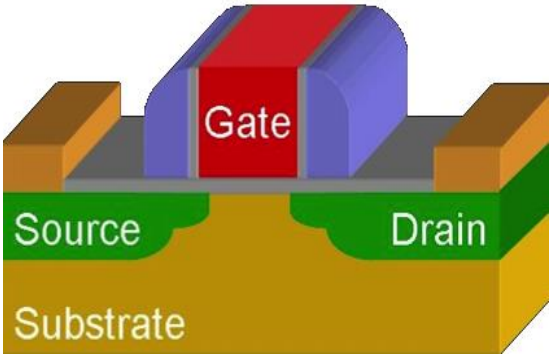

Fig.1.1 Schematic of a MOSFET.

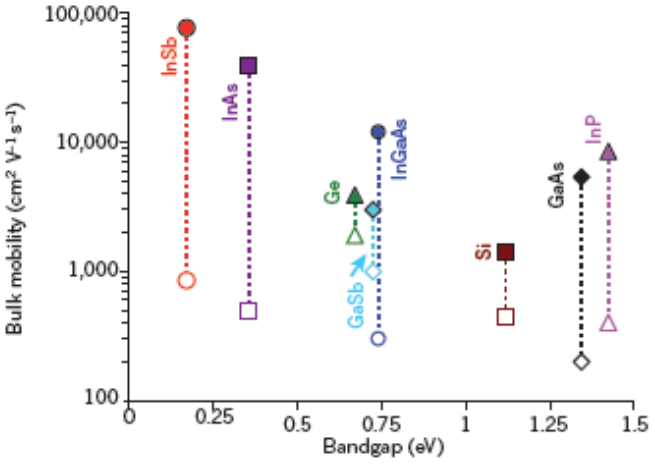

Fig.1.2 Bulk n- (closed symbols) and p-type (open symbols) mobility as function of band-gap for Si (wine), Ge (greed) and III–V materials (others).

In particular, the important technological parameter that needs to be minimized is the sheet resistance R_s associated to USJs, that can be expressed as:

$$R_s = \frac{1}{\int_0^{x_J} q\mu N_{active}(x)dx} \qquad (1.1)$$

where q is the carrier charge, $N_{active}(x)$ is their active concentration profile and x_J is junction depth, which is the thickness of source and drain. From the formula above, one can easily derive the advantage of using higher mobility substrate, so providing lower R_s. Besides, the maximum electrical activation is often used to compare different USJ fabrication techniques, since this quantity is independent upon x_J itself. Still, it is a poor metric when comparing junctions in different materials, as the relevant quantity is R_s., that depends not only on the carrier concentration but also on their mobility. For that reason, the state of the art on Ge-based USJs obtained with different techniques are reviewed using R_s-x_J plots hereinafter.

1.2 Issues on Ge-doping

In order to fulfill the requirements for USJs, dopants are usually introduced by ion-implantation at concentrations exceeding the solid solubility as well as shallow profiles by suitable combination of energy and incidence angle. Subsequently, a post-implantation annealing step is necessary for dopant activation and damage recovery. Germanium is a good candidate for the replacement of silicon, but the fabrication of USJs on a Ge substrate appears to be problematic, in particular concerning n+/p junctions.

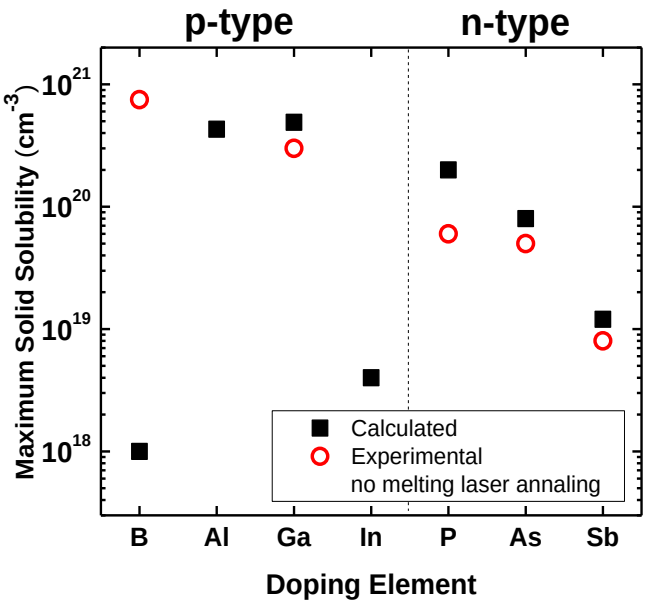

Fig.1.3 Maximum active concentrations experimentally obtained (open circles) and calculated[Fistul2004] (closed squares) maximum solid solubility of *p*- and *n*-type dopants in germanium.

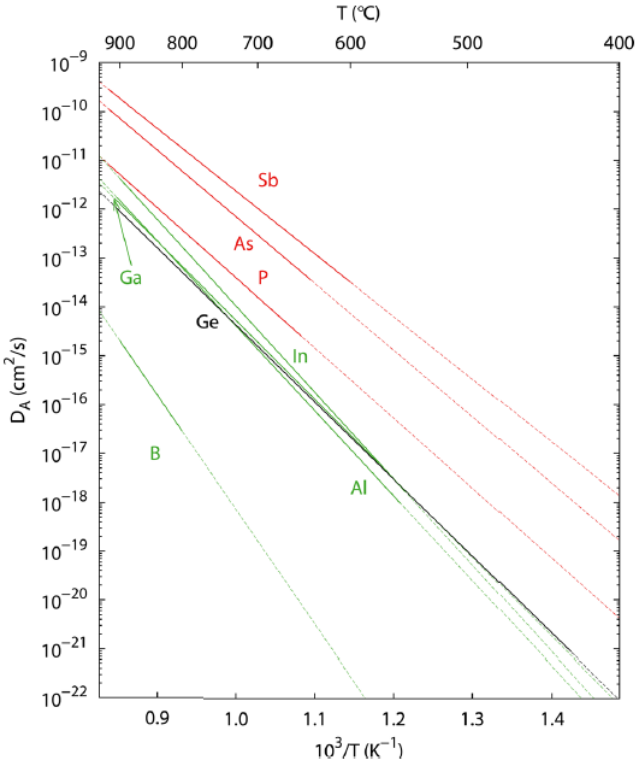

Fig.1.4 Equilibrium diffusion coefficients of the *n*-(red lines) and *p*-type dopants (green lines) in Ge compared the self-diffusion (black line) as function of temperature. Solid and dashed lines span experimental and extrapolated range respectively. [Chroneos2014]

One issue is related with the solubility of dopants (fig.1.3). The solubility of impurities in a solid phase is defined as the maximum (or saturation) concentration of that impurity in thermodynamic equilibrium with the liquid phase of the matrix where it is dissolved. This equilibrium between the crystal and its melt is function of the temperature and it is described by the distribution or segregation coefficient *k*:

$$k = \frac{C_S}{C_L} \qquad (1.2)$$

where C_S and C_L are the impurity concentrations in the solid and in the melt, respectively. The solubility in the liquid phase is nearly always higher. Therefore, a value of k=1 means complete impurity incorporation in the crystal, while k<1 implies preference for the melt. From atomic point of view, *k* is influenced by the covalent (or ionic) radius of the solute and according to the different Groups in the periodic table.[Trumnore1960]

The maximum equilibrium solubility of dopants[Fistul2004] is relatively high for acceptors, with value close to 5×10^{20}cm^{-3} for Al and Ga, except for B which has a maximum solubility around 1×10^{18}cm^{-3}. However, by moving from equilibrium, through amorphization by ion-implantation followed by solid phase epitaxy (SPE), the solubility (metastable) of B can be increased well beyond C_S,[Impellizzeri2009, Mirabella2008] as shown in fig.1.3, and as discussed more deeply in the following section. The solubility of donors is in general lower than for acceptors, with P and As having values of ~2×10^{20}cm^{-3} and ~8×10^{20}cm^{-3}, respectively, and Sb having a significant lower value of slightly higher than 1×10^{19}cm^{-3}. In addition, donor-V pairing at high dopant concentrations, as discussed below, promotes dopant clustering that further limits the achievement of the high active donor levels required by future CMOS technology.

Vs mainly mediate the diffusion of both acceptors (*p*-type dopants) and donors (*n*-type ones) in Ge under thermal equilibrium, as determined by self-diffusion experiments[Werner1985] as well as by Density Functional Theory (DFT) calculations. This is expressed by lower formation energy of Vs with respect to Is. Nonetheless, *p*-type dopants exhibit comparable diffusion activation enthalpy with respect to self-diffusion[Hüger2008] as displayed by their more pronounced slope in fig.1.4. In this landscape, boron diffusion in Ge makes exception, being significantly slower than self-diffusion,[Uppal2001] owing to an interstitial-mediated mechanism.[Napolitani2010] The lower diffusion of acceptors, and of B in particular, is very promising for *p*-type USJ formation.

On the contrary, shallow profiles and high electrical activation of donors in Ge are prevented both by their quick diffusion and also clustering with vacancies, due to their stronger Coulomb interaction. Indeed, doubly negatively charged V^{2-} prevails under *n*-type extrinsic condition and diffusion and clustering of a substitutional donor A_s^+ can be respectively described by the following reactions:

$$A_s^+ + V^{2-} \rightleftarrows AV^- \qquad (1.3)$$

$$AV^- + A_s^+ \rightleftarrows A_2V^0 \qquad (1.4)$$

where AV^- is the mobile pair mediating the diffusion and A_2V^0 the lowest order inactive cluster.

At variance with Si, where the donor dependence of diffusion increases linearly with *n*,[Bracht2007] intrinsic diffusion $D_A(n_i)$ of the donor A={P, As, Sb} under equilibrium conditions results increased by the square of free/intrinsic carrier ratio (n/n_i) in extrinsic conditions:[Brotzmann2008]

$$D_A(n) = D_A(n_i) \cdot \left(\frac{n}{n_i}\right)^2 \qquad (1.5)$$

In the case of As diffusing in germanium, these parameter respectively are:[Brotzmann2008, Morin1954]

$$D_{As}(n_i) = 32^{+21}_{-13} \exp\left[-\frac{(2.71 \pm 0.06)eV}{k_B T}\right] \mathrm{cm}^2/\mathrm{s} \qquad (1.6)$$

$$n_i = 7.3^{+5.4}_{-3.1} \times 10^{20} \exp\left[-\frac{(0.44 \pm 0.05)eV}{k_B T}\right] \mathrm{As/cm}^3 \qquad (1.7)$$

where k_B is the Boltzmann constant and T the temperature.

From the (1.5) it results that for high dopant concentrations, the formation of AV^- and also the encounter probability with A_s^+ is increased. As a consequence both excessive diffusion and clustering or direct deactivation becomes more relevant, according to the mechanisms described by reactions (1.3) and (1.4). This is experimentally observed by deviation of the chemical dopant profiles as expected by the (1.5), and by maximum electrically active concentrations for *n*-type dopants always significantly lower than their equilibrium solid solubility after conventional annealing processes (fig.1.3).

Moreover, if stable, higher order A_mV_n clusters can grow when additional AV^- pairs join. The formation of such high order clusters is favored by slow cooling from high temperatures or low temperature annealing. In principle, either interaction between AV and V would lead to dopant-defect complexes, and thus to indirectly donor deactivation via (1.3). However, the formation AV_2 is unlikely because of the Coulomb repulsion between the mobile pair and vacancies.

Last but not least, another issue is the dopant loss during thermal annealing, giving rise to a lower active doping concentration and so to higher R_s. It has been shown for phosphorous that the dopant loss is mediated by the ion implantation damage[Poon2005], so that damage removal is a universal key to achieve highly activated junction.

In conclusion, dopant-defect interactions enhance diffusion in extrinsic regime and favor electrical deactivation, which are highly detrimental for highly-doped USJ fabrication in Ge. For this purpose, high temperatures and sort times annealing are used to inhibit reactions (1.3) and (1.4).

1.3 Benchmarking results on Ge-doping

The renewed interest in Ge as high mobility substrate has corresponded to new studies on junction formation by ion-implantation.[Chui2003, Satta2005] As discussed above, as higher and shallower the active profile is wanted, as faster the annealing process must be. This chapter aim at giving an overview of the current state-of-the-art of shallow junction processing in Ge, defects removal, x_J control and of the records achieved in activation, with particular emphasis about the dopant used in this work: boron and arsenic.

In the case of acceptors, early experiments already pointed out that the implantation of B could be successful for standard p^+n junctions.[Jones1981] This is related to its lowest diffusivity in Ge, as discussed above, but also to the favorable dynamic defects annealing and activation taking place already during implantation at low fluences ($\lesssim 10^{14}$B/cm^2).[McDonald1975] Boron, due to its low solubility, upon implantation at subamorphizing doses show relatively low activation levels.[Satta2005] Indeed, the application of the so-called rapid thermal annealing (RTA) to B implants is sufficient to yield good R_s values, corresponding to electrical activation well above the maximum solid solubility (few times of 10^{20}B/cm^2) and junction depth of ~150nm.[Chui2003] Moreover, the low R_s so obtained is very stable: negligible diffusion after FA at 600°C for 3h is observed.[Suh2005]

A further improvements in fabrication of *p*-type junction can be achieved by the use of Ge pre-amorphization implant (PAI), which results in shallower as-implanted profiles due to channeling suppression and it also removes the stable extended defects observed after high-dose implantation at the amorphous/crystalline (a/c) interface.[Satta2005] It indicates that the non-equilibrium solid solubility in pre-amorphized is much higher than in crystalline Ge (c-Ge). In fact, the highest activation level has been achieved up to ~6×10^{20}B/cm^2 whereby PAI is followed by solid-phase epitaxial regrowth (SPER) induced by FA.[Mirabella2008] However, 100% of activation was not achieved likely because of impurity scattering from residual defects, which are found to be significantly stable for 1h at 550°C.[Impellizzeri2009] The tested stability demonstrates that the B clustering, responsible of B inactivity, is characterized by high binding energies and clearly, higher thermal budget annealing are needed in order to eliminate this damage properly and to improve USJ formation. In the same study, slightly lower activation level (~5.8×10^{20}B/cm^2) with respect to PAI+SPE method is obtained by testing B-implantation at liquid nitrogen temperature (~77K), in order to suppress the damage

annealing during the implantation. In this way amorphous pockets are formed, so favoring nearly complete activation, through their regrowth process.

In summary, the best results for B-doped junction with depth from 60 to 120nm are reported in fig.1.5 using R_s-x_J plots together with the ITRS targets for the 45, 32 and 22nm nodes.

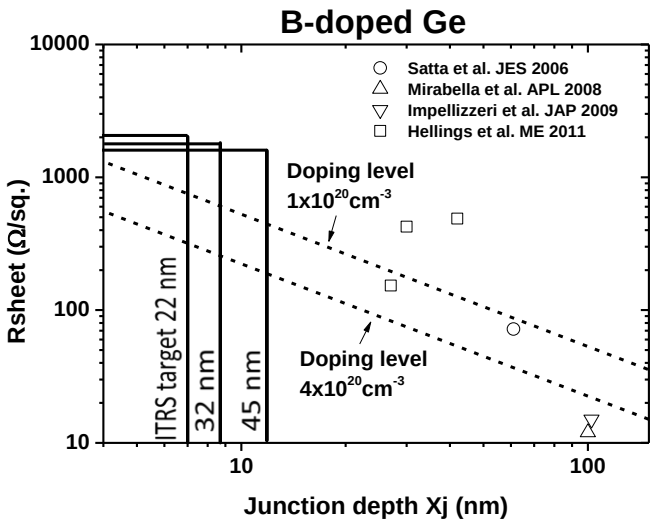

Fig.1.5 Sheet resistance as function of junction depth for B-doped Ge. Trend lines for ideal box-like profiles are added with ITRS targets for the 45,32 and 22nm nodes

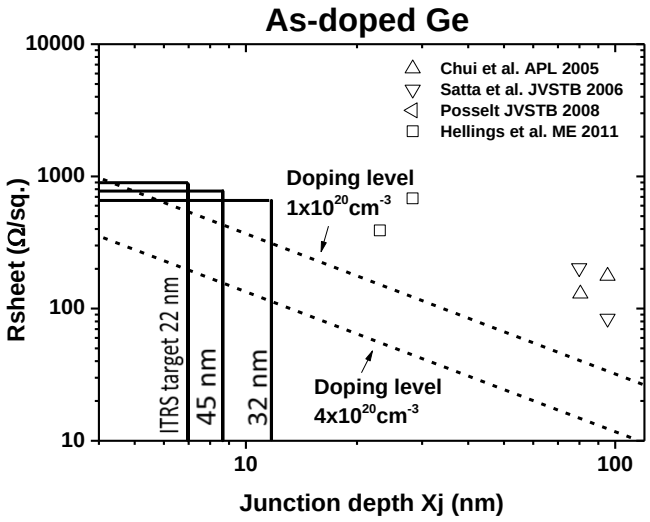

Fig.1.6 Sheet resistance as function of junction depth for As-doped Ge. Trend lines for ideal box-like profiles are added with ITRS targets for the 45,32 and 22nm nodes

On the contrary, the formation of shallow *n*-type junctions is more challenging due to lower solubility and high diffusivity of donors. The implantation of n^+p junction suffers of several problems. Due to their heavier mass compared with B, the damage is much more pronounced, henceforth much more difficult to remove. For practical implantation fluence ($\gtrsim 10^{13}cm^{-2}$), P, As and Sb will lead to an amorphized top layer of the germanium and residual defects remain up to about 450°C, independently of the implanted dose.[Benourhazi1992] In addition, the damaged after high-fluence implants results in deep voids formation that cannot be repaired, especially if high-mass element such as Sb are used. The only way to prevent void agglomeration is by performing implantation above 300°C, so that no amorphous region is formed.[Romano2013] Similarly, in the case of As implantation a surface roughness is seen, but no void formation. Adding a cap layer removes the surface roughness.[Janssens2006]

Another problem suffered by *n*-type doped Ge, especially with P and As, is the dopant loss during subsequent thermal annealing by evaporation (out-diffusion) from the surface during conventional FA annealing. In contrast with P, Arsenic tends to out-diffuse up to 50% even with a 40nm SiO_2 cap,[Impellizzeri2011] thus preventing full activation.

Because of those problems, arsenic is the less studied dopant of Ge among the donor and the record of activation up to about 1×10^{19}As/cm^3 established in 1988[Hattangady1988] lasted for years, in spite of its one order of magnitude higher solid solubility. In this early work, it was showed that it is possible to activate nearly 100% of low fluence of As implanted in Ge by a dual process: 430°C-FA/650°C-RTA. However, achieving higher active concentrations is difficult for the reasons of high diffusivity and increasing interaction with vacancies promoting clustering, as discussed above. Recently, encouraging results are obtained by means of non-melting laser annealing to induce very rapid SPE in As-implanted into Ge covered with 2nm-deposited SiO_2 after PAI. In this way an active As concentration of 4×10^{19}As/cm^{-3} was achieved without significant out-diffusion, although the activation is only around 30%. Before the present thesis work, this was the highest activation record of As in Ge.

Instead, there have been studies using a single pulse of melting laser on P-doping through a PH_3 plasma[Heo2006] and on Sb-implant at 50keV, 6.4×10^{15}Sb/cm^2 at 300°C and subsequent PAI[Bruno2012] testing single and multi-pulse regimes. For both of the systems melting LTA succeeded in obtaining the highest activation ever, corresponding to 4×10^{20}P/cm^2 and 1×10^{21}Sb/cm^2 respectively. Although, the impressive record for Sb displays an overall activity lower than 50%, with deactivation in the deeper part of the original melt depth, again attributed to dopant-vacancy interactions. Last but not least, it is interesting to note that LTA provided solution simultaneously to out-diffusion of P, which results lower than 20% without capping,[Tsouroutas2009], and to recovery of voids defects, formed after Sb-implantation high-fluence implantation.[Bruno2010]

In summary, the records for As junction with depth from 60 to 120nm are collected in fig.1.6 using R_s-x_J plots, analogously to what was done for B. If the best values of R_s obtained so far for *n*- and *p*-junctions in Ge are compared, it is evident that particularly for the n^+-implantations there is still quite some work to do, especially if the future ITRS node of 15nm wants to be matched.

1.4 Laser annealing in the melting regime

A potential candidate to overcome the above issues and fulfill USJ requirements as well as high electrical activation is the pulsed Laser Thermal Annealing (LTA) in the melting regime. LTA is an advanced annealing technique employing a laser as a heat source, which allows to melt the substrate with a precise spatial and temporal control. The first demonstration of laser irradiation benefits came from the annealing of silicon implantation damage performed by soviet scientists in 1974. Thereafter, the term "laser annealing" was coined, but also its capability of semiconductor doping, processing and surface modification has been demonstrated in the past years. Indeed, a rapid heating and cooling of a chosen superficial layer is promoted depending on the pulse duration τ and absorption depth α^{-1} i.e. the reciprocal of optical absorption α which depends on the materials and on the wavelength. For example, the coupling to an amorphous or a crystalline target is different. A scheme of temperature distribution in planar geometry is reported in fig.1.7, where the laser annealing condition (absorption length thinner than characteristic diffusion one, i.e. opposite to the ablation regime) is satisfied:

$$\alpha^{-1} < \sqrt{2D_H \tau} \qquad (1.8)$$

here D_H refers to the diffusivity of heat dissipated into the solid substrate.

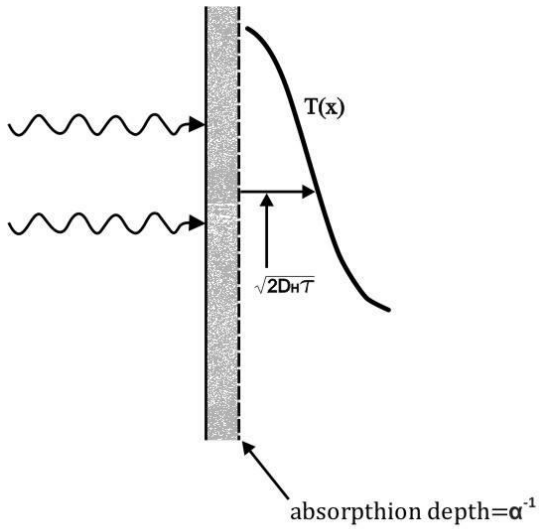

Fig.1.7 Temperature distribution in LTA experiment, where absorption length α^{-1} is less than the heat diffusion one $\sqrt{2D_H \tau}$.

In particular, if nanosecond pulse UV laser is used on semiconductors, surface melting and solidification in exceedingly short times (hundreds of nanoseconds) is promoted. To be more precise, UV light efficiently transfers a large amount of energy to the lattice, because it induces electronic excitations toward an high level of the conduction band, from where decay on the order of ~ps occurs by means of intra-band transitions (i.e. instantaneously for all the LTA purpose). Consequently, the threshold energy density required for melting becomes accessible by source with pulse duration on the order of ~100mJ/cm^2, as provided by heat flow calculations on Si and Ge.[Poate1982] In this case, scientists speak about LTA in the melting regime, which is of particular convenience for the purpose of doping because:

1) liquid have much higher diffusivity (10^{-5} cm^2/s) with respect to solids (10^{-12} cm^2/s), so the thickness of the processed layers is defined by the confinement of diffusion within the melt depth (which can be controlled by choosing the appropriate laser energy density in turn) and it can be chosen as required by the integrated circuits technology. Moreover, the high liquid diffusivity provides an even distribution of the dopant across that junction, especially if multiple laser pulses are used. Thus resulting in a homogeneous and well-defined box like junction;

2) the pulsed source results in extreme temperature gradient (~10^8°C/cm) at the liquid/solid (l/s) interface and consequently in a rapid solidification (~m/s). Under these pronounced non-equilibrium conditions, the trapping of impurities increases because the interface velocity v prevails over the probability to escape away from the moving front. The phenomenon is expressed by the effective segregation coefficient k_{eff}:[Wood1981]

$$k_{eff} = \frac{k_0}{k_0 + (1 - k_0)\exp(-v \cdot z_{MD} / D_l)} \qquad (1.9)$$

where k_0 is the equilibrium segregation coefficient, z_{MD} is the maximum depth of the molten layer and D_l is the impurity diffusivity in the liquid phase. Therefore, melting LTA is a unique technique for dopant incorporation at concentration far in excess of equilibrium values as well as for alloying in general;

3) the laser induced Liquid Phase Epitaxial Regrowth (LPER) efficiently suppresses preexisting defects independently on the starting conditions. Essentially high quality single-crystal materials can be produced even from deposited, amorphous or very damaged implanted layers nucleating above the substrate seeding. Either, lateral epitaxy can be exploited by shaping the melt puddle with a scanning

laser, so a complete 3D control is potentially achievable. Therefore, melting LTA is a powerful tool for engineering a variety of experimental and device geometry.

Nevertheless, disadvantages characterizing LTA still remain, so preventing its large scale industrial implementation. In particular, integration in the current process sequence to device fabrication results critical, because the gate is usually created before source and drain. In particular, melting of the gate cannot be avoided in Si-based technology due to the modality of absorption and heat diffusion as a result of irradiation, as demonstrated in series of experimental and theoretical works.[Privitera2007, LaMagnaJAP2004, LaMagnaAPL2004, Fisicaro2011] Again the different properties of Ge (e.g. lower melting point and latent heat) could open, in principle, new prospective for the use of LTA in solid-state transistors.[Fisicaro2011] However, a very localized LTA step and complete 3D control over thermal field evolution is still required, which is not trivial to attain especially in MOSFET patterned sample. Therefore, the development of suitable modeling techniques for designing LTA processing in Ge is now attracting more and more interests.

Further difficulties in LTA integration are related to its reproducibility: even small fluctuation in the irradiating energy (~mJ/cm^2) can results in significant variation in the melting depth (~nm), thus affecting the required devices properties. In addition, the lateral control of the intensity is also necessary if inhomogeneous melting of the doped region want to be avoided. Both of these problems are essentially still unsolved for the most of modern laser, although the introduction of upgrades in equipment such as beam homogenizers. So, additional efforts for improving the instrumentation are necessary.

Last but not least, another issue is the thermal stability of the carrier profiles in the USJs formed by LTA. This problem is relevant for MOSFET fabrication above all, as further temperature steps are required after junction activation. In Ge-based devices for example, germanidation takes place at 400°C typically.

1.5 Advances in melting laser annealing

Theoretical and experimental research efforts are required to complete the sill lacking physics involved in the extreme condition induced by the interaction with laser light. Among the phenomena, the transient thermal field dynamic, the kinetics of the l/s phase transition, the redistribution of dopants as well as the evolution of defects need quantitative knowledge. In particular, silicon represents the model system where the most recent experiments are tested. In fact, it is the most studied substrate, being the first material where experiments have been performed since 1974, so having the largest amount of data are available in literature.

Therefore, a selection of the most advanced theory and fundamental experiment about dopant redistribution and point-defects evolution in Si subject to LTA are reviewed in this chapter, as they inspired this thesis work about Ge. In particular, the modeling technique originally developed for Si, and used for the presented data simulation is presented. Furthermore the few fundamental studies of LTA on Ge preceding this work, are summarized.

The most effective methodology applied to simulate dopant redistribution in Si during a process of LTA in the melting regime was developed by CNR-IMM group at the University of Catania - Italy and it uses the so-called phase field approach.[LaMagnaJAP2004] This mathematical method is used to handle phase transition problems and it consists in introducing an interphase, i.e. a finite size region between the liquid and the solid phase. In this way it is possible to replace all the boundary conditions at the l/s interface with differential equations ruling the evolution of an auxiliary fields Φ (i.e. the phase field) analogous of the order parameter in the framework of the Ginsburg–Landau thermodynamic formalism. Therefore, the dynamic of the melting front can be described by three coupled equations: two of diffusion (for the dopant and the heat) and one for Φ (including all the conservation laws). The latter generally depends on spatial coordinates and on temperature. It is a continuous field varying between 0, in the liquid phase, and 1, in the solid phase, inside the interface of finite thickness *W*. A scheme is reported above in fig.1.8.

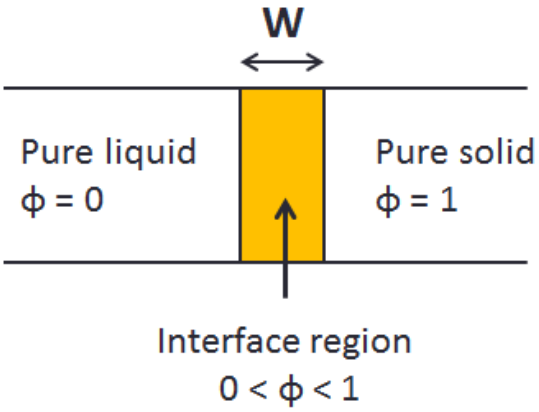

Fig.1.8 Schematic representation of the finite thickness interface (W) in the phase field methodology. Φ is the phase parameter.

It is worth noting that phase field methodology gives the resulting redistribution profile of dopants as output, once that the optical and thermal properties of the material (absorption coefficient, heat capacity, heat diffusivity) as well as the impurity-dependent diffusivity in the solid and in the liquid phase are provided. Last but least, it is noteworthy that it is very useful to numerically solve an LTA process, especially when the initial condition is an ion-implant process for instance.

Moreover, possible defect generation at the phase boundary[LaMagna2007] and the alloy non-equilibrium segregation effect can be consistently integrated in the code.[LaMagnaJAP2004, Wheeler1992] These two particular phenomena have been experimentally studied and main results, which are interest for this work, are presented hereafter.

The former was indirectly evidenced the first time in 2005, by observing a reduction up to ~25% of the interstitially mediated transient diffusion of boron[Cowern1992] in implanted Si after melting LTA.[Mannino2005] The phenomenon was attributed to an excess of vacancies induced by the rapid solidification which reduces net amount of interstitial available to the diffusion of B. Finally, the vacancy generation during fast melting and regrowth of Si as a result of laser irradiation has been conclusively demonstrated in 2007 thanks to an experiment based on positron annihilation spectroscopy.[LaMagna2007] In particular, it has been shown that the regime of vacancy generation is well separated from the regime of interstitial formation, in terms of the ratio between the l/s interface speed v_{sl} and the temperature gradient ∇T. The critical value is estimated of $(v_{sl}/\nabla T)\sim 0.1 mm^2/mink$ above which vacancies form. Since the usual LTA irradiation conditions induce a very rapid regrowth (on the order of m/s), the condition for vacancy formation are always given.

The latter mechanism, namely the non-equilibrium segregation of impurities during laser irradiation, has been studied by performing experiments on their redistribution. Among the dopants in Si, B shows anomalous behavior, namely a pile-up close to the maximum melt depth region, which emerged clearly when samples are processed with multipulses.[Monakov2005] The impurity profiles can be recovered an anomalous segregation coefficient larger than 1.[Ong2006] Recently, it has been proposed that the mechanism is linked to the property of the liquid phase of Si (l-Si), which undergoes a liquid-liquid phase transition in the undercooling regime due to its tetrahedral crystalline structure.[Fisicaro2013, and reference therein] Thus, the anomalous segregation in l-Si is explained on the basis of two (fast and slow) diffusivity states of B, correlated to the metallic and the covalent bond state, respectively. In particular, the phase-field simulations predict that the strongest undercooling region is expected close to the maximum melt depth, where the slower diffusivity state is strongly favored (fig.1.9 and fig.1.10). The first evidences of similar anomalous redistribution effects in Ge will be presented in this thesis.

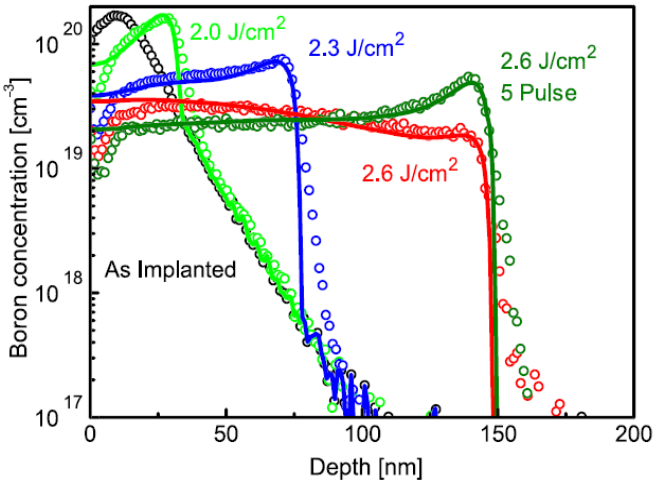

Fig.1.9 B concentration profiles obtained after single pulse laser irradiations at 2.0 (light green), 2.3 (blue), and 2.6J/cm^2 energy densities for 1 (red) and 5 pulses (dark green). Simulation with the two-state model are also reported.[Fisicaro2013]

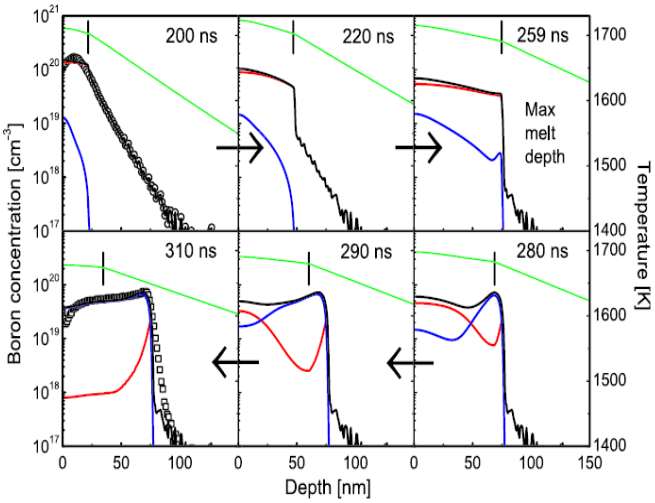

Fig.1.10 Dopant evolution during the LTA process (2.3J/cm^2). Melting and re-growth stages are indicated by the forward and the backward arrow respectively. The total (black), the fast (red) and slow (blue) diffusivity states of B. The as-implanted (circles) and the final (squares) profiles are also shown, as well as the local temperature (green line) and the l-s interface (bar). [Fisicaro2013]

As regarding germanium, only few basic experiments providing information on the mechanisms influencing dopant activation (or deactivation) by LTA are reported. Precisely, none about acceptors, whereas, among the donors, only phosphorous and antimony where subjected to structural characterizations. In particular, the partial activation as a result of LTA subsequent to high fluence P-implantation (in the range of 2-60×10^{15}P/cm^2) has been investigated in an early work published in 1985.[Contreras1985] From the observation of lattice parameter contraction as increasing active concentration beyond 1×10^{20}P/cm^3 together with the softening of both optical and acoustic phonons, the authors suggested that dopant pairing with vacancies prevent a full activation of the implanted ions. More recently, experiments on Ge doping by Sb-implantation and LTA in the melting regime suggested that a vacancy excess generation in the molten region limits the full activation, by inducing the formation of electrical inactive Sb_m-V_n complexes.[Bruno2012] In fig.1.11 their cross-sectional transmission electron microscopy (X-TEM) image is reported, in order to illustrate the direct evidence supporting the above deactivation model. A vacancy-rich band observed at the maximum melt depth, where an inactive dopant peak is accumulated.

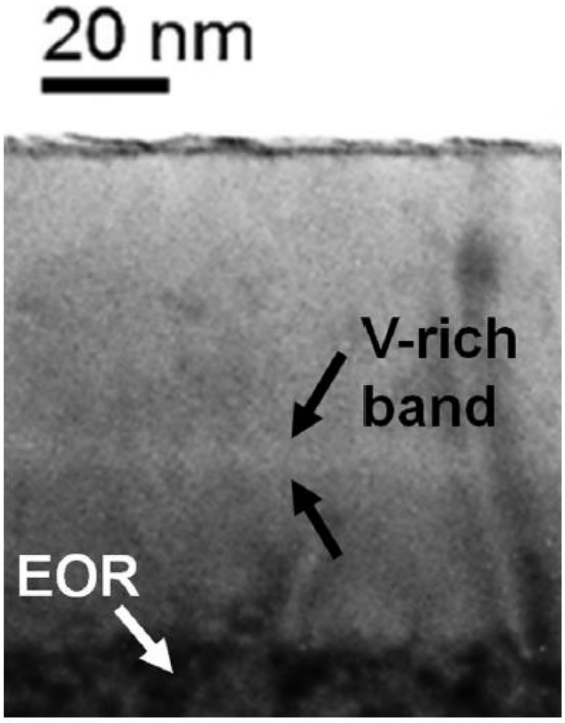

Fig.1.11 X-TEM image of a Sb- doped Ge sample annealed with 5 laser pulses at an energy density of 360mJ/cm^2.[Bruno2012]

CHAPTER 2

EXPERIMENTAL METHODS

In this chapter the sample preparation and the experimental techniques used to characterize both the B and As-doped samples are described. In the first part, the used doping method: a combination of ion-implantation and excimer laser annealing (ELA) is briefly presented. Afterword, the principles and the experimental setup of the used characterization techniques are explained together with the corresponding analysis for providing the final data. Those are Secondary Ion Mass Spectrometry (SIMS), Spreading Resisting Profiling (SRP), Cross-section Transmission Electron Microscope (X-TEM), High Resolution X-Ray Diffraction (HR-XRD) and Atom Probe Tomography (APT). Specific consideration is given to the issues on applying these techniques to the doping of Ge by B or As-implantation and subsequent melting LTA.

2.1 Sample preparation

In this section, the general aspects and the experimental procedure for sample preparation are described, namely the ion-implantation and excimer laser annealing (ELA).

2.1.1 Ion-implantation

Ion implantation is the most used technique to introduce dopants in semiconductors while controlling precisely and independently dopants fluencies or positions. It consists on accelerating energetic ions in an electric field toward the target with enough energy to penetrate beyond the surface. The main advantages are that a mass selection system allows high control on the purity of the implanted elements, and, their implanted concentrations can exceed the solid solubility as well as they can be placed at the required depth and concentration, and with high reproducibility, by tuning the incident energy and the angle, as well as the integrated beam current on the target. However, depending on the kinetic energy transferred collisions, the atoms in the target are typically displaced from their original lattice position and so an extremely large number of point defects are produced. Furthermore, beyond a critical threshold in defects density, the target crystal structure can result even amorphized. Thus, a following annealing step is necessary to recover a good crystalline quality and electrically activate the dopants.

Sample prepared analyzed for this thesis work were prepared by ion implantation on a (100)-oriented Czochralski-Ge wafers with B^+ or As^+ ions at 20keV and 40keV respectively. In particular, two different for each sample are investigated: $1\times10^{15}cm^{-2}$ and 1×10^{16} cm^{-2} for boron while $2\times10^{14}As/cm^2$ and $3\times10^{15}As/cm^2$ for As. In the latter case, ion implantation produced surface amorphous layers of 48nm and 61nm thick for the low and high fluence respectively, as measured by Rutherford Backscattering Spectrometry in channeling conditions (c-RBS). In both of the cases, no special surface preparation or cleaning was done prior to implantation.

2.1.2 Excimer Laser Annealing

Among the laser sources, the ones using excimers as active media irradiate highly intense UV light. The term "excimer" stand for "excited dimer", which is pseudo-molecule formed by the combination of a noble and a reactive gas (fluorine or chlorine) under the appropriate conditions of electrical stimulation and high pressure. Noble gasses are highly inert and do not usually form chemical compounds, so excimers can only exist temporarily in an excited state which can give up its excess energy by undergoing spontaneous or stimulated emission. This decay results firstly in a strongly repulsive ground state molecule, which then very quickly (on the order of ~ps) dissociates back into two unbound atoms. This forms a population inversion between the bound excited and the unbound states which are coupled by photons with wavelengths in the ultraviolet range. For practical purpose, it is worth nothing that an excimer laser systems are suitable for melting LTA of semiconductors because they are characterized by ns-pulses with energy density on the order of ~J/cm^2.

In particular, our implanted samples have been processed in vacuum with Lambda Physik LPX 205, which uses a XeCl laser having wavelength λ=308nm and a nominal pulse with of 28ns (FWHM).The repetition rate uses is ~Hz, i.e. sufficiently slow for subsequent pulses no to superimpose. Our experimental setup was equipped with a beam a beam homogenizer forming 5×5mm^2 spots. The investigated energy densities on samples implanted with As are 530mJ/cm^2 and 650mJ/cm^2, corresponding to different melt depths. For the highest energy, single- and multi-pulses (10 pulses) regimes were tested. Meanwhile B-implanted samples were irradiated at 630mJ/cm^2 for 1, 3 and10 pulses. To complete our study, a portion of unimplanted Ge wafers has been analogously irradiated with 650mJ/cm^2 for 1 and 10 pulses.

2.2 Characterization techniques

Hereafter, the main characterization techniques used for this thesis work are introduced: Secondary Ion Mass Spectrometry (SIMS), Spreading Resisting Profiling (SRP), Transmission Electron Microscope (TEM), High Resolution X-Ray Diffraction (HR-XRD) and Atom Probe Tomography (APT).

2.2.1 Secondary Ion Mass Spectrometry

Secondary Ion Mass Spectrometry (SIMS) is an analytical technique that measures the chemical concentration profile of impurities in the surface region of a solid with sensitivity of in the part per billion (ppb) to part per million (ppm) range for almost all the elements. The technique uses a primary beam of ions (usually O_2^+ of Cs^+) with energy in the range of 0.5-20keV, to sputter the sample surface. As a result of the impact, 1 to 5 atoms per incident ion are sputtered, and about a 2-3% of them are in the form of ions (i.e. secondary ions) and consequently accelerated and analyzed by a mass spectrometer.

One-dimensional concentration profiles as function of the depth can be obtained by counting the selected secondary ions as a function of time. The secondary ion yield as function of time can be converted into a concentration depth profile by a proper calibration procedure. The depth scale is obtained by measuring the final crater depth with a stylus profilometer and assuming a constant sputtering rate. The impurity concentration vs. yield calibration is obtained by quantitative comparison with a standard with a known impurity concentration made of the same matrix as the sample and measured exactly with the same conditions, since the response of the technique depends on the incident ion, the analyzed ion and the sample matrix. The resulting depth resolution is of the order of few nanometers, depending on the uniformity and the low energy of the primary beam.

The analytical conditions should be chosen such as the response of the technique is as much as possible uniform and linear. For this reason, it is worth to collect also a secondary ion composed by element(s) of the matrix, as they are expected to be constant throughout the entire profile for proper analysis conditions.

Furthermore, the SIMS signal in the first few nanometers is typically affected by artifacts due to the native oxide or due to surface transient effects related with the establishment of a steady state between the primary beam ions incorporation and removal. Such effects need to be minimized by optimizing the measurement conditions (typically by reducing the primary beam energy) and/or by removing the native oxide before the measurements. In any case such surface region need to be considered with care and has to be excluded from quantification considerations and from comparison with simulations.

The SIMS measurements reported in this thesis have been measured by a CAMECA IMS-4f spectrometer with a Cs^+ 5.5keV primary beam analyzing $CsAs^+$ and CsB^+ secondary ions, for B- and As-doped sample respectively. Depth profiles of oxygen impurities within those samples are measured by using a primary beam of Cs^+ 7.25keV and analyzing secondary O^- ions. The concentrations of all species have been calibrated using commercial certified standards with an overall accuracy of 10%. The depth scales have been calibrated by measuring the crater depths with a profilometer and assuming constant sputtering rates, with an overall accuracy of 2%.

Indeed, O_2^+ primary beam is usually employed to analyze boron as a secondary positive ion (due to its low ionization potential) and Cs^+ to analyze phosphorous or arsenic (i.e. elements with high electron affinity). Moreover, as regarding laser irradiated samples, particular care on the depth resolution must be taken, especially if dopant behavior in the shallow region close to the maximum melt depth wants to be characterized. For this reason, low energy of the primary beam is preferred to reduce the atomic mixing and therefore O_2^+ should be more advisable than Cs^+ for characterizing the B-doping, also because its depth resolution has been systematically investigated.[Schueler2000, Magee2000] However, by using the oxygen protocol, huge distortion were observed in the reference signal of Ge implanted with high fluence (~1×10^{16}B/cm^2) already before the laser annealing and also increasing with number of pulses. In addition, comparison of the measured implanted B areal densities with the nominal ones evidenced a strong superlinear increase of the B secondary yield by increasing the B concentration. This has been partially related with matrix effects due to the relatively high B peak concentrations (around 2%). For this reason primary Cs^+ ions and CsB+ secondary ions have been selected, as such kind of ions are known to be usually poorly affected by matrix effects[Gao1988], obtaining excellent results with constant matrix yield profiles and implanted doses in good agreement with the nominal ones.

Finally, before the measurements of oxygen profiles, the samples have been etched by hydrofluoridric acid (HF) for 1 minute. Thus the systematic error on the concentration has been minimized, by reducing the oxygen from the superficial native oxide formed as consequence of the air exposure.

2.2.2 Spreading Resistance Profiling

Spreading resistance profiling (SRP) is a technique used to analyze carrier depth profiles. The used experimental apparatus is reported in fig.2.1 and it consists of two carefully aligned tips. Resistance is measured along a beveled doped sample, with typical angle in the range from 0.001 to 0.2 radians. Then, resistivity profile can be obtained converting the measurements thanks to algorithms calibrated with measurements on known-resistivity standards. Finally, carrier concentration versus depth can be inferred by using calibration curve reported in literature which are usually measured by Hall effect, assuming that Hall and drift mobility are equal. The possibility that they are different would represent a systematic source of error in measurements on high doped sample. However, theoretical calculations suggest that no deviation larger than 20% is expected at room temperature. Another systematic error comes from the spilling effect, namely the redistribution of mobile carriers in sample consisting of thin sublayers with sharply differing doping levels.[ClarysseAPL1990]

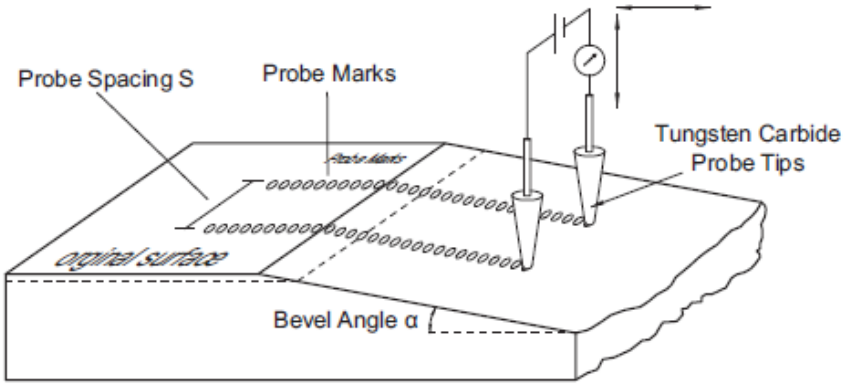

Fig.2.1 Schematic of SRP setup used to probe our sample.[Treberspurg2012]

The carrier concentration profiles reported in this work have been obtained by using a SSM 150 system with probe loading weight of 5g [Privitera1993, Clarysse2006]. The conversion of resistance data into resistivity have been done by means of homogeneously doped (*n*-type) Ge samples of known resistivity. Afterward, the resistivity profiles have been converted into carrier concentration profiles using resistivity versus impurity concentration curve reported in literature,[Sze68] with maximum overall concentration uncertainty of 20%. Last but not least, the measured samples have been expressly doped with the same sign of the substrate, not to form a pn-junctions, so as to prevent the spilling effect.

2.2.3 Cross-section Transmission Electron Microscopy

Transmission electron microscopy (TEM) is an experimental technique which probes with a beam of energetic electrons a thin samples (with thickness on the order of 100nm) prepared by mechanical grinding and or ion milling. In this way transmitted electrons can pass through the sample and an image with nanometric or sub-nanometric spatial resolution can be formed. The advantage of this microscope, with respect to an optical one, is that electrons have de Broglie wavelength smaller than nanometers, so enabling better resolving power of single atom at ultimate sensitivity (~Å).

The TEM can be used to detect residual defects after the implantation and the subsequent annealing, by providing information on their density, type and structure. However, if small clusters are present and with a relatively low density, it is very unlikely to detect them. In general, the minimum cluster size that can be detected in Si and Ge is usually assumed to be about 2nm in diameter.

The X-TEM analyses for this thesis work were performed on selected samples in order to characterize extended defects or dopant precipitates. They have been acquired with a 200keV JEOL JEM 2010 instrument to investigate the residual crystalline damage after the laser annealing. The sample was thinned by mechanical grinding and by ion milling that was performed in a GATAN-PIPS apparatus, at low energy (3keV Ar^+) and low incidence (7°), in order to minimize the irradiation damage.

2.2.4 High Resolution X-Ray Diffraction

High Resolution X-Ray Diffraction (HRXRD) is a non-destructive technique used to precisely determine the deformation state of a single crystal, namely to separate two types of components of the deformation tensor: lattice rotations and tensile/compressive strain. It consists in probing a crystal sample with an X-ray with wavelengths λ that are on the same order of the lattice parameter (~Å). The radiation is then elastically scattered by the electron cloud surrounding the atoms.

The constructive interference between two scattered rays can be described by the Bragg's law:

$$2d\sin(\theta) = n\lambda \qquad (2.1)$$

where n is an integer number related to the order of reflection, θ the angle of incidence and d is the spacing within a sheaf of planes producing a diffraction spot.

Furthermore, the ensemble of the diffraction spots form a lattice associated with the reciprocal of the crystal planes, so that X-ray diffraction is often illustrated with the help of the reciprocal lattice. For practical purposes, it is convenient to define the scattering vector $\boldsymbol{S}$, being the difference between the diffracted k_h and the incident beam k_0. In fact, it can be demonstrated that when $\boldsymbol{S}$ equals a reciprocal lattice vector (Laue condition), the relation (2) is satisfied, so that to a set of reciprocal miller indices (hkl) univocally correspond a specific $\boldsymbol{S}$. Moreover, given the probing λ, the scattering vector directly identifies the experimental geometry through its dependence upon the angle between the incident and diffracted beams 2θ as well as of the angle of incidence with the sample surface ω. Conversely, the length of $\boldsymbol{S}$ can be changed by altering 2θ, or its orientation is scanned by ω.

In other words, the scattering vector at Laue condition defines the family of planes which are diffracting together with their orientation respect to the surface. In general, if ω is equal to θ, the reflection is called symmetrical, otherwise it is called asymmetrical (fig.2.2 and fig.2.3 respectively).

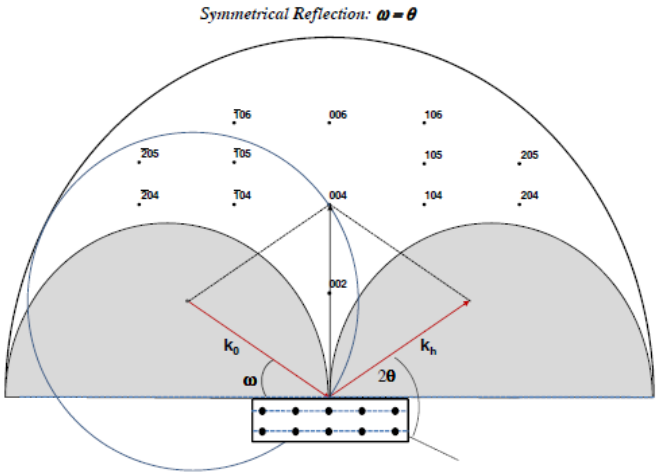

Fig.2.2 Symmetric reflection (ω=θ) for a (001)-oriented Ge crystal. In this case the diffraction involves plains parallel to the surface. The grey areas show regions where either the incoming or the outgoing beam (red arrows) are shaded by the sample.

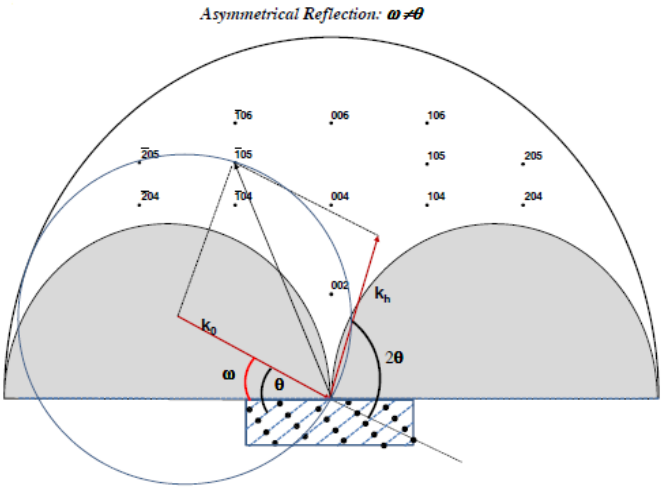

Fig.2.3 Asymmetric reflection (ω≠θ) for a (001)-oriented Ge crystal. In this case the diffraction involves plains not parallel to the surface. The grey areas show regions where either the incoming or the outgoing beam (red arrows) are shaded by the sample.

For the aim of this thesis work the case of an epitaxial layer grown over a substrate of lattice parameter (a_S) is of specific interests. In particular, if there is a mismatch in their lattice parameters, the layer atoms tend to adjust themselves in order to reproduce the same crystalline structure of the substrate. Limiting the description to tetragonal distortion, the cubic layer possesses a parallel ($a_{||}$) while a perpendicular lattice parameter components at the interface ($a_\perp$), which is the only one achieved by a symmetrical measurement. In case of no bending, the strain tensor has only two components, i.e. the parallel ($\varepsilon_{//}$) and the perpendicular one ($\varepsilon_\perp$), defined as following:

$$\varepsilon_{//} = \frac{a_{//} - a_{rel}}{a_{rel}} \qquad (2.2)$$

$$\varepsilon_{\perp} = \frac{a_{\perp} - a_{rel}}{a_{rel}} \qquad (2.3)$$

where a_{rel} is the the lattice parameter of the fully relaxed layer. Moreover, if the layer is pseudomorphic to the substrate, i.e. if $a_{//}=a_s$, so that only $a_\perp$ is distorted according to the Poisson ration:

$$\nu = \frac{\varepsilon_{\perp}}{\varepsilon_{\perp} - 2\varepsilon_{//}} = \frac{C_{11}}{C_{11} - C_{12}} \qquad (2.4)$$

where C_{11} and C_{12} are the elastic constants.[ioffe.ru] In this case, the $\varepsilon_{\perp}$ can be rewritten by using the elasticity theory:

$$\varepsilon_{\perp} = -2\frac{C_{12}}{C_{11}}\frac{a_s - a_{rel}}{a_{rel}} \qquad (2.5)$$

so that a single HRXRD symmetrical measurements is sufficient to obtained a_{rel} by looking at $\Delta\theta$, i.e. the distance between the layer and the substrate Bragg peak θ_B, according to:

$$a_{rel} = a_s\left(1 - \frac{\Delta\theta}{\tan\theta_B}\cdot\frac{1-\nu}{1+\nu}\right) \quad (2.6)$$

In particular, it easy to demonstrate that when $a_{\perp}<a_s$, (i.e. $\varepsilon_{\perp}>0$), $\Delta\theta>0$. In this case, the layer is affected by compressive strain; whereas the strain is called tensile when the opposite case holds.

However, to precisely determine little lattice relative variation which results on the order of 10^{-5} in the detecting relative inter-planar variation $\frac{\Delta d}{d}$, HRXRD measurements are required. Thus, an experimental setup enabling monochromatic and low divergent incoming beam is necessary as expressed by the differential Bragg equation:

$$\frac{\Delta d}{d} = \frac{\Delta\lambda}{\lambda} + \frac{\delta}{\tan\theta} \quad (2.7)$$

where $\Delta\lambda/\lambda$ and δ are the wavelength spread as well as the divergence, respectively.

Those features are usually obtained by equipping X-ray diffractometers with a parabolic bent graded multilayer mirror and a Bartels monochromator, which reduce the δ and $\Delta\lambda/\lambda$, down to 0.003° and to 10^{-5} respectively. If no other element than a detector is added, the resulting configuration is called double axis or open detector and its angular acceptance is of ~1°. Instead, if also an analyzer crystal is added before the detector, the resolution in 2θ is improved and a better signal/noise ratio is obtained, although the probing intensity is reduced and the alignment becomes more difficult. This configuration is called triple axis and its scheme is reported below (fig.2.4).

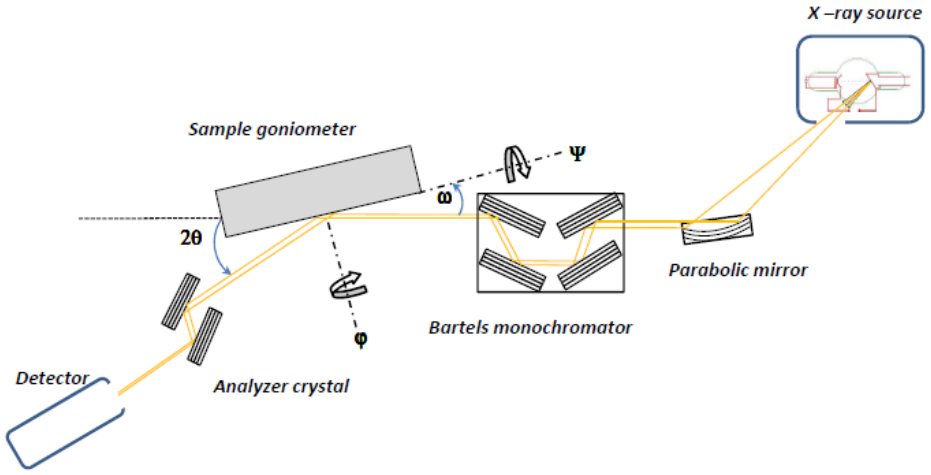

Fig.2.4 Scheme of an HRXRD experimental apparatus. ω, 2θ, φ, Ψare the sample goniometer degree of freedom.

The typical HRXRD measurement is the so called rocking curve (RC) or, alternatively, ω-2θ scan for which ω is varied around a starting value of ω_0 and 2θ has a double variation around a starting point $2\theta_0$. This scan changes the modulus of scattering vector without changing its orientation in the reciprocal lattice. In particular, ω-2θ scan of symmetric reflections runs along the diffraction rod and gives information about the deformation state of the crystal lattice plane parallel to the surface. In principle high resolution measurements are obtained in triple axis configuration since open detector ω-2θ scan can mix the effect of the distribution of inter-planar distances of the sample with the eventual effect of tilt of the planes due to defects or bending. In order to have high accuracy ω-2θ measurements exclusively sensitive to lattice deformation, the scans are deduced by reciprocal lattice map (RLM) i.e. ω-2θ are performed at different starting ω_0 and the integral intensity at every 2θ is considered. In this way eventual distortion of the intensity due to tilt or positioning inaccuracy are corrected.

However, this procedure is highly time consuming because normally at least 20 RCs per RLM are necessary. Therefore, sometimes in this thesis work RLMs have been obtained thanks to a software which interpolates five ω-2θ scans at different starting ω_0 around the substrate peak with a parabola. It was tested that the two procedures give results in good agreement with each other.

Commonly, a quantitative interpretation of a measured HRXRD spectrum obtained is performed by comparing experimental data with simulation according to dynamical theory of diffraction, which correctly considers the wave field propagation in the crystal periodic refractive index as well as all multiple scattering effects.[Wormington1999] Practically, a starting strain profile is used to generate a simulation (fig.2.5) and varied by a chi-square minimization procedure of comparison with the experimental data. Thus, the strain profile as a function of depth can be obtained, with a theoretical minimum uncertainty given by the (2) and typically on the order of ~10^{-5}.

In particular, in this thesis work, the uncertainty on the calculated strain has been always verified by checking if this variation resulted into reliable simulation. As an example, the experimental HRXRD spectrum of Ge implanted with 3×10^{15}As/cm^2 at 40keV and subsequent ELA at 650mJ/cm^2 for 10pulses is reported in fig.2.6, together with the best fit and a simulation obtained assuming a strain value 2 times of the estimated error of 10^{-5} (2σ). Only in the case of arsenic implanted with low fluence (2×10^{14}As/cm^2) the strain resulted close to the sensitivity limit of 10^{-5},so a larger error (2×10^{-5}) corresponding to a significant divergence has been assumed.

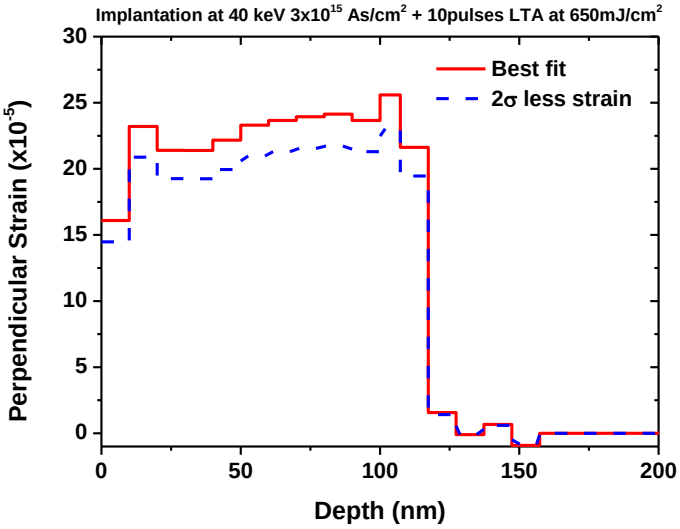

Fig.2.5 Strain profile used to generate the simulation on the right. In particular, the best fit (solid line) is reported together with a strain profile assuming a 2σ of lower strain (dashed line).

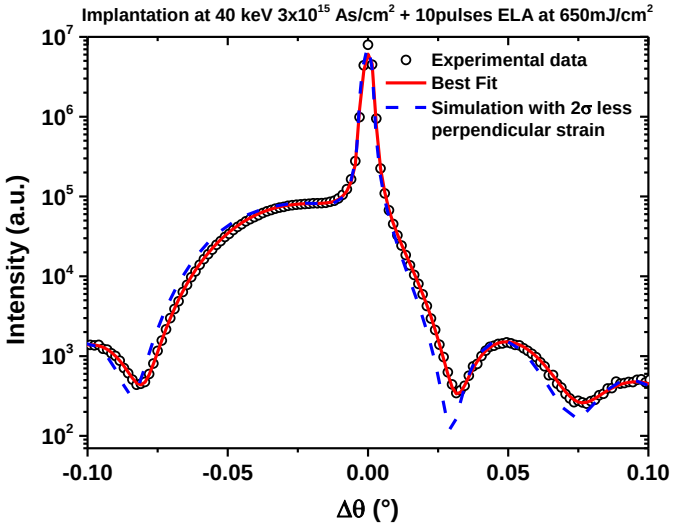

Fig.2.6 Experimental HRXRD spectrum of Ge implanted with 3×10^{15}As/cm^2 at 40keV and subsequent ELA at 650mJ/cm^2 for 10pulses (symbol). The best fit obtained with dynamical theory (continuous line) and a simulation assuming a 2σ of lower strain (dashed line) are also reported.

In the picture above the layer peak is less than 0.05° to the left of the intense substrate peak and intense primary peak), and it appears as an undistinguished bump. The picture demonstrate that simulation can perfectly get such feature only by tuning the strain profile with strain variation as low as 10^{-5}. Also other features, i.e. secondary interference fringes between the substrate and the layer are observed, and their intensity and position (related to the film thickness) are well described in the framework of dynamical scattering theory.

The measurement of peak-to-peak distances and of interference fringes can give all these information in presence of a single layer with a homogeneous composition as a function of depth, but in many cases this this is not true. Thus the rocking curves induced by a strain that changes as a function of the depth can be interpreted correctly imaging a superimposition of thinner layers with different lattice parameters and thicknesses. This is the approach implemented in the dynamical simulation software BEDE-RADS MERCURY[Wormington1999], used in this thesis: the free parameters, i.e. the lattice parameter and thickness of each inserted layer are adapted during a "trial and error" procedure until the residuals, i.e. the difference between the experimental and the simulated data, are minimized.

In the fitting practice, layers of the order of 10-20nm allows to give the best results in case of broad profiles, while in case of abrupt interfaces, 1-2nm depth accuracy is needed to reproduce the fringes position. So, in case of laser annealing this method provide a very sharp estimation on the maximum melt depth. Nevertheless, depth resolution is variable with the sample characteristic, although it can be considered typically less than 20 nm. On the other hand the maximum probing depth is typically of 1-2μm and is mainly limited by the angular resolution.

The relevance of strain profile in our investigation will be pointed out in the results sections. In general the strain status of the first microns of a crystal that undergoes modification processes is due to the average effect of defect and impurities introduced by the process. A classic and well assessed example is the epitaxial growth of semiconductor alloys in which the amount of mixing elements in the alloys regulate the strain. In case of laser annealing doping, the lattice deformation will be induced by the foreign atoms incorporation and by eventual defects accumulation during the processes. The comparison of average strain with chemical and electrical depth profiling will be very useful to disentangle the effect of the different species.

Last but not least, if equipped with an hot stage apparatus, *in situ* measurement as function of temperature can be performed, in order to characterize the strain evolution during defects complexes formation/dissolution. In particular, every changes in the perpendicular lattice parameter variation rate corresponds to the activation of a process, as it can be the dissolution of different types of defects/clusters of defects, or defects complexes reorganization (e.g. cluster growing). Indeed defects complexes formation/dissolution can take place only after overcoming an energy barrier, which is supplied by the annealing.

These class of experiments has to be adapted to the different sample characteristics under study: for example, a not uniform distribution of defects inside the sample could not allow to determine a unique value of the perpendicular lattice parameter for the entire strained layer. In this case it is preferable to consider the strain integral, defined as the area under the strain profile. The strain integral can be used instead of the perpendicular lattice parameter: if the perpendicular strain profile changes its shape during the annealing, its integral undergoes to a general variation, with a rate that depends on the dissolution of different complexes.

The strain profiles presented hereafter have been obtained by performing HRXRD measurements with a Philips MRD X-Pert PRO^{TM} system, equipped with a parabolic mirror and a Bartels Ge (220) four-crystal monochromator. In particular, the Cu $K\alpha_1$ radiation (~8 keV) was selected as the probe. The angular acceptance has been reduced down to 12 arc sec by a channel-cut (220) analyzer equipped detector. The parallel and perpendicular lattice parameters of doped layers can be determined by HRXRD measurements around symmetrical and asymmetrical reciprocal lattice points (004) and (444), respectively. Therefore, RCs can be extracted and they can be simulated by using a the RADS code[Wormington1999], which takes into account the XRD dynamical theory.

Finally, As-doped samples were subject *in situ* measurements by using an Anton Paar DHS 900 hot stage in N_2 atmosphere. The annealing apparatus is made of a heating plate, which is mounted in place of the normal sample holder plate, where the sample is fixed by clips. Then the sample is covered by a plastic dome, with the peculiarity to be almost transparent to X-ray (the beam intensity is reduced by a factor of ~30%). Each step consisted of 100°C/min linear ramp starting from RT up to a 50°C higher temperature kept for 10 minutes and subsequent complete cooling phase. In this way, temperatures of 50, 100, 150, …, 550°C are characterized. The temperature is controlled by a NiCr-Ni thermocouple.

2.2.5 Atom Probe Tomography

Atom probe tomography (APT) is an analysis technique that delivers three-dimensional (3D) chemical characterization with sub-nanometers spatial resolution of materials. Especially, it is ideal to investigate interfaces, segregation and precipitation phenomena and to resolve nanoscale structures including clustering.

It consists in inducing evaporation from a needle shaped specimen with an end radius of about 50nm in order to induce evaporation field magnification. In particular, an atom by atom evaporation on semiconductors is guaranteed by applying an electric field of tens of volts per nanometers on the tip surface coupled with an ultrafast pulsed laser (with repetition rates on the order of 100kHz). The samples is placed in Ultra High Vacuum (UHV) conditions (10^{-11}Torr) and at cryogenic temperature (20-100K). The evaporated ions are analyzed thanks to a position sensitive detector (PSD) system that allows the 3D information on a nearly atomic scale. This is composed by a multi-channel timing system to measure the time of arrival of each ion and by two micro-channel plates in a chevron configuration. Commonly, ion detection efficiency is on the order of 35-50%, namely one ions on two is not detected. Finally, a time of flight (TOF) spectrometer measures the mass to charge ratio. A scheme of the experimental setup is reported in fig.2.7.

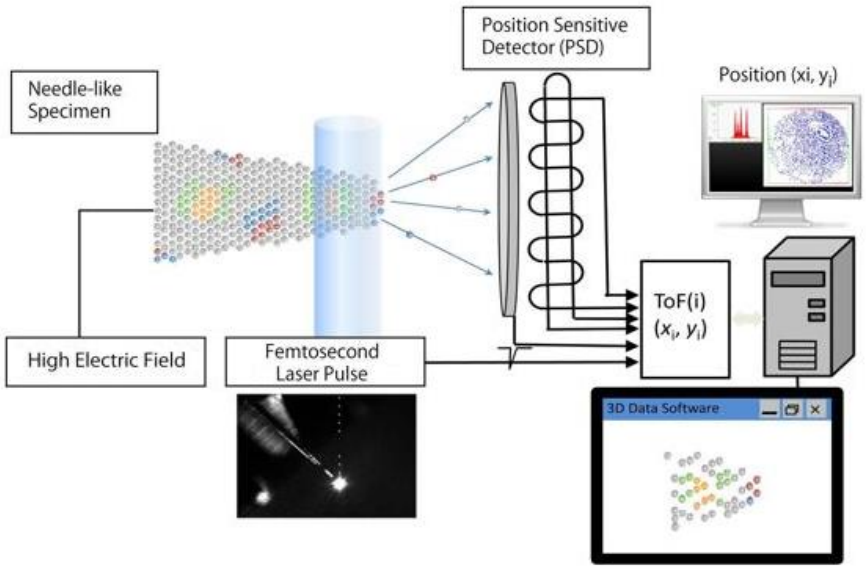

Fig.2.7 Scheme of a laser assisted APT

In order to detect the presence of clustering in the reconstructed volume algorithms methods based on density variation of a certain chemical species which is supposed to form clusters have been developed. Essentially two different approach can be used: the 3D reconstruction or statistical analysis. The former allows to investigate only large clusters (with more than 100 atoms), which are directly detected by pronounced density changes. An indirect method typically employed for small clusters is based on calculating the nearest neighbor (NN) distribution of solute atoms. It consists in dividing the material into blocks of homogenous density and then comparing the obtained NN distribution of the solute with a random one. In particular, a shift is significant of clustering or of precipitation phenomena.[Moody2008] In this case, it is possible to characterize clustering composition and size by assuming that solute atoms within a cluster, on average, tends to be closer to each other than solute atoms in the matrix. This methodology is called maximum separation[Hyde2011] and works with algorithms[Stephenson2007] involving parameters such as the minimum number of solute atoms that defines a significant cluster N_{min} and the maximum separation distance d_{max} grouping together atoms separated by no more than this distance and consequently the size of the cluster.(fig.2.8)

In particular, the distribution of significant clusters as a function of d_{max} is called the cluster count distribution and it is usually chosen lower with respect to the lattice parameter of the matrix, as well as correspondent to values able to maximized the statistical difference between the experimental and random distribution. Finally, the density and chemical composition of the clusters can be calculated as function of this parameter.[Marquis2010]

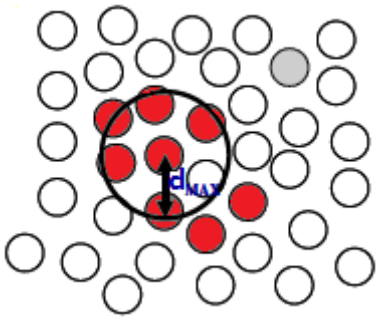

Fig.2.8 Schematic of a cluster of size d_{max}, namely the maximum separation distance between solute atoms (red circles). Atoms of the matrix (white circle) and of an eventual impurity (gray circles) are also reported.

The APT measurements for this this work have been performed after covering the samples with 100nm of a Ni protection layer by physical vapor deposition to ensure the protection of the sample surface in early stages of preparation procedure. In fact, by using a specific method of preparation, needle-shape samples were obtained with focused ion beam as required for APT analysis that were performed by using a LEAP 3000X HR instrument, which provides a detection efficiency of about 37%. The specimen temperature was set at 25K; the evaporation laser pulse rate was kept at 100kHz, initially the energy was set at 0.5nJ to evaporate the Ni surface layer and then it was decreased to 0.07nJ inside the Ge sample. The 3D reconstruction was performed with IVAS software by using a shank-angle based algorithm and an evaporation field of 16V/nm. Finally, the 3D reconstructions were calibrated in depth using the SIMS profiles with an overall spatial resolution higher than the Ge lattice parameter (a_{Ge}=5.6575Å).

CHAPTER 3

RESULTS AND DISCUSSION

This chapter is the core of this thesis work. It consists of the five experiments the were performed during the three years of PhD in chronological order. Therefore, for each experiment it will be described separately the aim of the study, the experimental procedure, the characterization performed and the results will be discussed.

The first experiment that is reported is the study on the diffusion and activation of B during LTA in the melting regime as well as on the mechanisms responsible for the limited electrical activation observed. Similarly to B, a study on arsenic diffusion and activation in Ge as a result of implantation and LTA is reported thereafter, evidencing differences and similarities between the two systems, both in terms of diffusion and activation. Since oxygen contamination is found to favor the deactivation of B through the formation of B-O clusters, a third experiment aiming to characterize the oxygen diffusion into B- and As-doped l-Ge will be presented, in comparison with undoped Ge subjected to the same laser processing. Then, a comprehensive study characterizing the strain evolution in Ge after LTA previous and subsequent to ion-implantation is described. This allows to review the different mechanisms responsible for partial activation in a wide range of experimental conditions. Finally, an experiment characterizing the thermal stability of the two systems is reported.

3.1 Boron diffusion and activation during LTA

The aim of this work is to study the effect of Laser Thermal Annealing (LTA) on B redistribution and electrical activation in Ge. With this purpose, an experimental and theoretical study of the effect of excimer LTA on B redistribution and electrical activation in Ge is reported. Detailed structural, chemical, and electrical characterizations of Ge samples implanted with B (20keV, 1×10^{15}, or 1×10^{16}B/cm^2) and processed by LTA (λ=308nm) with multiple pulses (1, 3, or 10) at 630mJ/cm^2 are performed. Afterwards, the samples have been characterized with X-TEM, SIMS and SRP measurements, following the protocols described in the previous chapter. A diffusion model, in order to simulate the B redistribution induced by the LTA process has been developed, as will be described in the following section.

We will show that an anomalous impurity redistribution occurs in the molten phase, which causes a dopant pile-up at the maximum melt depth. The investigated samples showed a partial electrical activation of the B dopant. The inactivation of B in the samples implanted with 1×10^{15} B/cm^2 is correlated to an oxygen contamination, while the poor electrical activation of B in the samples implanted with 1×10^{16}B/cm^2 is related to the precipitation of the dopant, in good agreement with the experimental and theoretical results.

3.1.1 Modelling

The model developed, in analogy to the case of LTA of B implanted Si substrates, aims to consider the effects on the mass transport of the anomalous bonding state of liquid Ge, which undergoes a semiconductor-to-metal transition on melting.[Chathoth2009] Consistently, we assume that B atoms coexist in two different states: one highly mobile, the other slowly diffusing. The mobile state is virtually bounded to the metallic phase, while the low diffusivity state is trapped by those Ge atoms forming covalent bonds. The temperature rules the corresponding concentrations, as the persistence of covalent bonding depends on T should be more relevant in under-cooled l-Ge. As a consequence, the balance between the two states is modeled by means of (density conserving) rate equations, where the rate parameters are T dependent.

The temperature field, in the presence of the solid-liquid phase transition, has been simulated according to the approach described in Refs.[Huet2009] and [LaMagnaJAP2004]. The diffusion model reads:

$$\frac{\partial C_B^{HD}}{\partial t} = -\nabla\left[D_B^{HD}\nabla C_B^{HD}\right] + k^{\tau}\left(C_B^{LD} - \overline{R}\cdot C_B^{HD}\right) \qquad (3.1)$$

$$\frac{\partial C_B^{LD}}{\partial t} = -\nabla\left[D_B^{LD}\nabla C_B^{LD}\right] - k^{\tau}\left(C_B^{LD} - \overline{R}\cdot C_B^{HD}\right) \qquad (3.2)$$

where D_B^{HD} and D_B^{LD} are the diffusivity of B atoms in the higher and lower diffusion state in liquid phase, respectively, C_B^{HD} and C_B^{LD} are the corresponding concentrations, $k^{\tau}(T)$ is a rate coefficient ruling the transition between the two states, which should be also related to the rapidity of the bonding order fluctuations in l-Ge. $\bar{R}(T)$ is the average (equilibrium) ratio between low and high diffusivity states at constant T. In the solid phase metallic bonds are not present and $D_{Bsol} = D_{Bsol}^{HD} = D_{Bsol}^{LD}$.

The two parameters of the rate expressions in Eqs. (1) and (2), $k^{\tau}(T)$ and $\overline{R}(T)$ have been fixed calibrating the model on the available experimental data. The possible dependence of $k^{\tau}(T)$ on T is not critical as its value was fixed as a constant (not null in the melting phase). The function of T, used for the calibration of $\overline{R}(T)$, tends to constant values in the under-cooled and over-heated regime of the liquid phase, and monotonically switches between these two values for T close to the melting point.

In order to reproduce the experimental fluence loss, the following boundary condition has been implemented at the irradiated surface:

$$\Gamma = \frac{D_B(T,\Phi)C_B}{d_{surf}} \qquad (3.3)$$

where Γ denotes the dopant flux lost towards the irradiated surface and d_{surf} the spatial region where dopant atoms can leave the surface.

3.1.2 Low fluence

Fig.3.1 shows the B concentration profile (dashed line), as measured by SIMS, together with the X-TEM of a Ge sample implanted with B ions, 1×10^{15}B/cm^2 at 20keV, just after the ion-implantation process. Although the ion beam was misoriented by 7° to the normal to the wafer surface, the low energy caused an evident channeling of the dopant.[Rimini1995] The maximum concentration of B resulted to be 7×10^{19}B/cm3. The implanted region appeared, by the micrograph in the same figure, crystalline and free of detectable defects.

X-TEM investigation of the samples subjected to LTA revealed no extended structural defects or precipitates. Fig.3.2 shows the X-TEM view of a low fluence sample annealed with a laser energy density of ~630mJ/cm^2 for 10 pulses. The observed small (few nanometres in diameter) black dots are artefacts, typical of TEM sample preparation of Ge.[Boninelli2012]

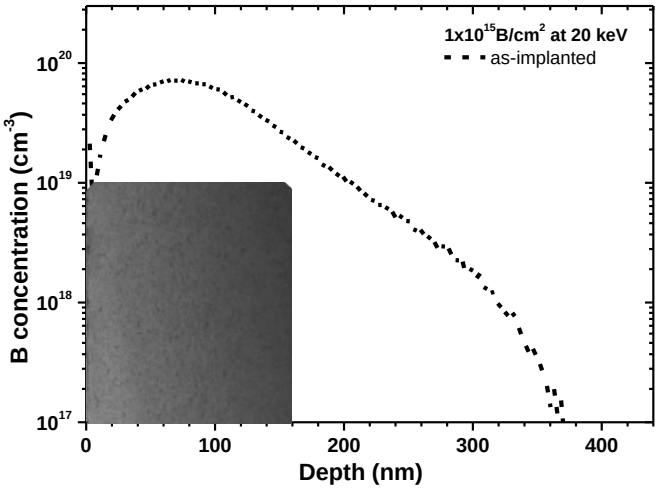

Fig.3.1 X-TEM of a Ge sample implanted with 1×10^{15}B/cm^2 at 20keV, together with the B concentration profile (dashed line) as measured by SIMS, just after the implantation.

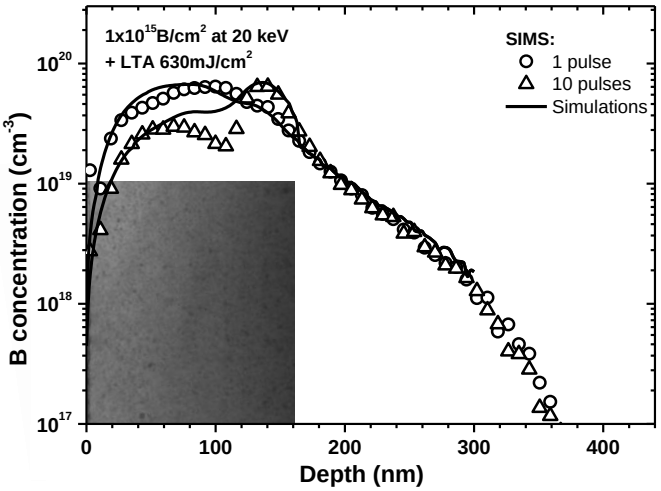

Fig.3.2 X-TEM view of a low fluence sample (1×10^{15}B/cm^2 at 20keV) subjected to LTA (630mJ/cm2, 10 pulses), together with the B concentration profiles after LTA for 1 (circles) or 10 pulses (triangles). Simulated B profiles are also reported (solid lines).

Fig.3.2 also shows the B concentration profiles after LTA for single and 10 pulses irradiation (the 3 pulses one is not shown). Boron is redistributed over a region of ~140nm. A clear pile-up in the B concentration can be observed next to the maximum melt depth (at 138nm), pile-up that increases with the number of pulses (up to ~6.7×10^{19}B/cm^{-3} for 10 pulses). The tail part of the B distributions (at a depth greater than 138nm) follows the slope of the implanted B profile, indicating that in the non-melted areas B atoms do not diffuse. Although a high temperature is achieved at the vicinity of melted zone, the small time duration of the laser pulse prevents thermal diffusion of dopant in these regions. The integration of the SIMS profiles gives a fluence reduction of ~10% for 1 pulse, ~20% for 3 pulses, and ~35% for 10 pulses, when compared to the measured B fluence in the as-implanted sample. This indicates a remarkable B out-diffusion, increasing with the pulse number. It is worth to note that no capping layer was used in our experiment during laser annealing processes.

The experimental results, in particular SIMS profiles before and after LTA processes, suggest an anomalous impurity redistribution in the molten phase, which cause a dopant incorporation during the melt-growth at the maximum melt depth, analogous to the pile-up phenomenon investigated for the case of melting LTA processes in B-implanted Si.[Fisicaro2013]

The designed experiment allows us to analyze the dopant evolution in a wide range of conditions, both varying the thermal budget (multi-pulse processes) and the dopant concentration with respect to the substrate Ge atoms, necessary for getting a reliable calibration of $k^{\tau}(T)$ and $\overline{R}(T)$ to reproduce the non-conventional dopant redistribution. Solid lines of fig.3.2 represent the simulated B dopant profile after single and 10 pulses laser irradiations, for the laser processes performed in samples implanted with a low fluence. The calibration procedure gives the value of $k^{\tau}(T)$=9.0×10^{6}s^{-1} for the reaction rate, whilst the $\overline{R}(T)$ (average ratio between the low diffusivity and high diffusivity B states) is shown in fig.3.3 as a function of T, obtained by means of the calibration work for the low fluence samples. The limit values of $\overline{R}(T)$ in the deep under-cooled and over-heated regimes are 150.0 and 0.3, respectively, and it switches between them in a narrow region ~10K wide close the melting point.

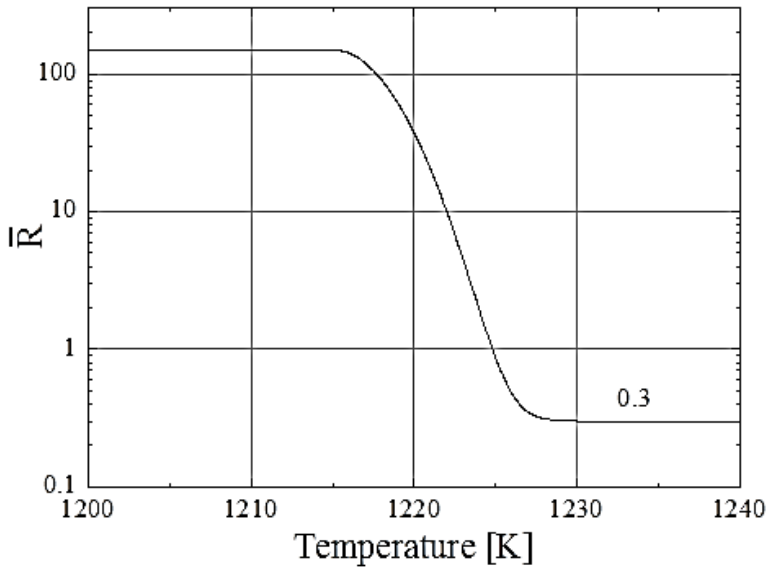

Fig.3.3 $\bar{R}(T)$ function, i.e., the average ratio between low and high diffusivity states at constant temperature, obtained with the calibration process of the low fluence case.

The l-Ge boron diffusivity in the high diffusivity state was found to be $D_B^{HD} = 8.0\times10^{-5}\text{cm}^2/\text{s}$, whilst a value 50 times lower has been extracted for the low diffusivity one. The calibration procedure gave also a value of d_{surf}=1nm for the dopant loss boundary condition of Eq. (3.3) (the same value is kept for all the simulated processes).

The microscopic diffusion mechanism of B in l-Ge, which explains the accumulation, is based on the local balance of B atoms between the two states with different mobility. In particular, dopant atoms in the lower diffusion state are strongly favored in regions at low temperature (i.e., under-cooled regions), whilst atoms in the higher diffusion state characterize the impurity kinetics in the stable liquid regions.

This diffusion mechanism has different effects on the resulting profile, depending on the initial dopant distribution and the maximum melt depth of the process with respect to the implant dopant projected range. During the melting stage the majority of the dopant atoms (71%) resides in their high diffusivity state as the temperature is significantly above the Ge melting point. After that the maximum melt depth is reached, during the re-growth the dopant atoms are shifted toward the s/l interface, due to the presence of the under-cooled phase which favors the B state with low diffusivity and a large density gradient of the high diffusivity component. As a consequence, a net migration of impurity atoms from left to right is the combined result of the two components evolution.

When the laser energy density is fixed and the sample is processed with multi-pulse irradiation, a dopant accumulation near the maximum melt depth is experimentally observed. The good agreement observed between SIMS and simulation for single and multi-shot conditions confirms the validity of the two-state diffusivity model for the B evolution in l-Ge and the role played by the under-cooled liquid during the ns laser annealing.

Fig.3.4a reports the carrier concentration profiles of samples irradiated for 1 (closed circles) or 10 (closed triangles) pulses (the 3 pulses is not shown). The investigated samples show a partial electrical activation of the B dopant: ~50% for 1 pulse, ~40% for 3 pulses, and ~20% for 10 pulses, when compared with the chemical B fluence obtained by SIMS (fig.3.2). The electrical activation never reaches 100%, and it is worse with increasing the number of pulses, thus the best results were obtained for 1 pulse: maximum concentration of active B~4×10^{19}B/cm^{-3} (closed circles). In order to clarify this point, since the X-TEM analyses showed no precipitates, the presence of contaminants, such as C, H, and O has been checked by SIMS. While the presence of a significant amount of C and H was excluded by the SIMS analyses (not shown), the investigation showed the presence of oxygen, as reported in fig.3.4b. The O concentration profile in a virgin Ge is reported as reference resulting similar to the one measured just after the B implantation (not shown). The oxygen signal in the virgin Ge (extending up to ~80nm in depth) is an artefact of the SIMS technique, related to the presence of a native surface Ge oxide and due to atomic relocation during the analyses. The chemical profiles of O clearly indicate the presence of oxygen induced by the LTA process.

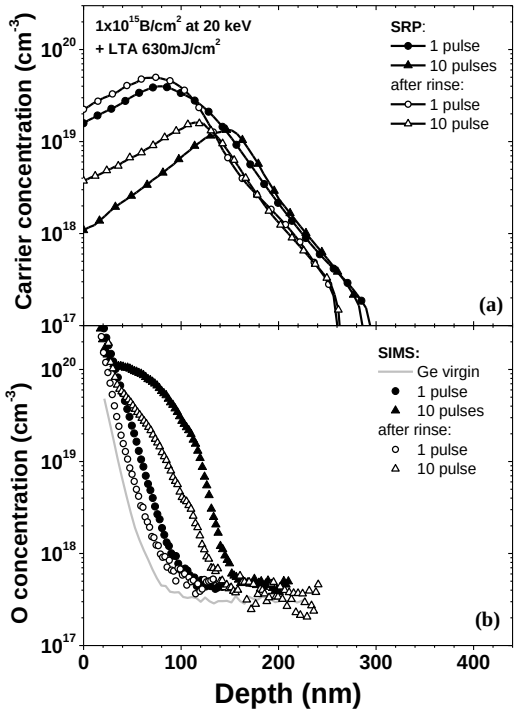

Fig.3.4 Carrier concentration profiles as measured by SRP (a) and O concentration profiles as measured by SIMS (b) after low B fluence implant plus LTA for 1 pulse (closed circles) or 10 pulses (closed triangles), or after low B fluence implant plus etch of native germanium oxide plus LTA for 1 pulse (open circles) or 10 pulses (open triangles). The O concentration profile in a virgin Ge is reported as reference (grey line).

In order to correlate the inactivation of B to the presence of O, the inactive B fluence as a function of the oxygen amount for the three samples irradiated for 1, 3, or 10 pulses (closed squares) is plotted in fig.3.5. The inactive B fluences (the difference between the B fluence measured by SIMS and the carrier fluence measured by SRP) were measured only considering the region where oxygen is present and above the concentration level of $6\times10^{17}cm^{-3}$. The experimental data are well fitted by a straight line with a slope of 0.3. We can speculate that B is inactivated by oxygen, probably coming from the native germanium oxide, which usually forms on the sample surface exposed to the atmosphere. The reaction between B and O may take place within the Ge melt. The reaction products are subsequently incorporated into the grown crystal as electrically inactive complexes. This result is in good agreement with the work by Edwards, reporting the interaction between O and B in liquid Ge during Czochralski growth.[Edwards1968] The lack of the observation of these complexes by TEM suggests that their size and/or density is below the visibility limit for this technique.

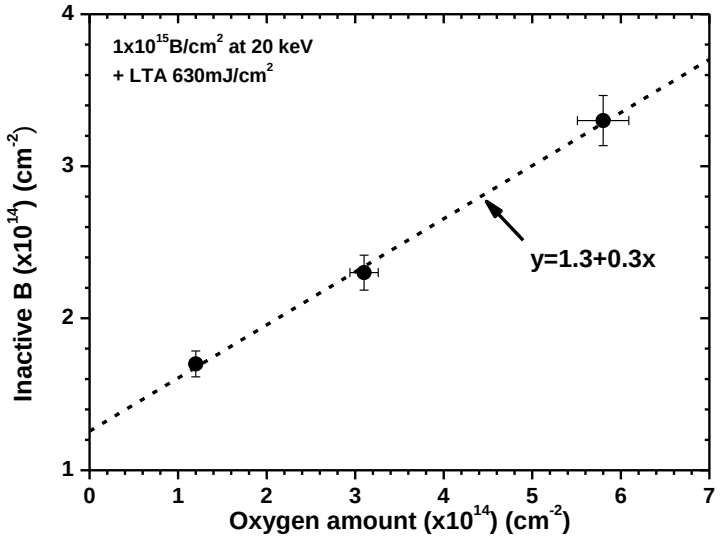

Fig.3.5 Inactive B fluence vs oxygen amount in B-implanted samples plus LTA for 1, 3 or 10 pulses (closed squares). Dashed line is the linear fit of the experimental data.

In order to obtain a higher B electrical activation, the native oxide is removed, just before repeating the LTA processes. In particular, since GeO_2 is partially soluble in water, the as-implanted samples were rinsed in deionized warm (50°C) water for 1min.[Prabhakaran1995] Fig.3.4 reports above the carrier concentration profiles of samples rinsed in warm water and next irradiated for 1 or 10 pulses (the 3 pulses is not shown) and below the correspondent O concentration profiles in the rinsed plus LTA samples. A remarkable reduction of oxygen is evident, which has a clear effect in improving the electrical activation of boron. The maximum concentration of active B is $\sim 5\times10^{19}$B/cm^3 for 1 pulse The persistence of oxygen, even in the rinsed samples, is surely due to the air exposure when the samples are transferred from the warm water to the chamber where LTA is performed. Hence, the effect of oxygen on the electrical activation has to be carefully taken into account when LTA is used as post-implantation processing.

3.1.3 High Fluence

The samples implanted with low fluence (maximum B concentration ~7×10^{19}B/cm^3) allowed to obtain a maximum concentration of active B of ~5×10^{19}B/cm^3, when the samples undergo a rinse in water to remove the native germanium oxide. In order to enhance the electrical activation of the dopant, the B implanted fluence is increased to 1×10^{16}B/cm^2, unchanging all the other process parameters.

Fig.3.6 shows the B concentration profile of a Ge just after the ion-implantation with B ions, 1×10^{16}B/cm^2 at 20keV. The maximum B concentration resulted of ~8×10^{20}B/cm^3. The X-TEM of the same as-implanted sample is also reported. Ion-implantation at this high fluence generated two defective regions into the crystalline matrix: the former is an amorphous region, extending from the surface to a depth of ~20nm; the latter is a defective region close to the projected range of boron ions (~60nm), extending from about 40 to 100nm. This type of damage is typical of diluted collision cascades, as in the case of light incident ions (such as B)[Van den Berg2001]), which usually have smaller activation energy for point-defects recombination. The surface acts as a nucleation seed for the amorphous phase, because the native oxide at the surface enhances the damage stability.[Lopez2007] The observed damage is similar to the damage profile obtained by Rutherford backscattering spectrometry, in Ge samples implanted with B^+ ions at 35keV with fluences higher than 7.6×10^{15}B/cm^2.[Impellizzeri2009]

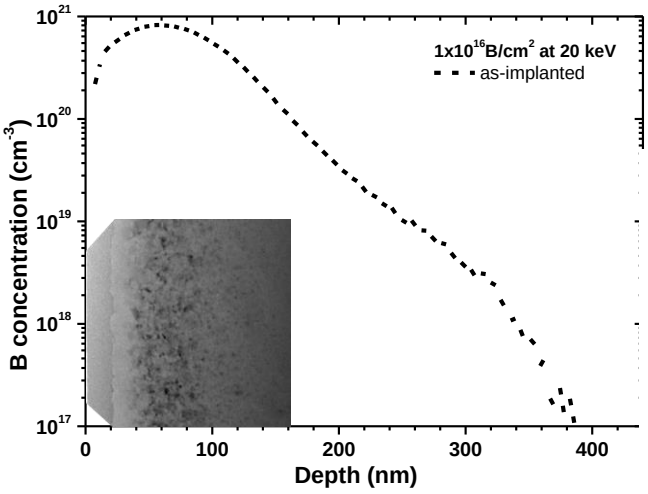

Fig.3.6 X-TEM of a Ge sample implanted with 1×10^{16}B/cm^2 at 20keV, together with the B concentration profile (dashed line) as measured by SIMS, just after the implantation.

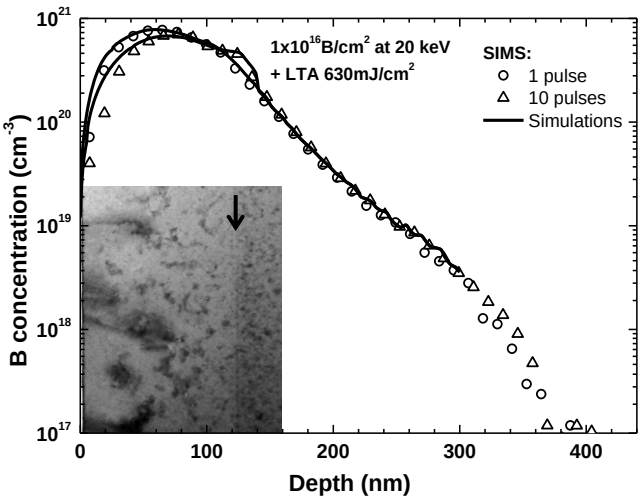

Fig.3.7 X-TEM of high fluence sample (1×10^{16}B/cm^2 at 20keV) after LTA (~630mJ/cm^{2,} 10 pulses) and B concentration profiles after 1 (circles) or 10 pulses (triangles). Simulation are also reported (solid lines). The arrow in the TEM image indicates the maximum melt depth.

X-TEM investigation of the samples subjected to LTA revealed a highly damaged crystal. Fig.3.7 shows a X-TEM view of a high fluence sample annealed with a laser energy density of ~630mJ/cm^2, 10 pulses. The arrow in the TEM image indicates the maximum melt depth, located at ~120nm from the surface. One can observe that the maximum melt depth differs in the low/high fluence samples (roughly 138/120nm, respectively). This difference can be ascribe to a difference in the electronic and optical properties of the Ge semiconductor, caused by the defects and high concentration of boron. The molten zone resulted to be full of isolated damaged regions and dislocations, extending from the B projected range to the surface. Dislocation defects appeared during the very rapid solidification process are likely to result because of the lower melt depth with respect to the extension of the defective doped region.[Tsouroutas2006] Thus, the LTA was not able to remove the implantation damage. As suggested by the isolated defects appearing in the region beyond the maximum melt depth.

Fig.3.7 also shows the B concentration profiles after LTA for single and 10 pulses irradiation (the 3 pulses is not shown). The LTA process does not cause a remarkable redistribution of boron. A clear pile-up of B can be observed next to the maximum melt depth (at ~120nm), increasing with the number of pulses (up to ~4.8×10^{20}B/cm^3 for 10 pulses). The tail part of the B distributions (at a depth greater than 120nm) follows the slope of the implanted B profile, indicating that in the non-melted areas B atoms do not diffuse. Fluence measurement, by integration of the SIMS profiles, gives a fluence reduction of ~10% for 1 and 3 pulses, ~20% for 10 pulses when compared with the measured B fluence of the as-implanted sample, indicating a remarkable B out-diffusion depending on the pulse number, but lower than the out-diffusion observed in the low fluence samples. It is worth to note that also for the high fluence samples no capping layer was used during the laser annealing process.

The calibration of the two states model (Eqs. (1) and (2)) derived in the low fluence case led to some peculiar difference when it is applied to the case at higher fluence. Indeed, simulations performed with the same calibration implemented for the low fluence implants do not fit the experimental SIMS profiles. An overestimation of the dopant loss at the irradiated surface is obtained together with a consequent reduction of the B local concentration (with respect to the experimental one) as a function of the pulse number. We can speculate that this behavior could be related to a concentration dependence of the diffusivity, which is not evidenced in the low fluence case. In particular this missing feature causes an overestimation of the "high-diffusivity" dopant fraction in stable l-Ge, i.e., at temperatures larger than the melting point, leading to a related overestimation of the mean diffusivity in samples where a high dopant concentration is present.

Solid lines of fig.3.7 represent the simulated B dopant redistribution after single and 10 pulses of laser irradiation. In this case, all the model parameters are set equal to that of the low fluence case, with exception of the $\bar{R}(T)$ function.

In the simulation of the low fluence substrate, both the limit values of $\bar{R}(T)$ in the deep under-cooled and overheated regimes (150.0 and 0.3, respectively, see fig.3.3) were held constant for all multi-shots processes. At variance, for the higher fluence case, the limit values of $\bar{R}(T)$ in the deep under-cooled remains 150.0, while it takes the values 3.0, 10.0, and 30.0 for the 1, 3, and 10 multi-shots processes in the overheated regimes. This increase of the $\bar{R}(T)$ value in the over-heated regimes (fig.3.8), which was found through the calibration work and only for the high B fluence substrate, indicates an increase of the low diffusivity component with increasing pulse number and a consequent decrease of the high diffusivity component. Simulation results extracted in this high dopant

implantation fluence specimens have to be taken as indicative of the effects introduced by the high local B concentration (i.e., the large B atomic percent in the Ge-B liquid alloy). Moreover, evidences of these effects can be also perceived in the X-TEM analyses of the samples subjected to LTA. The analyses revealed a highly damaged crystal, with a molten zone full of isolated damaged regions and dislocations. From this point of view, the effective increase of the low diffusivity component with the increase of the pulse number can be an indication of a two correlated phenomena in concomitance of the nanosecond annealing duration: (1) the dopant precipitation processes, where the formed clusters are not fully dissolved in the subsequent irradiations, (2) the free B atoms diffusion in a non-ideal l-Ge whose degradation increases with the pulse numbers. The incomplete dissolution of B precipitates in l-Ge is also supported by the low solubility of B in l-Ge, even for temperatures beyond the melting point of Ge.[Lopez2007] This scenario is consistent with the highly defective matrix evidenced by X-TEM (fig.3.7), and with the effective pulse variation of the low diffusivity component derived by the fitting procedure shown below.

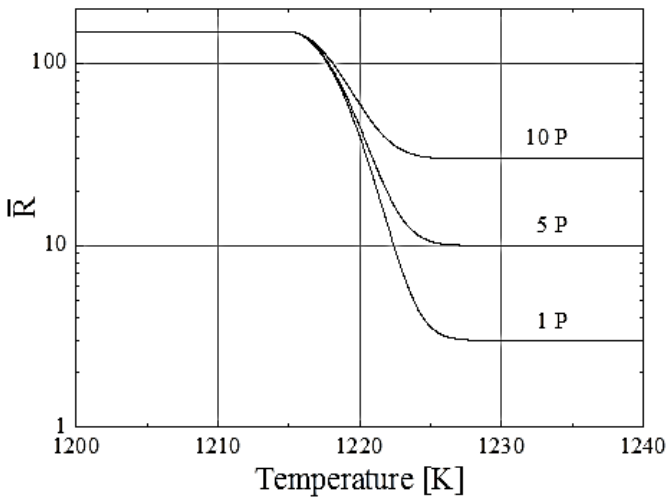

Fig.3.8 $\bar{R}(T)$ function, i.e., the average ratio between low and high diffusivity states at constant temperature, obtained with the calibration process of the high fluence case.

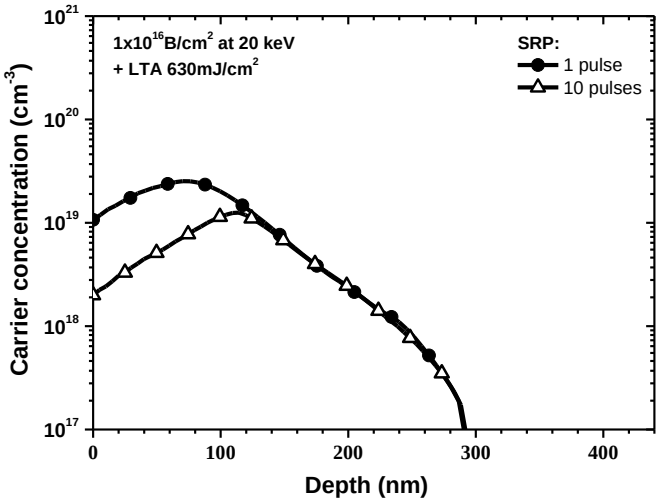

Fig.3.9 Carrier concentration profiles as measured by SRP after high B fluence implant plus LTA for 1 pulse (closed circles) or 10 pulses (opened triangles).

Fig.3.9 reported above shows the carrier concentration profiles as measured by SRP after high B fluence implant plus LTA for 1 pulse (closed circles) or 10 pulses (open triangles). The electrical activation of B is very poor: a few percent of the B fluence obtained by SIMS (fig.3.7). To investigate the role of oxygen, the O concentration profiles are measured by SIMS. The oxygen amount resulted to be similar to the one obtained in the low fluence samples. Since the B concentration is about one order of magnitude higher than the O concentration, we can exclude any correlation between the presence of oxygen contaminant and the electrical inactivation of the B dopant. Indeed, there is no linear correlation between the inactive B fluence and O amount (not shown), unlike the low fluence case.

The very high dopant concentration (~8×10^{20}B/cm^3), together with the small diffusion of the dopant, can suggest the precipitation of B as the responsible for the B inactivation. This idea is in good agreement with the highly defective matrix evidenced by X-TEM, and with simulations, indeed the increase in the $\bar{R}(T)$ value in the overheated regime is typical of dopant agglomeration processes.

3.1.4 Conclusions

In conclusion, a detailed experimental and theoretical study of the effect of LTA on B redistribution and electrical activation in Ge has been performed. In particular, thanks to the two states diffusivity model, the anomalous redistribution of B in Ge melting phase is demonstrated to derive from an unique diffusion mechanism, which is responsible for the observed dopant pile-up phenomenon. The investigated samples showed a partial electrical activation of the B dopant. The inactivation of B in the samples implanted with 1×10^{15}B/cm^2 was correlated to an oxygen contamination, coming from the native germanium oxide that forms on the sample surface exposed to the atmosphere. Hence, this contamination is observed to hamper the substitutionality and the electrical activation of boron, in fact a clear increase of the B electrical activation is obtained after removing the native oxide, just before the LTA processes.

Instead, the poor electrical activation of B in the samples implanted with 1×10^{16}B/cm^2 was related to the precipitation of the dopant, caused by the very high dopant concentration. This idea is supported by the observed small dopant diffusion, the microscopy analyses and the simulation results.

3.2 Arsenic diffusion and activation

The aim of this work is the investigation of the melting LTA applied to the *n*-type doping of Ge by As implantation, which was still unexplored before this this work, despite promising results obtained reported in literature for this process on implanted Phosphorous[Heo2006] and Antimony [Bruno2012]. In particular, the activation record was ~5×10^{19}cm^{-3}, obtained by applying a non-melting laser annealing technique,[HellingsEESL2011] which was lower than the solid solubility limit of 8×10^{19}cm^{-3}[Fistul2004] and is still below the activation levels needed to meet the technological requirements.[HellingsME2011]

For this reason, As^+ ions have been implanted at 40keV with two different fluences (2×10^{14}As/cm^2 and 3×10^{15}As/cm^2) into germanium, so obtaining maximum concentrations of ~7×10^{20}As/cm^3 and ~6×10^{19}As/cm^3 respectively, i.e. below and above the solid solubility. The as-implanted samples have been rinsed in de-ionized water at 50°C for 1min and then excimer laser annealing (λ=308nm) with two different laser energy densities (530mJ/cm^2 or 650mJ/cm^2) and single or multiple pulses was performed. The diffusion and activation of arsenic have been studied, both experimentally and theoretically.

We observed a different behavior with respect to B, with similar diffusion for different fluences, with no out-diffusion and no formation of pile-up at the maximum melt depth. The diffusion profiles have been satisfactorily simulated by assuming two diffusivity states of As in the molten Ge and a non-equilibrium segregation at the maximum melt depth. The electrical activation is partial and decreases with increasing the chemical concentration with a saturation of the active concentration at 1×10^{20} As/cm^3, which represents a new record for the As-doped Ge system.

3.2.1 Modelling

Arsenic redistribution during the melting laser processes is simulated by the same model used to simulate B behavior, with the difference that in this case, as we will see, the non-equilibrium impurity trapping at the liquid/solid (*l/s*) interface has a significant role.[Fisicaro2011] This effect, in the phase field formalism is ruled by the equilibrium segregation coefficient $k_0 = C_S^* / C_L^*$ (for the quasi-static re-crystallization conditions) and by the effective diffusivities in the liquid, solid and interface regions. In general, non-equilibrium kinetic leads to an increase of the impurity trapping in the solid region (i.e. a larger value of the effective segregation coefficient $1 > k_{ne} > k_0$). Of course, the final shape of the simulated impurity profile depends on the parameter calibration and on the process conditions. In particular, the model recovers the pile-up at the melt depth region observed in the case of impurities with large $k_0 > 0.1$ in Si and Ge (like B or P) after the ELA processes. Arsenic in Ge has a relatively low value of k_0=0.02, thus segregation effects are expected even out of equilibrium.

3.2.2 Results

Fig.3.10 shows the chemical As concentration profiles measured by SIMS before (dashed lines) and after (symbols) different LTA treatments on Ge samples implanted with As at 40keV with fluences of 2×10^{14}As/cm^2 and 3×10^{15}As/cm^2 respectively. A significant redistribution of As after the LTA process can be noticed. In particular, after 1 pulse at low energy density, the diffusion is accompanied with a sharp decrease in the As concentration at about 55nm and 68nm for the low and high fluence, respectively. This is a well-known effect in LTA processing, due to the drop of the diffusion coefficient by several orders of magnitude in the solid phase with respect to the liquid phase. Thus, the above values represent an estimate of the maximum melt depths. Such values are deeper than the respective depths of the a/c interfaces measured by c-RBS after ion-implantation, indicating that the LTA, even for the low energy density, has fully melted the amorphous layer. As shown by the SIMS profiles in fig.3.10, in the case of irradiation at high energy density, the maximum melt depth increases significantly up to about 120nm, and it is reached by the diffusing As only after 10 pulses, when the peculiar box-like profile typical of LTA is formed.

It is worth noting that the diffusion profiles have similar shapes for both fluences when analogous LTA conditions are compared, suggesting a concentration-independent diffusion mechanism. This is at variance with what we observed in the case of LTA in Ge implanted with B, where a significant reduction of the B diffusion is present by increasing the implanted fluence as a result of dopant precipitation in the melt phase. Thus, the concentration-independent diffusive behavior of As makes it promising for having reduced As precipitation and consequently for achieving higher activation levels, as will be discussed later.

A small peak at the surface can also be noticed in fig.3.10. Such feature suggests that As is pushed towards the surface by the non-equilibrium segregation at the l/s interface. However, it cannot be excluded that such peak is partially due to a SIMS artifact, being visible, even if to a smaller extent, also in the as implanted sample. Anyway, in the worst case such peak contributes to the total As dose by no more than 10% and, whether or not it is included in the estimation of the total dose from the SIMS profile, no dose loss is detected after LTA within 10%. This indicates that the surface does not act as a sink for the As, on the contrary with what observed in case of B or P.[Tsouroutas2009]

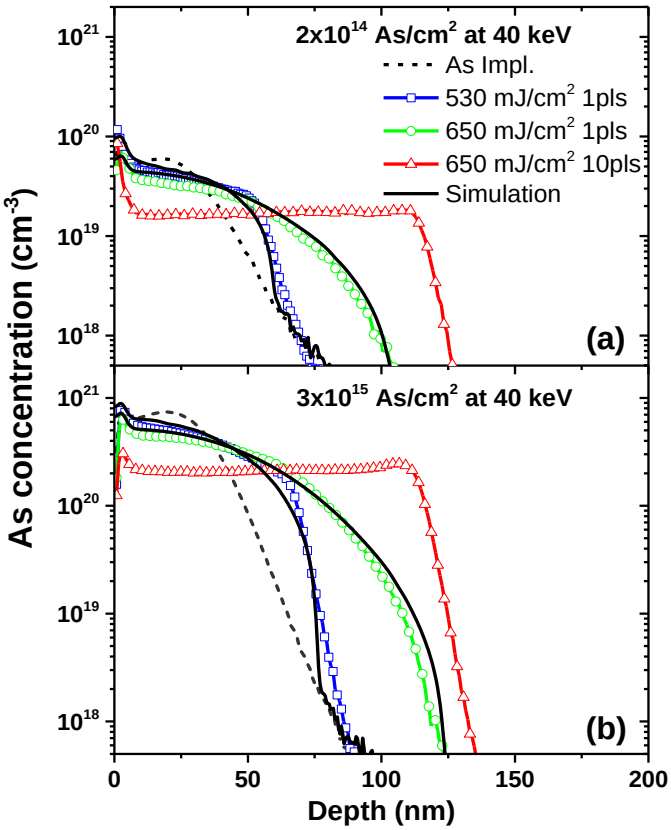

Fig.3.10 Chemical concentration profiles measured by SIMS in samples implanted at 40keV with 2×10^{14}As/cm^2 (a) and 3×10^{15}As/cm^2 (b) before (dashed lines) and after (symbols) LTA processes with 1 pulse at 530mJ/cm^2 (squares), 1 pulse at 650mJ/cm^2 (circles), and 10 pulses at 650mJ/cm^2 (triangles). Simulations obtained with a phase-field model (solid lines) of the profiles after 1 pulse are also reported.

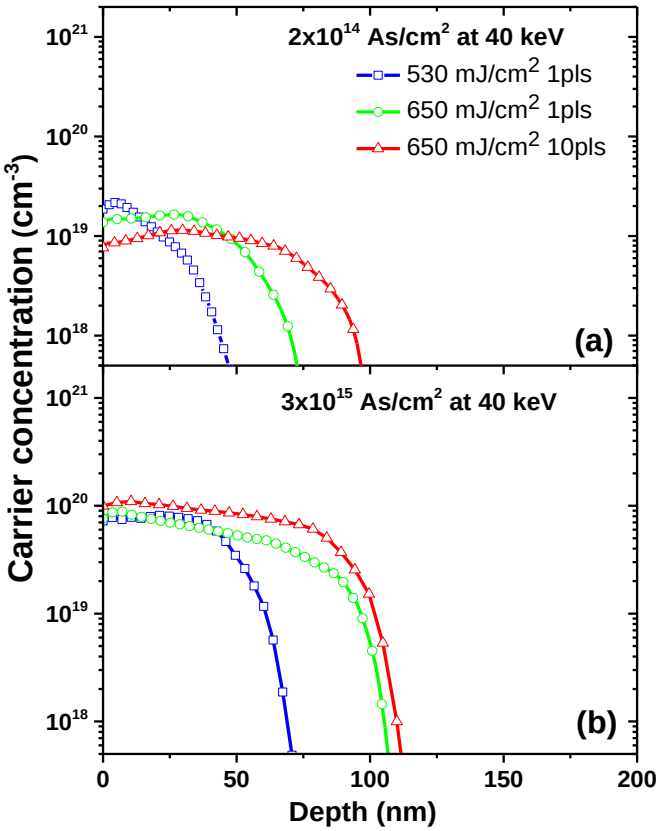

Fig.3.11 Carrier concentration profiles measured by SRP in samples implanted at 40keV with 2×10^{14}As/cm^2 (a) and 3×10^{15}As/cm^2 (b) after LTA processes with 1 pulse at 530mJ/cm^2 (squares), 1 pulse at 650mJ/cm^2 (circles), and 10 pulses at 650mJ/cm^2 (triangles).

Further insights on the above phenomena can be driven by the simulation fits (continuous lines in fig.3.10) of the SIMS profiles obtained after 1 pulse LTA reported in the same figure. As described in above, such simulations, which reproduce satisfactorily the experimental data, have been obtained according to the phase-field methodology, including the thermal problem due to LTA treatment, the phase change of the irradiated material, the covalent/metallic non-Fickian impurity diffusion in l-Ge as well as the non-equilibrium dopant segregation at the l/s interface. The same parameters obtained by

the calibration for B in Ge are used (low fluence case), except for the As diffusivity in the high diffusivity state that was optimized in order to fit the experimental data (the ratio between the diffusivities in the high and low diffusivity states was kept equal to 50 and 0.4 in the undercooled and non-undercooled regime, respectively). The As equilibrium segregation coefficient was assumed k_0=0.02 according to the experimental estimation reported in literature.[Olesinski1985] The simulations reproduce both laser treatments varying the laser energy density. During the melting process and the subsequent crystalline regrowth towards the surface, two distinctive phenomena concurrently occur: the first one is the dopant dynamics in both high and low diffusion states, whose final effect is to push impurity atoms into l-Ge during the ns melting process towards deeper regions during the regrowth, due to the unbalance of both dopant components in the liquid phase; the second one is the dopant segregation at the l/s interface with a net effect of pushing the dopant towards the surface during the melting evolution. In the case of B in Si or Ge substrates, the first effect is predominant with a final dopant accumulation at the maximum melt depth. In the present investigation, i.e., As in Ge, experimental data show no pile-up in deeper molten regions. Concurrently, a peak has been suggested by SIMS near the surface. Both observations suggest that for the case of As, the segregation is the dominant effect in the competitive dynamics during LTA. Simulations, including both effects, confirm this picture reproducing the peak at the surface as well as no-accumulation in deeper regions.

Moreover, the simulations confirm that As diffuses in the Ge molten phase with the fast diffusing component having a diffusion coefficient of ~3.0×10^{-4}cm^2/s with no dependence on concentration, and with no appreciable clustering. This is in agreement with the equilibrium properties of the Ge-As system, where liquid solution all over the As concentrations range can be deduced from the phase diagram above the melting temperature of Ge.[Olesinski1985]

As a result, data suggest that in the As-doped Ge system, the characteristic pile-up resulting from LTA is overwhelmed by the concurrent segregation, which depends on the l/s interface dynamics. In particular, the k_{ne} tends to its low equilibrium value of 0.02 when the moving interface slows down approaching the maximum melt depth. Thus, the As arriving from the molten phase at the l/s interface at the maximal melt depth has a much higher probability of being rejected into the liquid thus canceling any pile-up formation. On the other hand, as soon as the l/s interface moves off the maximum melt depth and approaches the surface, it also accelerates significantly due to the increase in the cooling rate and k_{ne} tends to 1. As a result, the As is incorporated in the crystal and no significant dose loss is observed.

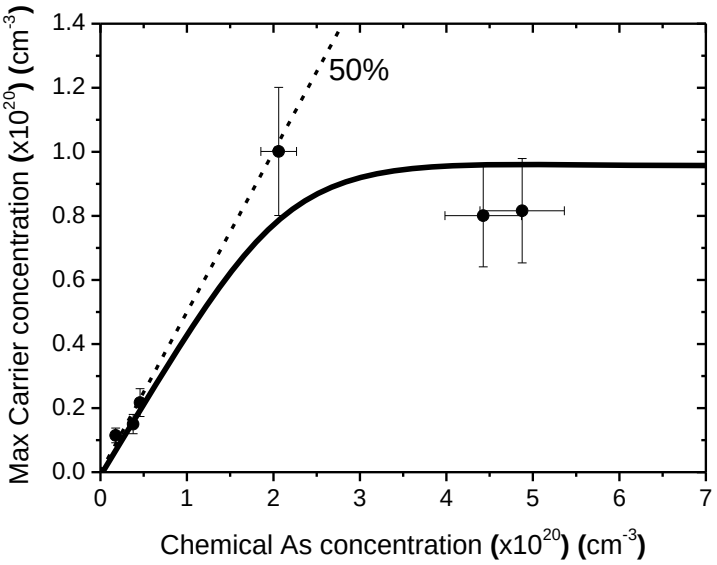

Fig.3.12 SRP carrier concentration versus SIMS chemical concentration extracted at the max carrier concentration depth from the profiles reported in figs.3.10 and 3.11. The dashed line indicates an active fraction of 50% and the continuous line has been drawn to guide the eye.

Fig.3.11 shows the carrier concentration profiles measured by SRP on the same annealed samples of fig.3.10. In the case of the sample implanted with the low fluence of 2×10^{14}As/cm^2 (fig.3.11a), the carrier concentration profiles show a similar qualitative behavior with respect to the chemical profiles (fig.3.10a), with different electrically active concentrations as well as junction depths as a function of the LTA conditions. On the contrary, in the samples implanted with the high fluence of 3×10^{15}As/cm^2, the carrier concentrations (fig.3.11b) does not seem to be correlated with the chemical concentration (fig.3.10b).

In order to clarify the above data, the maximum carrier concentrations for each SRP measurement of fig.3.11 has been extracted and reported in the fig.3.12 as a function of the corresponding chemical concentrations extracted in fig.3.10 at the same depths. It is clear from fig.3.12 that the maximum electrical activation follows a linear trend, being approximately 50% of the chemical concentration (dashed line), up to a value of As concentration of ~2×10^{20} As/cm^3, above which it saturates at an activation level of about ~1×10^{20}As/cm^3. Such high value, obtained with the sample implanted with the high fluence of 3×10^{15}As/cm^2 after 10 pulses at 650mJ/cm^2, is remarkable as it is about a factor of 2 above the previous record obtained with laser annealing in sub-melting regime, and meets the requirements of future technological nodes.[HellingsEESL2011]

The partial electrical activation depicted in fig.3.12 and, in particular, the saturation behavior of the electrically active concentration as a function of the chemical concentration is quite surprising. A possible deactivation mechanism might involve the interaction with O coming from the surface, as observed after similar ELA processes for B in Ge. However, the surface native oxide has been removed before performing the ELA process, and SRP profiles are flat in the surface region thus showing no evidence of changes in the activation mechanism approaching the surface. In addition, as it is shown in the next section (fig.3.18), the O dose extracted by SIMS resulted to be not correlated with the electrically inactive As dose extracted from data reported figs. 3.10 and 3.11. As a matter of fact, the behavior is completely different for B in Ge, where a depletion of activated dopant can be observed close to the surface (fig3.4) and a correlation between O dose and inactive B dose was found (fig3.5), as a direct evidence of B-O interaction. Thus, it can be already concluded that there is no significant role of oxygen contamination from the surface in the observed partial activation of As in Ge after ELA, as confirmed by the further investigations reported in the following experiments.

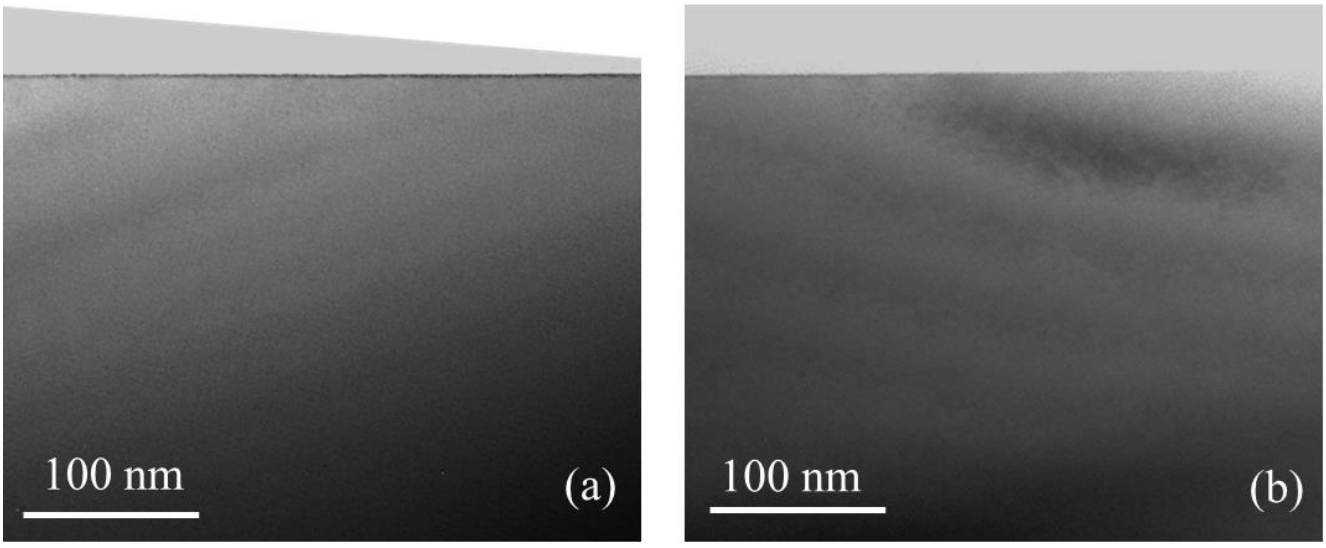

Fig.3.13 X-TEM of Ge implanted at 40keV with 3×10^{15}As/cm^2 after LTA at 650mJ/cm^2 with 1 (a) or 10 pulses (b).

In order to get more insights on the partial electrical activation of As, we characterized by X-TEM the samples implanted at 40keV with 3×10^{15}As/cm^2 after 1 pulse and 10 pulses at 650mJ/cm^2 LTA (fig.3.13), which represent, one of the two samples with the highest inactive fraction (more than ~80%) and the sample with the highest activation, respectively. No evidence of extended defects nor clustering, nor appreciable contrast modulation is reported in both samples. This fact has important implications: first of all, the absence of extended defects is remarkable for the implementation of LTA processing after ion-implantation; second, no considerable accumulation of vacancies at the maximum melt depth (within the sensitivity of the technique) is produced LTA, in agreement with what observed with Band at variance with what observed for Sb. Finally, inactive As is presumably in the form of very small clusters, with diameters falling below the X-TEM sensitivity of about 2nm. Such agglomerates hardly form due to a precipitation in the bulk of l-Ge, which can be ruled out for several reasons. As discussed previously, the Ge-As liquid solution above the Ge melting temperature is indicated to be thermodynamically stable in the Ge-As phase diagram. In addition, the good quality of the simulations reported in fig.3.10 has been obtained by assuming no clustered fraction of As in the liquid phase. Furthermore, also the mechanism of bulk As-O clustering has been ruled out in the previous paragraph. Instead, we can speculate that the origin of the partial As activation in Ge during LTA is related to a mechanisms acting during the regrowth process at the l/s interface, or very close to it. In fact, as the liquid close to the l/s interface is undercooled in this temperature regime, the anomalous covalent bonding state of l-Ge should be more relevant,[Chathoth2009] and this might alter the solubility of As in the liquid Ge phase. However, the multipulses profile clearly display an homogeneous partial activation, so leading us to rule even a interphase speed dependence, as expect in the latest case. So, the only reasonable possibility left is that a fast precipitation towards the equilibrium As solubility occurs in the crystalline phase close to the l/s interface, where the temperature remains, at relatively high values, even if for a very short transient. Exploring this hypothesis, further investigations are presented in the following experiment.

3.2.3 Conclusions

Implanted As in Ge is observed to redistribute significantly within the melt during LTA, with no appreciable dose loss, no pile-up at the maximum melt depth, and no formation of extended defects. The diffusion profiles are satisfactorily simulated with a model based on anomalous l-Ge with two As diffusivity states and non-equilibrium As segregation at the l/s interface. The As in the fast diffusivity state shows a diffusion coefficient of 3.0×10^{-4}cm^2/s independent on As concentration.

The electrical activation increases proportionally by a factor of ~50% along with the chemical concentration, up to a saturation level of $\sim1\times10^{20}$As/cm^3, which is above the solid solubility and a factor of two higher than the previous best activation level for As-doping in Ge. A mechanism related to clustering phenomena occurring just beyond the l/s interface during crystallization is supposed underlying the As partial activation but needs further investigations. The present work confirms ELA as a promising technique and suggests arsenic as a possible candidate in order to overcome issues in forming *n*-type USJs on Ge.

3.3 Role of oxygen contaminants

The role of the oxygen contamination on the electrical activation and its interaction with dopants during LTA is further investigated also in the sample implanted with arsenic. At variance with boron, no correlation with the partial activation is observed, despite a deep oxygen penetration into the molten region is detected. In order to investigate on the origin of the contaminants, an un-implanted Ge sample has been subjected to 1 or 10 pulses of LTA at 650mJ/cm^2. Oxygen infiltration even in this case has been found thus unambiguously induced by the laser processing.

Moreover, by fitting the experimental SIMS profiles of contaminants, lower oxygen diffusivity ($\sim 3\times10^{-5}$cm^2/s) is observed if boron is present, so demonstrating the B-O interaction already in the liquid phase. At variance, no As-O interaction in l-Ge is suggested, as long as oxygen diffusion after As-implantation is unchanged with respect to the unimplanted sample. For the same reason, however, the multipulse regime results into a complete redistribution within the molten region that allows only a lower limit estimation ($\gtrsim 10^{-4}$cm^2/s) for the oxygen diffusivity into As- or (un-)doped l-Ge

3.3.1 Results

The oxygen concentration profiles as measured by SIMS after the high fluence (fig.3.14) and (fig.3.15) low fluence As-implantation and subsequent LTA at for 1 (open symbols) and 10 (closed symbols) are shown above. The oxygen penetration in these samples is clearly observed being proportional to number of pulses. In particular, after 10 pulses a complete redistribution of the oxygen over a region of ~120nm (that is the molten region) is obtained. The contaminant profiles on a virgin Ge sample (not implanted nor irradiated) are also reported (dashed lines), this signals are due to the relocation of the oxygen from superficial native oxide during the SIMS analyses. The as-implanted profiles (solid lines) displayed the same shape. This represents less than ~15% of the contamination fluence detected after laser irradiation, thus suggesting that the largest amount of oxygen is introduced by the LTA.

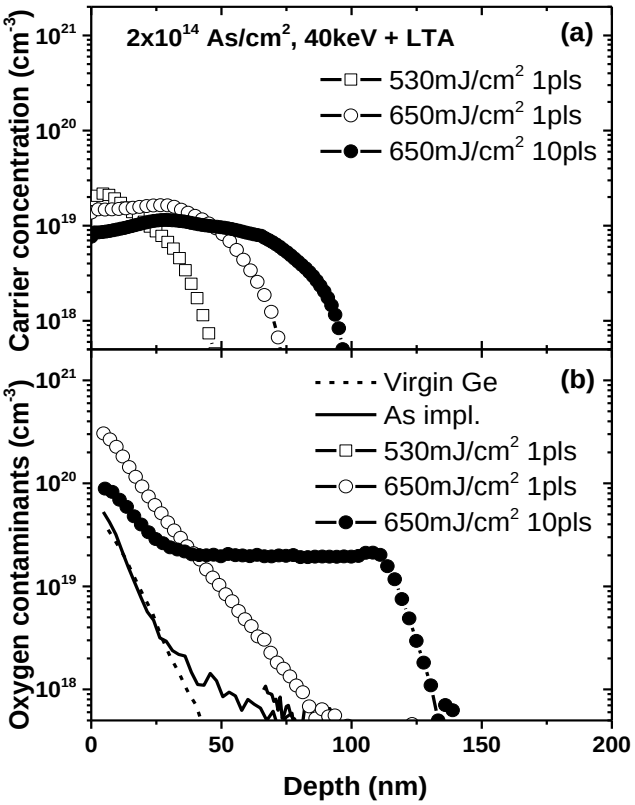

Fig.3.14 Carrier (a) and oxygen (b) concentration profiles as measured by SRP and SIMS respectively after implantation with 2×10^{14}As/cm^2 at 40keV and LTA at 530mJ/cm^2 for 1 pulse (open squares) and 650mJ/cm^2 for 1 (open circles) and 10 (closed circles) pulses. The oxygen profiles measured in the as-implanted (solid line) and in a virgin-Ge sample (dashed line) are reported as reference.

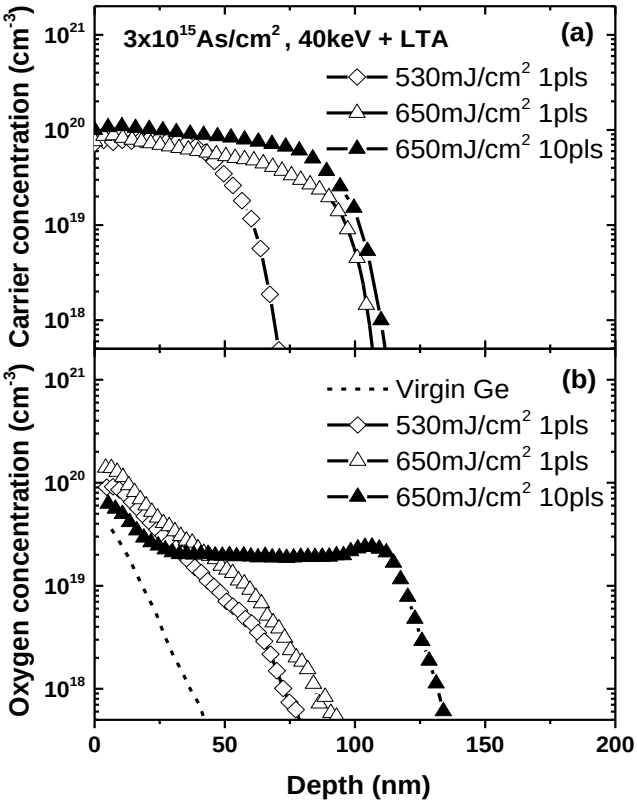

Fig.3.15 Carrier (a) and oxygen (b) concentration profiles as measured by SRP and SIMS respectively after implantation with 3×10^{15}As/cm^2 at 40keV and LTA at 530mJ/cm^2 for 1 pulse (open diamonds) and 650mJ/cm^2 for 1 (open triangles) and 10 (closed triangles) pulses. The oxygen profiles measured in a virgin-Ge sample (dashed line) are also reported as reference.

In the same figure the carrier concentration profiles already shown and descripted in the previous experiment are reported. The uncorrelation with contaminant penetration can be already appreciated by comparing the two implantation fluences, where similar oxygen concentration are observed, but the activation results one order of magnitude higher. Nevertheless, one might argue that the oxygen is a second order effect and some correlation could be found within the same implantation fluence. So oxygen and inactive arsenic concentration extracted at the maximum activation depth as well as the fluence are carefully checked (figs.3.16 and 3.17). In addition, also attempts in excluding and including the SIMS in the first 20nm are tried, but no correlation is found, at variance than in case of boron which showed a clear correlation as previously shown in Fig. 3.5.

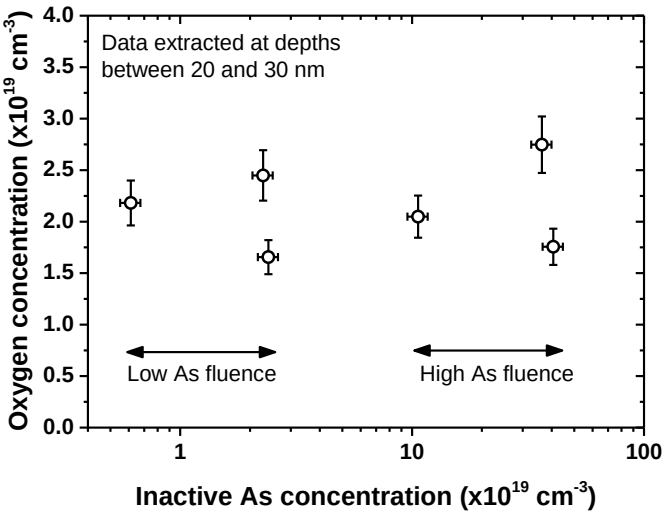

Fig.3.16 Oxygen vs inactive As concentration as measured from SIMS at the maximum carrier concentration depth.

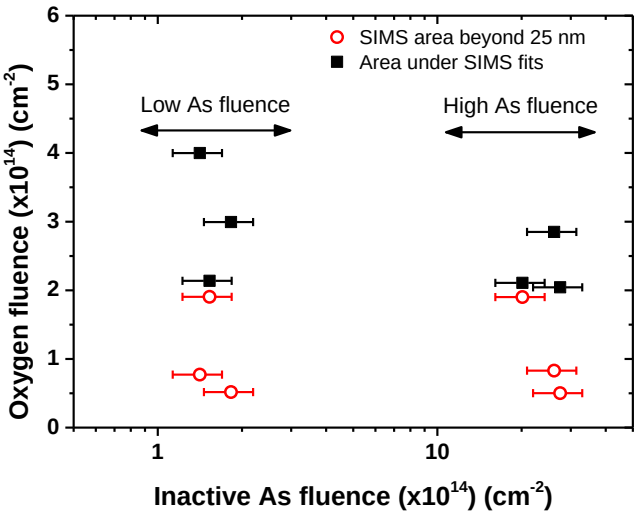

Fig.3.17 Oxygen vs inactive As fluence as measured from SIMS. Both the integration excluding (circles) and including the superficial peak (squares) are tried.

Further insights are given by the oxygen chemical profiles as measured by SIMS after 1 and 10 pulses (open and closed symbols respectively) in three different conditions (un-, As- and B-implanted), as reported in fig.3.18 (squares, triangles and circles). It is interesting to note that the oxygen redistributes within the molten layer already into unimplanted Ge after 1 pulse (open squares), despite the dip with de-ionized water at 50°C for 1min performed to remove the superficial native oxide, so evidencing that the oxide removal during the dip is only partial and/or some oxidation occurred between the dip and the LTA. Before discussing the evolution, it is important to note that the measured oxygen fluence in this reference sample is lower (roughly 4 times) compared with the implanted ones, which show also higher superficial concentrations, thus suggesting that ion-implantation slightly enhances oxygen incorporation. Nevertheless, the oxygen profiles both in un- and As-implanted samples are in qualitative agreement with each other.

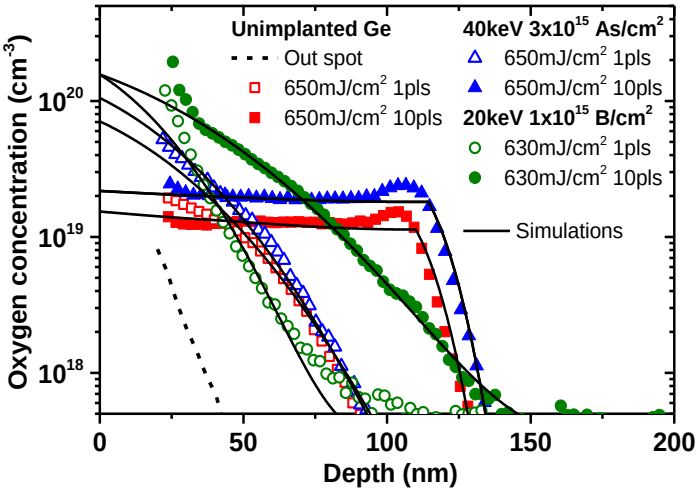

Fig.3.18 SIMS characterization of oxygen penetration into unimplanted Ge (squares) after 1 (open symbols) and 10 pulses (closed symbols) of LTA at 650mJ/cm^2 and implanted with 3×10^{15}As/cm^2 at 40keV (triangles) as well as with 3×10^{15}B/cm^2 20keV and subsequent LTA at 630mJ/cm^2 (circles).

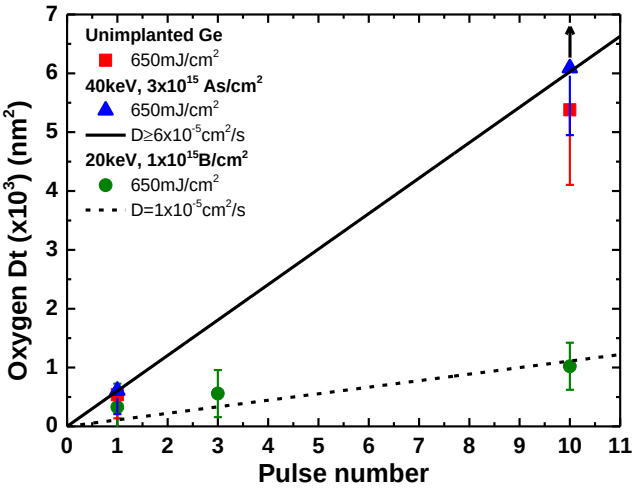

Fig.3.19 Dt versus the pulse number, as determined by the fits of the O concentration profiles. The linear fit for un- and As-implanted (solid line) and for B data (dashed line) are also reported.

From the evolution of contaminant profiles recorded after 10 pulses of LTA, different behavior due to the doping is observed. In particular, oxygen diffusion in presence of B (closed circles) is shallower than in the unimplated Ge, as a result of the B-O interaction occurring in l-Ge which is thus responsible not only for the B partial activation through B-O complexes precipitation descripted above, but also for a reduction of O diffusivity in the melt phase. On the contrary, oxygen diffusion in As-doped sample after 10 pulses at 650mJ/cm^2 (closed triangles) is similar to that observed in unimplanted Ge irradiated with the same conditions, suggesting that no As-O interaction is taking place in the liquid phase. Moreover, contrary to B-O interaction, no studies concerning possible As-O interactions in l-Ge, even in non-equilibrium conditions, are reported as far as our knowledge. Indeed, the disconnection between impurity penetration and As deactivation is confirmed (the sample implanted with 3×10^{15}As/cm^2 at 40keV after 10 pulses at 650mJ/cm^2 shows the highest activation, but also the largest amount of oxygen concentration). In effect, direct interaction forming an As-O pair in solid Ge (as well as in Si) is recently found to be unfavorable by DFT calculation,[Chroneos2012] so even any interaction during fast cooling can be excluded.

Finally, in every case the diffusion can be satisfactory described by numerically solving the Fick's equation in 1D which was done thanks to a code written in ANSI-C and developed by our group. The peculiarity of the code is the implemented boundary condition which are very generally described by means of λ, namely the efficiency of the interface to sustain a fixed oxygen concentrations C_0 at maximum melt depth, according to:

$$D\left.\frac{\partial C}{\partial x}\right|_{x=melt\_depth} + \frac{D}{\lambda}\cdot\left(C_{eq} - C_0\right) = 0 \qquad (3.4)$$

This equation describes the behavior of the melt depth acting as a perfect well at the virtual concentration C_{eq} localized at depth λ. In our case, the limit cases of $\lambda\to\infty$ was used to describe a perfect "mirror" conditions for oxygen reaching the maximum melt depth.

The code returns the oxygen concentration profile of the contaminant within the molten region (reported in fig.3.18) and it provides, in first approximation, *Dt* (i.e. the square of the penetration length) for the different number of pulses, as reported in (fig.3.19). So, the effective diffusivity of O in the three different condition can be estimated, by combining these values with *t*, namely the stay time of O in the liquid phase (i.e. the duration of the liquid phase) estimated thanks to the model described in the previous experiments: ~100ns.

In particular, the diffusivity in l-Ge under LTA after B-implantation results $\sim 1\times10^{-5}$cm^2/s and, since no comparison has been found in literature, the obtained value is the first estimation of this quantity existing, as far as our knowledge. On the other hand, in the case of un- or As-doped sample, only a lower limit of $\gtrsim 6\times10^{-5}$cm^2/s for the oxygen diffusivity can be inferred from the reported profiles. In fact, no exact value into Ge undergoing a melt phase is achievable due to the box-shaped profile observed after multipulse irradiation. However, as being closer to the typical liquid phase diffusivities ($\sim10^{-4}$cm^2/s) and much higher than into B-doped Ge, this value evidences again no slowing down effect by the arsenic.

3.3.2 Conclusions

In conclusion, as a result of this experimental study on the oxygen diffusion in Ge after LTA in the melting regime previous and subsequent to ion-implantation, oxygen contaminants penetration already into the unimplanted sample as a consequence of LTA is demonstrated. However, no correlation with the inactive arsenic is found, so indicating that the contaminates do not significantly affect the doping.

In particular, the experimental O profiles are fitted so allowing to originally determine the diffusion coefficient of oxygen in the doped l-Ge. In particular, oxygen diffuses into As-implanted samples in similar way than into undoped Ge after the same irradiation condition, thus excluding any As-O interaction in the liquid phase.

On the contrary, after B implantation (20keV, $1\times10^{15}cm^{-2}$), LTA favors the interaction between B and O within the Ge melt, clearly visible by the reduction of the oxygen diffusion path with respect to unimplanted samples. It follows that the reaction product is subsequently incorporated into the solid crystal as electrically B–O inactive complexes.

These results need to be carefully considered if LTA process wants to be employed for fabricating *p*-doped Ge-based devices. In particular, they suggest that native oxide must be removed, just before the laser processing.

3.4 Strain characterization

A limited activation for boron and arsenic have been observed as a result of LTA in the melting regime, although a new record was established in the latter case, so demonstrating the capability of LTA to meet technological requirements for As-doped Ge-based USJs down to the 22nm node. Moreover, oxygen contamination penetrating from superficial native oxide have been found to play a key role in preventing an high B activation, while the mechanism responsible for As low activation as well as the role impurities is still unclear. In particular, neither As de-activation correlated with oxygen penetration, nor extended defects above TEM sensitivity have been detected, thus suggesting clusters smaller than 2nm (i.e. with point defects) being responsible for limited activation of As.

Therefore, the aim of this work is clarifying this aspects by characterizing the contaminants behavior and the resulting strain after the LTA previous and subsequent to ion-implantation. Oxygen contaminants in interstitial configuration inducing positive strain are found to penetrate already in the unimplanted samples. In case of B, the inactive B-O clustering are found to induce negligible strain, while a tensile strain assigned to B-B precipitates is observed in the region close to the maximum melt. On the contrary, clustering mechanism by vacancy interaction, which compensates the substitutional compressive strain and also modifies the oxygen configuration, is proposed as being responsible for the partial activation of As observed. Finally, a small fraction of As-rich clusters is inferred by APT.

3.4.1 Results

Figs.3.20 and 3.21 report the chemical and carrier concentration measurements by means of SIMS and SRP respectively, already shown above for As-implanted Ge at 40keV with 2×10^{14}As/cm^2 or 3×10^{15}As/cm^2 and subsequent LTA single pulse at 630mJ/cm^2 or 650mJ/cm^2 for 1 and 10 pulses. As a direct comparison, the corresponding strain $\varepsilon_\perp$ profiles as function of the depth as extracted by the HRXRD measurements around symmetrical (004) RLP are plotted in the panel below (c).

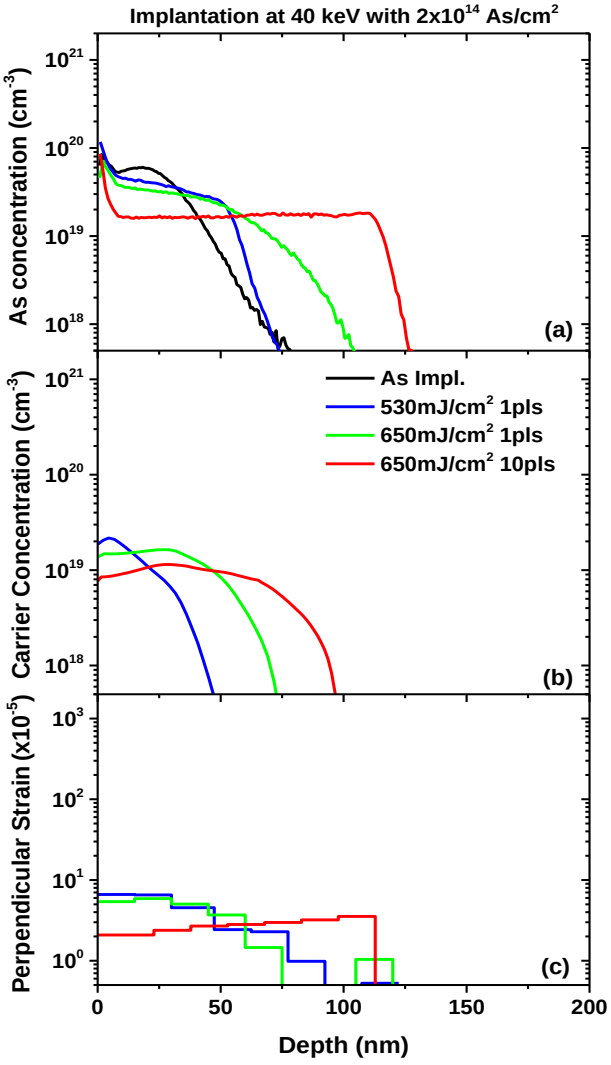

Fig.3.20 Chemical (a), carrier, (b) and strain (c) profiles after implantation with 2×10^{14}As/cm^2 at 40keV and LTA at 530mJ/cm^2 for 1 pulse (blue) and 650mJ/cm^2 for 1 (green) and 10 (red) pulses.

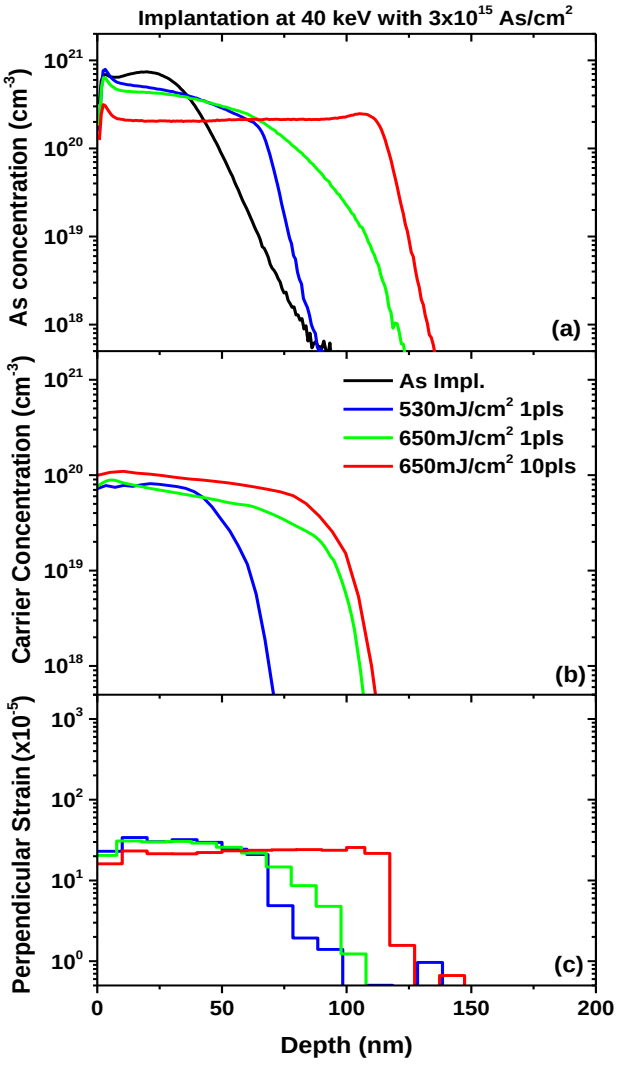

Fig.3.21 Chemical (a), carrier, (b) and strain (c) profiles after implantation with 3×10^{15}As/cm^2 at 40keV and LTA at 530mJ/cm^2 for 1 pulse (blue) and 650mJ/cm^2 for 1 (green) and 10 (red) pulses.

Clearly, the perpendicular strain profiles follow a similar trend that the diffused and the activation profiles. In particular, the strain observed after lower fluence results lower than 10^{-4}, while it exceeds this value of 2-3 times when higher fluence are used. In addition, higher irradiation energies results into deeper melt depths and the resulting strain also extends as well as it becomes of flatter shape after multipulse LTA, according to the redistribution of the dopant.

To check if the regrowth layer is pseudomorfic to the Ge substrate, the parallel lattice parameter of this sample, which shows the largest strain integral among the As-doped sample, was also investigated by measurements around asymmetrical (444) RLP (not reported here). Since no parallel mismatch is observed, we conclude that the doped layer is actually pseudomorphic, i.e. it induces only tetragonal distortion on the Ge host lattice along the direction perpendicular to the growth plane. As a result, we can focus only to the perpendicular strain for the following considerations and only symmetrical measurements are sufficient to determine $\varepsilon_\perp$ in every samples by using the elasticity theory.

As a direct comparison, the $\varepsilon_\perp$-profiles after irradiating unimplanted sample with analogous LTA condition (1 and 10 pulses at 650mJ/cm^2) are included in the same figure (fig.3.22). Unexpectedly, a weak strain is detected even without any doping (about 3 times smaller than that observed in As-implanted sample), being clearly positive (i.e. in-plane compressive).

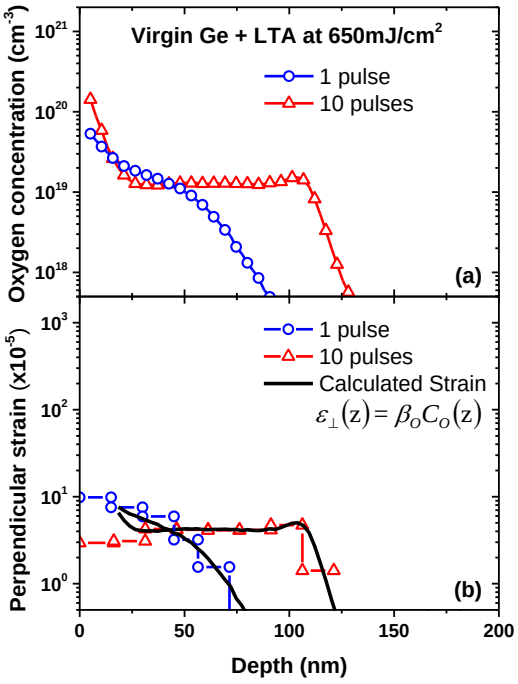

Fig.3.22 (a) SIMS and (b) HRXRD data after LTA at 650mJ/cm^2 1 (circles) and 10 pulses (triangles) on unimplanted Ge sample. Strain simulations for interstitial oxygen calculated by DFT[Coutinho2000] are also included (black line).

Seeing as the impurity penetration from the surface into the uniplanted Ge, the recorded $\varepsilon_\perp$-profiles is simulated by starting from the oxygen chemical concentration as function of the depth $C_O(x)$ as measured by SIMS according to a direct scaling law (black line in fig.3.22b):

$$\varepsilon_\perp = \beta_O C_O(x) \qquad (3.5)$$

where β_O is the fitting proportionality coefficient, namely the strain per atom, preferably reported in terms of the lattice volume modification per atom ΔV (i.e. the atomic volume modification referred to the relaxed lattice), as being directly comparable with the literature. It can be obtained from β by the formula, as deduced by Ref.[Bisognin2010]:

$$\Delta V = \frac{a_{Ge}{}^3\left(1+\frac{\beta\rho_{Ge}C_{11}}{2C_{12}}\right)^3 - a_{Ge}{}^3}{8} \qquad (3.6)$$

where a_{Ge}, ρ_{Ge}, C_{11} and C_{12} are lattice constant, density (in cm^{-3}), and the elastic constant of Ge, respectively. So that the experimental value obtained in unimplanted samples subsequent to LTA results equal to $\Delta V_O = +17.3 \pm 0.2 Å^3$, which is very close to the value of $+15.6 Å^3$ obtained by DFT calculation for interstitial oxygen.[Coutinho2000] Hence, the observed strain is assigned to oxygen impurities occupying interstitial placement inside the regrown Ge lattice, which is the only detected source in the unimplanted sample.

On the other hand, as regarding the total strain observed in the implanted samples after LTA (fig.), both oxygen contaminants and dopants are simultaneously present and the electrical activation of As is found to be partial, so either electrically active (i.e. placed in substitutional position and obtained by SRP) and inactive dopant (i.e. clustered and namely the subtraction of SRP values to the total chemical concentration as measured by SIMS) are expected to induce strain with different contribution. For simplicity, forasmuch as the resulting $\varepsilon_\perp$ again shows a box-shape profile in samples processed with 10 pulses, the maximum As substitutional concentration As_s as well as the corresponding clustered one As_{cl} at the same depth are plotted as function of the corresponding measured perpendicular strain for each samples (fig.3.23a), in order to investigate the trend in a wide range of irradiation conditions (energy density and number of pulses).

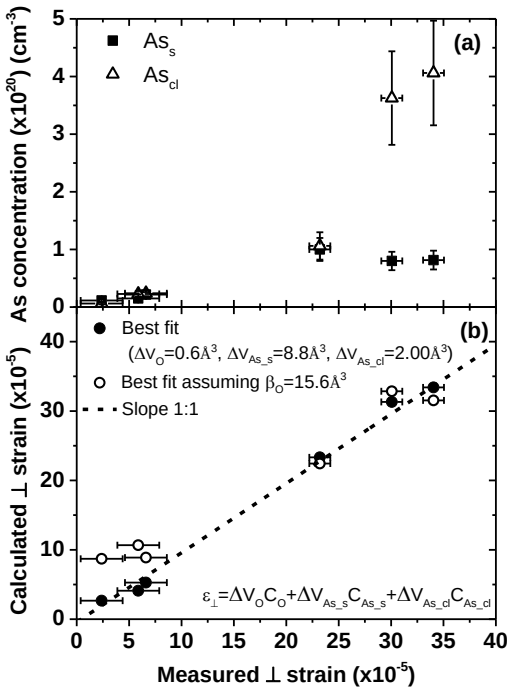

Fig.3.23 Samples implanted at 40keV with 2×10^{14}As/cm^2 and 3×10^{15}As/cm^2 after LTA with 1 pulse at 530mJ/cm^2, 1 pulse at 650mJ/cm^2 and 10 pulses at 650mJ/cm^2. As function of measured perpendicular strain, (a) the maximum carrier concentration (i.e. in substitutional position) as measured by SRP (squares) and the corresponding inactive concentration (likely in cluster form) (triangles) obtain as difference between total chemical concentration as measured by SIMS and active one; (b) calculated perpendicular strain on the hypothesis of being independently produced by substitutional, clustered As and oxygen in interstitial form (open circle) or giving negligible contribution (closed circles).

Given that no linear behavior for none of As_s or As_{cl} is evidenced, $\varepsilon_\perp$ is clearly uncorrelated with only As_s or As_{cl}. Consequently, it is analyzed under the hypothesis of a linear combination of the different strain sources including oxygen. The outputs of this analysis, similarly to the case depicted above for unimplanted samples, are the ΔV_x coefficients of the linear relation between strain and the concentrations C_x of each species *x*, with *x* referring to subtitutional dopant, clustered dopant or oxygen alternatively. Fig.3.23b reports the calculated $\varepsilon_\perp$ as a function of the corresponding measured values according to the best fitting. It is remarkable that the strain behavior is described by a unique set of parameters ΔV_{As_s}=+8.8±0.6Å^3, ΔV_{As_cl}=+2.00±0.04Å^3 and ΔV_O=+0.6±0.9Å^3≈0Å^3, suggesting the same mechanism of deactivation both in the high and low fluence sample as well as in single or multipulse regime. Additionally, the oxygen contribution is found to be negligible, as a result only two contributions, namely from active and inactive As, are able to reproduce the strain behavior in a wide range of experimental condition.

So as to prove the general validity of this practical analysis, the same method is applied to describe the HRXRD spectrum collected on Ge implanted at 20keV with 1×10^{15}B/cm^2 and subsequent 10 pulses of LTA. The corresponding electrical and chemical concentration profiles of B and O (also described above) are reported in fig.3.24a. together with the extracted $\varepsilon_\perp$-profile as shown below in fig.3.24b. Evidently, the strain results negative (i.e. in-plane tensile) within the regrowth layer, at variance with respect to un- or As-doped sample. In particular, a negative peak of strain is observed in correspondence to the pile-up region and it reverses abruptly to positive values beyond the maximum melt depth. Such a difference between B and As is expected from the dopants and matrix covalent radii (also reported in tab.3.1) which are much smaller for B, and similar for As, with respect to that of Ge.[Pyykkö2012] In both systems anyhow, the observed strain profiles follow the redistribution of the dopants.

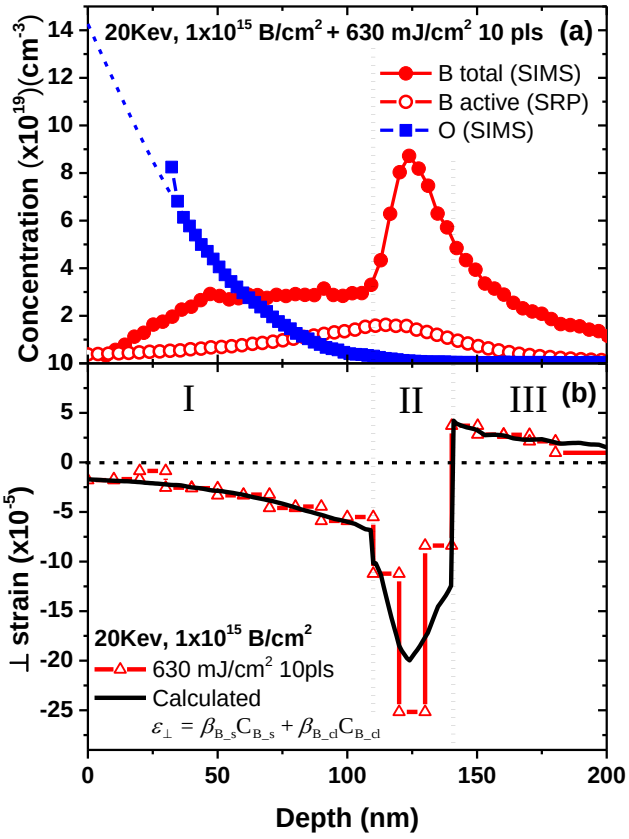

Fig.3.24 Characterization of sample implanted with 1×10^{15}B/cm^2 at 20keV and subsequent 10 pulses of LTA at 630mJ/cm^2 (a) Chemical (closed circles) and electrically active (open circles) B as measured by SIMS and SRP, together with oxygen concentration profile of fig.3.18. (b) Perpendicular strain profile as measure by HRXRD (open triangles) and by calculation on the hypothesis of being independently produced by both substitutional and clustered B.

Once again, by using the concentration of active and inactive dopant as well as of oxygen impurity as inputs, the strain behavior can be reproduced. The resulting fit of the $\varepsilon_{\perp}$-profile for the B-implanted sample after LTA is included in fig.3.24b, while the output (the ΔV coefficients) are reported in tab.3.1 together with the values obtained for the As-doped and unimplanted Ge. More precisely, three regions with different strain behavior can be distinguished, on the basis of the contribution for inactive B.

The observed negative strain in the region I (superficial layer ~110nm thick), where the sample was rapidly molten and regrown by LTA, can be nicely fitted assuming the literature value of B occupying substitutional site ΔV_{Bs}=-12.3±0.5Å^3[Bisognin2010] and relatively small ΔV values for the other possible strain sources, i.e. ΔV_{Bcl}=-1.4±0.2≈0Å^3 and ΔV_O=-0.7±0.7≈0Å^3 .

The region II (between about 110nm and 140nm) is where the pile-up phenomenon occurs. No oxygen in this region is present in significant concentration, so only one additional contribution from the large amount of inactive boron is included in order to fit the experimental $\varepsilon_{\perp}$-profile, giving a ΔV_{Bcl}=-7.6±0.5Å^3. Such a negative value corresponds to a lower magnitude of tensile strain than ΔV_{Bs}. So, analogously to what observed in Si,[Bisognin2007] it was assigned to strain induced by precipitation of small B-B clusters that are likely favored by the more open covalent structure of germanium achieved in undercooled condition close to the maximum melt depth (also favoring the pile-up).[Fisicaro2013]

In the region III (i.e. beyond ~140nm) ΔV_{Bcl}=+9.3±0.2Å^3, i.e. boron clusters induce positive strain in the lattice. This is close to the value reported in literature for Boron Interstitial Clusters (BIC) observed after ion-implantation and conventional annealing (ΔV_{Bcl}=+14.8±1.7Å^3).[Bisognin2010] Indeed, in this region no melting due LTA has occurred, thus boron clustering presumably occurs through the interaction of boron with the residual ion-implantation damage. The lower value with respect to literature is consistent with smaller clusters (thus inducing lower strain) as expected due to the reduced thermal budget of LTA beyond the maximum melt depth.

	ΔV_{subst} (Å^3)	$\Delta V_{clusters}$ with O (Å^3)	$\Delta V_{clusters}$ Pile-up (Å^3)	$\Delta V_{clusters}$ beyond max melt depth (Å^3)	$\Delta V_{clusters}$ (Å^3)	ΔV_{Oxygen} (Å^3)	r_{cov} (pm)
Ge undoped	--	--	--	--	--	+17.3±0.2	122
As	+8.8±0.6	--	--	--	+2.00±0.04	+0.6±0.9	117
B	-12.3±0.5 [Bisognin2010]	-1.4±0.2	-7.6±0.5	9.3±0.2	+14.8±1.7 [Bisognin2010]	-0.7±0.7	88

Tab.3.1 Summary of the lattice volume modification measured in Ge in this thesis work.

Among the outputs collected in tab.3.1, it is interesting that the best fit is obtained with systematical negligible contribution from the oxygen both for B-and As-doping after LTA, at remarkable variance with the corresponding value observed in the unimplanted Ge. As long as the previous studies assigned to oxygen contaminants the de-activation of B through B-O clusters formation in the region-I, the HRXRD data suggest that those small clusters (not observed by TEM) weakly interact with the Ge lattice, so inducing negligible tensile strain as well as preventing oxygen to assume the interstitial configuration. Instead, the fact that the best fit is obtained with a lattice volume modification per oxygen atom far fewer than the one calculated by *Coutihno at al.*[Coutinho2000] is quite surprising as regarding sample with As, where no As-O interaction is observed (fig.3.18), on the base of diffusion and As activation considerations. So a fundamental question about the origin of the change in ΔV_O due to presence of As is raised: which is the microscopic configuration of oxygen in the As-implanted samples after LTA?

To consistently explain the experimental data and the change in oxygen configuration in particular, a mechanism occurring in the solid phase in the first stage of cooling down (near the melting temperature T_m=1211K for a maximum time t ~100ns) is proposed. In particular, the characteristic migration time (CMT), i.e. the average time for a single migration step, is semi-quantitatively evaluated as:

$$CMT = \frac{1}{\nu_0} e^{\frac{Em}{K_b T_m}} \quad (3.7)$$

where (ν_0=9×10^{12}Hz) is the phonon frequency, K_b is the Boltzmann constant and E_m is the migration that is 2.08eV for single atom O_i or 1.48eV for dimer oxygen dimer O_{2i} interstitially diffusing. According to our calculations, CMT for O_i and O_{2i} are both too large (at least 160ns in the latter case) and so they are expected to be migrationless in this regime. Therefore, the configuration changing as a result of LTA subsequent to As-implantation must be treated assuming that the immobile oxygen is a trap for another mobile specie related with As, which is not present in the unimplanted Ge. This specie could be the AsV pair that is expected to be spontaneously favored by reduction of the local strain energy and, when formed, to mediate also deactivation through clustering of As in the solid phase in the first stage of cooling (as usually observed in diffusion experiments at the equilibrium conditions):[Brotzmann2008]

$$AsV + As \rightarrow As_2V \quad (3.8)$$

In addition, the role played by AsV in the experiment is supported on the basis of its relatively low migration energy (0.99eV), corresponding to an estimated CMT of ~1.5ns, thus suggesting that migration can effectively occur within the cooling stage. In this case, the mobile AsV trapping by oxygen is expected to form an inactive AsVO cluster, which is calculated having a stable binding energy of about ~1.27eV.[Chroneos2012] However, kinetic considerations for the mobile species AsV lead to a characteristic migration length (CML) of about 1.2nm given by the formula:

$$CML = \sqrt{2t \frac{\nu d_{NN}^2}{6} e^{-\frac{E_m}{KT_m}}} \quad (3.9)$$

where d_{NN} is the Ge nearest neighbor distance. For comparison, oxygen atoms have minimum averaged half distance between each other $<d_{O\text{-}O}/2>$ of about ~2nm, corresponding to the reciprocal of the maximum impurity concentration ($\lesssim$2×10^{19}cm^{-3}). Thus, the AsV pair hardly can reach an oxygen atom. Moreover, no correlation between oxygen and As deactivation is experimentally detected, hence ruling out the hypothesis of AsVO formation. In the same way, the As concentration in low fluence samples is close to oxygen one and partial electrical activation is anyway recorded.

Therefore, an indirect role of the mobile pair is proposed via its recombination into substitutional arsenic As_s and releasing a vacancy V:

$$AsV \rightarrow As_s + V \quad (3.10)$$

This possibility is supported by a recombination time on the order of ~40ns within a cooling time of ~100ns, calculated on the basis of the AsV binding energy (1.34eV).[Chroneos2014] In this description, the trapping of V by an oxygen more probable (CML~7nm) an it forms a so-called A-center (vacancy-oxygen pair)[Chroneos2012], so explaining its change of the configuration. In fact, the formation energy of VO is more than 3eV in Ge[Coutinho2000], but it also has a stable binding energy of about 0.45eV[Chroneos2012], which makes VO likely to form as a result of non-equilibrium solidification. In addition, the vacancies released by recombination are expected to assist also the As deactivation trough a dopant-defect clustering phenomenon indirectly directly via:[Chroneos2014]

$$V + AsV \rightarrow AsV_2 \quad (3.11)$$

Experimentally, the body evidence of the mechanism proposed above is the ΔV reduction, which reveals that the reduction of the strain energy through a vacancy interaction is the driving force. Indeed, the ΔV for clustered As (ΔV_{As_cl}=2.00±0.04Å^3) is about 4 times lower than for substitutional As (ΔV_{As_s}=8.8±0.6Å^3). The present result indirectly suggests that the As-V complex is responsible for deactivation analogously to the mechanism observed in Si.[Borot2007] The parallelism between Si and Ge is clear when comparing the present lattice volume modification data for B- and As-doping of Ge by LTA with the conventional ones reported in literature also for both Si and Ge (fig.3.25). Very interestingly, lattice expansion is found for substitutional B and maintained for small B-B clusters in Ge and also in Si. Instead, ΔV turns to positive values when larger BICs grow. In case of arsenic, opposite behavior is observed both in in Si and Ge, thus supporting the occurrence of V-clustering mechanism. Nevertheless, despite residual supersaturation of vacancies was directly measured in unimplanted Si as a result of LTA[PRBLaMagna07], the present experimental data suggest that, if established, the supersaturation produced by LTA in Ge is likely to decrease towards the equilibrium in a very short time, as no residual vacancies interacting with oxygen are observed in the unimplanted Ge where all of the oxygen is found to be in interstitial configuration.

In case of arsenic, vacancy dynamic is likely very changed: the presence of arsenic that forms the mobile AsV species acts as reservoir for vacancies, so being stabilized in this form and released within longer CMT. Moreover, the AsV binding energy can reduce the effective energy cost for V formation increasing the total amount of vacancies. Therefore, it is likely that As indirectly increases the V-O interaction by acting on the V population and dynamic while no direct As-O interaction occurs.

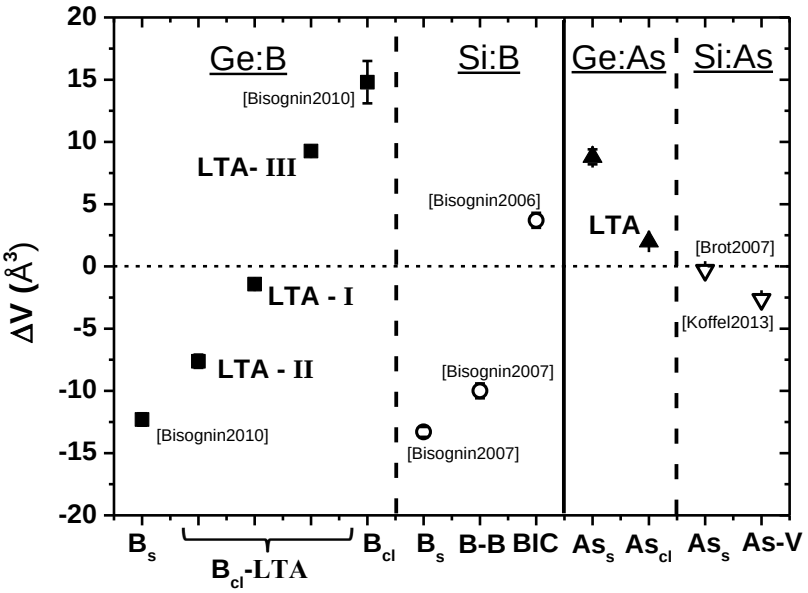

Fig.3.25 Summary of the lattice volume modification measured in Si (open symbols) and Ge (closed symbols) when doped with B (squares) or As (triangles).

Last but not least, from the estimated CMT only V-rich clusters are expected to form at low fluence, according to (3.11). Conversely, since our calculations show that AsV diffusion is faster than its recombination, some As-rich clusters formed according to the (3.8) might be observed in the high fluence sample where the CMT of the mobile pair is predicted comparable to $<d_{As\text{-}As}/2>\sim$1nm (for As concentration of $\sim 1\times10^{20}$cm^{-3}). In particular, this contribution might be responsible for the observed saturation trend in the As electrical activation. However, HRXRD data are well described by a unique ΔV_{As_cl} for both low and high fluence. The explanation could lie on the unfavorable As-As configuration in the Ge lattice (as well as in Si) as calculated by DFT,[Chroneos2007] which would result always into a V-mediated interaction also in As-rich clusters. In other word, similar long-range $\varepsilon_{\perp}$ is expected for both the two kind of clustering and no information about the local ordering can be obtained from HRXRD.

Nevertheless, the prescience of AsV-rich clusters was tested by APT measurement on the high fluence As-implanted samples after 1 and 10 pulses at 650mJ/cm^2. No clusters can be directly observed by the 3D reconstruction, because of their very small size in comparison with the APT sensitivity, as expect for LTA that is a very fast process and thus reduces the Ostwald ripening. However, statistical analyses based on nearest neighbor (NN) distribution can be used to investigate the presence of clustering, as reported in figs.3.26a and 3.26b. Especially, the experimental NN distribution calculated for the sample subjected to 1 pulse resulted shifted towards lower distance values, if compared with the respective randomized one, so indicating that some short-range order between As atoms exists. Instead, this shift is less pronounced in the sample irradiated with 10 pulse, so suggesting a lower clustering phenomenon.

In order to find the As concentration in form of clusters, first of all the maximum separation method was employed by fixing the minimum number of As that defines a significant cluster N_{min} to a sufficiently high value (5 atoms not to wrongly include smaller false clusters). In this way, one obtains the cluster count distribution as function of d_{max}, namely the maximum As-As distance within the cluster (figs.3.26c and 3.26d). Since some counts could simply be the result of random fluctuations, the same procedure was applied to a random data set obtaining a significant difference with respect to the experimental one (also reported in the figures). Then, d_{max} was fixed to values maximizing the difference with the random distribution, i.e. 1.5nm and 1.6nm for 1 and 10 pulse respectively, so as to determine density and chemical composition of the clusters thanks to the double maximum separation method Finally, the concentrations of As in form of clusters rich with more than 5As/cluster, are estimated $(7.5\pm3)\times10^{18}$cm^{-3} for the single and and $(4.5\pm3)\times10^{18}$cm^{-3} for the multipulse LTA processing. Such values are large enough to be indirectly detected by APT by means of the descripted procedure and they correspond to about the 1.9±0.8% and 2.2±0.8% of the inactive As measured by SIMS and SRP in both the regimes for 1 and 10 pulses, respectively.

It is noteworthy that a weak difference with the random cluster count distribution is obtained for the multipulse sample at variance with the single pulse data, thus indicating a smaller cluster dimension in this former case (fig.3.26d). Correspondingly, the APT measurements results of a lower sensitivity and therefore a larger relative error is provided. We can speculate that this is because of the As redistribution as a result of LTA, which increased the $<d_{As\text{-}As}/2>$ and consequently reduced the clustering probability.

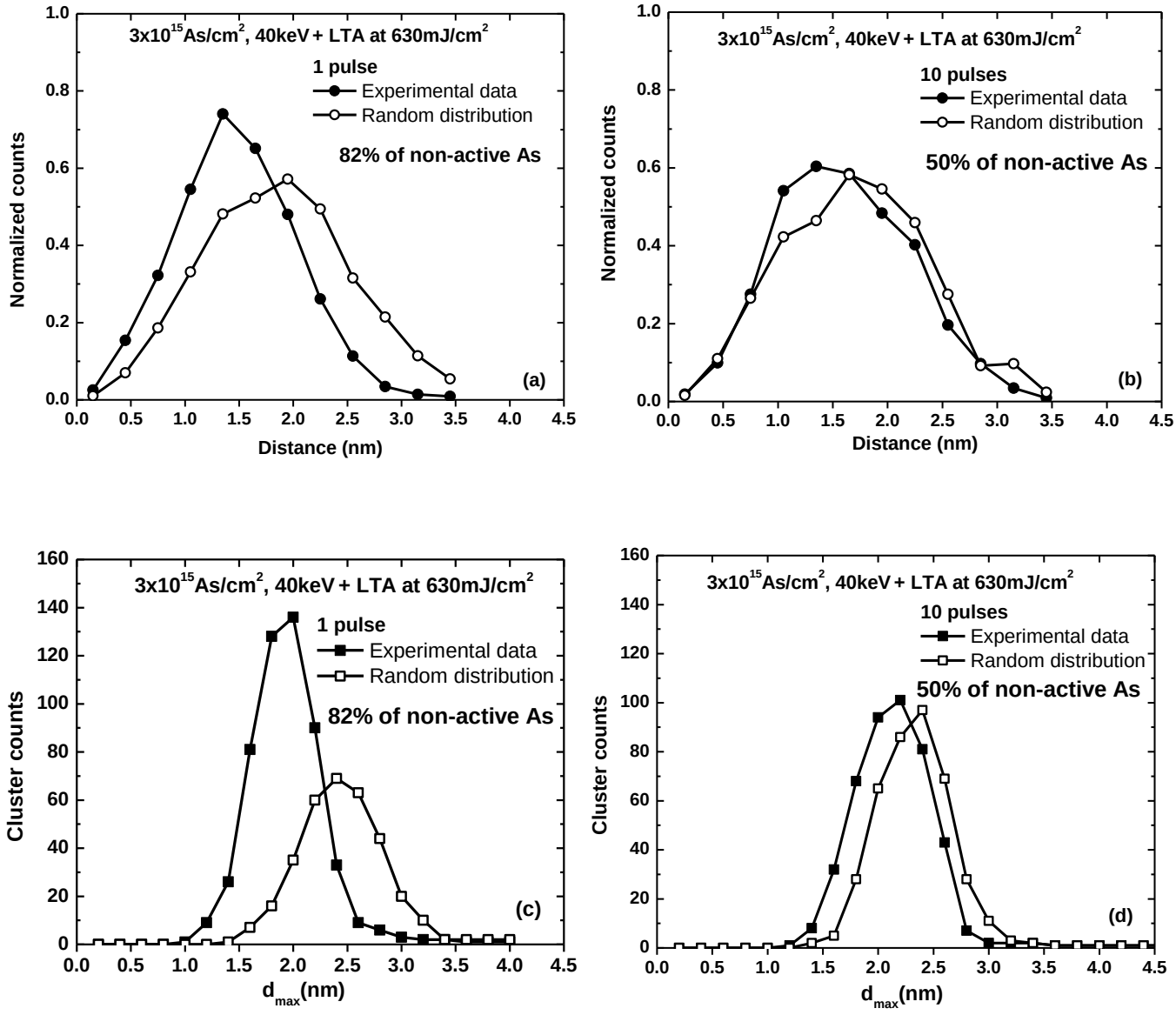

Fig.3.26 Experimental (closed symbols) and random (open symbols) NN (circles) distributions and cluster counts distribution (squares) of the sample implanted at 40keV with 3×10^{15}As/cm^2 after LTA processes with 1 (a) and (c) as well as 10 pulses (b) and (d) at 650mJ/cm^2 The ordinate axis is an arbitrary histogram count normalized for each curve to allow comparison.

In order to describe the APT data as well as the recorded electrical activation, a simple model was developed starting from the kinetical consideration explained above and assuming that the (3.8) is the dominating mechanism at these fluence. Indeed, if random migration of AsV is assumed, the cluster formation is dominated by the encounter probability of AsV with other As species. We can consider the probability *W* of having *k* encounters as given by the binomial distribution:

$$W_{n,p}(k) = \binom{n}{k} p^k (1-p)^{n-k} \qquad (3.12)$$

where *p* is the encounter probability, being roughly equal to the As concentration (~1.13% and (~0.50% for the single- and multi-pulse sample respectively), while *n* is the effective number of migration steps. After *k* encounters, under the hypothesis that cluster are stable during the cooling time as suggested their stable binding energy (being larger than 1.22eV as calculated by DFT method [Chroneos2012]), a cluster of a=k+1 As atoms forms. Therefore, the fraction of As embedded into clusters larger than one As atom can be estimated by means of:

$$f(a) = \frac{\sum_{k=a-1}^{\infty} (k+1) W_{n,p}(k)}{\sum_{k=0}^{\infty} (k+1) W_{n,p}(k)} \qquad (3.13)$$

Thus, *f(5)*, namely the fraction of clusters having at least 5 As atoms, can be compared with APT data, as well as with *f(2)*, i.e. with the total inactive fraction recorded by SIMS and SRP (tab3.2). In particular, it was noted that both *f(5)*≈2% as well as the observed activation fraction are satisfactory reproduced for both of the samples by choosing a unique *n*=75±5, which is in good agreement with the CMT~1.5ns for AsV (n≈100ns/CMT≈67).

n=75	***f(2)***	**Total inactive fraction** (SIMS-SRP)	***f(5)***	**Inactive fraction** (APT)
1 pulse (*p=0.0113)*	77%	82±4%	3.1%	1.9±0.8%
10 pulses (*p=0.005)*	61%	47±4%	0.7%	2.2±0.8%

Tab.3.2 Inactive fractions as measured by SIMS-SRP and APT and kinetically estimated by random encounter probability.

3.4.2 Conclusions

The residual $\varepsilon_{\perp}$ is characterized by HRXRD and modeled as linear combination (i.e. independent contribution) of all the different species concerned. The resulting fitting parameters suggest that oxygen occupies interstitial configuration within the unimplanted Ge after LTA, so inducing compressive strain. After B implantation, the precipitation of inactive B-O clusters formed in the liquid phase are found to induce negligible strain likely due to their small dimension and a strain assigned to B-B precipitates is observed in the pile-up region at near the maximum melt depth. In case of LTA after As implantation, the spontaneous formation of AsV pair and its recombination is believed to promote a delayed vacancy supersaturation, which is responsible both for changing in the natural oxygen configuration and for partial As activation by means of vacancy interaction observed in a wide range of laser annealing conditions (energy densities and number of pulses) and fluences ($2\times10^{14}cm^{-2}$ or $3\times10^{15}cm^{-2}$). Additionally, an AsV-mediated deactivation mechanism leading to a saturation in the As electrical activation beyond concentration of $\sim1\times10^{20}As/cm^{3}$ is supposed to takeover in the latter case. This hypothesis is supported by APT measurements detecting a fraction of inactive As (about 2%) in form clusters larger than 5 atoms, which is compatible with the characteristic diffusion time of the mobile specie as well as satisfactory described by an AsV-As random encounter probability.

3.5 Thermal stability

Thermally stable Ge-based USJs capable of bearing further steps of the device fabrication sequence are required for a complete replacement of Si in semiconductor industry. Being LTA a highly out-of-equilibrium process, thermal stability might be a remarkable issue, not only due to solubility considerations, but also in view of possible effects related to residual vacancy defects after LTA [Bruno2012]. So, the effects of post-processing by conventional furnace annealing (FA) has been investigated on Ge samples where the highest levels of As activation (~1×10^{20}As/cm^2) was obtained, by ion implantation and LTA (see the previous section).

The electrical activation of As significantly reduces after annealing already at temperatures as low as 350°C, with negligible diffusion. HRXRD analyses, together with SRP, APT, and SIMS characterization, point towards a structural evolution during annealing of the clusters containing As, where interaction with vacancies plays a major role.

In addition, also B-implanted Ge at 20keV with high fluence (1×10^{16}B/cm^2) and subsequent LTA at 630mJ/cm^2 for 1 and 10 pulses was post-annealed with the aim of improving the electrical activation by dissolving the B precipitates. However, these clusters resulted stable up to the remarkable temperature of 600°C.

3.5.1 Arsenic

Two starting samples were selected from those having the highest As active concentration obtained in the previous section. They were implanted at 40keV with 3×10^{15}As/cm^2 and, after native oxide removal by dipping in hot de-ionized water, processed by LTA with 1 pulse or 10 pulses at 650mJ/cm^2, both reaching a maximum electrically active concentration of ~1×10^{20}As/cm^2. The samples are then further annealed by FA thermal cycles using an Anton Paar DHS 900 hot stage in N_2 atmosphere. Each step consisted of a 100°C/min heating ramps starting from the room temperature (~25°C), up to the chosen post-processing temperature kept for 10 minutes before the subsequent complete cooling phase, which exponentially decay with a characteristic time on the order of ~100°C/min. In this way, temperatures of 50, 100, 150, 200, 260, 300, 350, 400 and 450 were investigated.

Fig.3.27 shows the SRP measurements characterizing temperature evolution of carrier concentration profiles of Ge samples subjected to LTA for 1 pulse (Fig.3.27a) and for 10 pulses (Fig.3.27b), before and after post-LTA annealing. As already mentioned, the starting profiles after LTA, already reported in the previous experiments, show remarkably high maximum electrical activation (up to ~1×10^{20}As/cm^3) as a result of the laser irradiation. Upon FA, the two LTA conditions show the following similar behavior: annealing at 260°C for 10 minutes (circles) does not significantly change the activation, which results still high; after 10 min at 350°C (triangles), a substantial deactivation down to ~5×10^{19}As/cm^3 is instead observed. Since this value represents the maximum activation of As obtained with non-melting annealing processes, and the theoretical solid solubility of arsenic in Ge is (~8×10^{19}As/cm^3), this post-LTA process is sufficient to suppress all the advantages of melting LTA in terms of electrical activation. At 450°C (revers triangles), the profiles slightly reduce further and become also shallower by about 15nm.

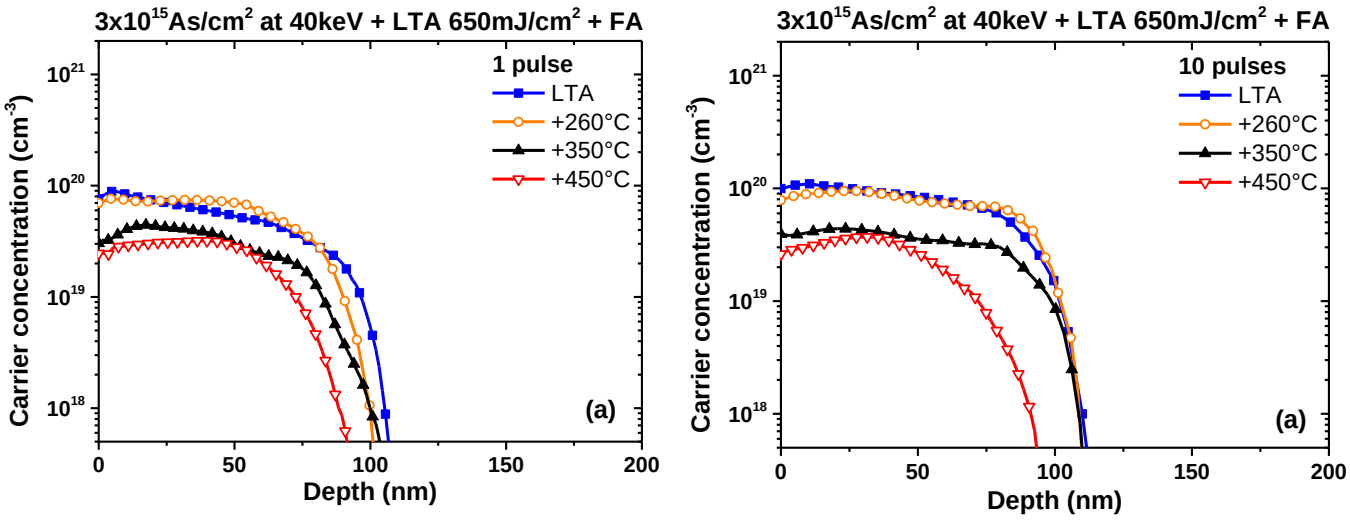

Fig.3.27 Temperature evolution of the carrier concentration profiles as measured by SRP in samples implanted with 3×10^{15}As/cm^2 at 40keV and irradiated with LTA at 650mJ/cm^2 with single- (a) and multi-pulse (b).

Fig.3.28 shows the SIMS chemical As concentration depth profiles before and after post-LTA conventional thermal annealing at 450°C, compared with the corresponding SRP carrier concentration depth profiles already reported above in fig.3.27. No in- or out-diffusion of the dopant is observed, so the dopant fluence is conserved. Indeed, the 10 pulses sample shows a slight shrinkage in the post-annealed SIMS profiles with respect to the sample after LTA. However, it has to be considered that the two measurements are relative to different LTA spots, and such a small difference is compatible with the irradiating energy differences (being less than 5mJ/cm^2) between the two spots. In any case, its weighs is less than the experimental uncertainty on the fluence estimation that results unchanged after the post-LTA at this temperature.

The absence of diffusion into the substrate is quite surprising for these thermal annealing (10 minutes at 450°C), as the high As concentration should determine high As equilibrium diffusion coefficients due to extrinsic effects. In order to clarify this aspect, simulations of the expected diffusion are also included in the same figure.[Brotzmann2008] These simulations have been obtained thanks to a code written in ANSI-C and developed by our group, which numerically solves the Fick equation in 1D so reproducing the AsV^--mediated diffusion, while considering the temperature dependence of intrinsic carrier concentration reported by Morin and Maita[Morin1954] through the Eqs.1.5-1.7.

In addition, we assumed that the As atoms which can participate to diffusion (and also introduce carriers) are only those that are electrically active after the LTA process. Thus, we assumed as an input the SRP profile after LTA and left the inactive As profile (i.e. obtained as SIMS-SRP) immobile. The diffused profile returned by the code (dashed line in fig.3.28) is then added to the starting immobile profile to obtain the final total profile (continuous line).

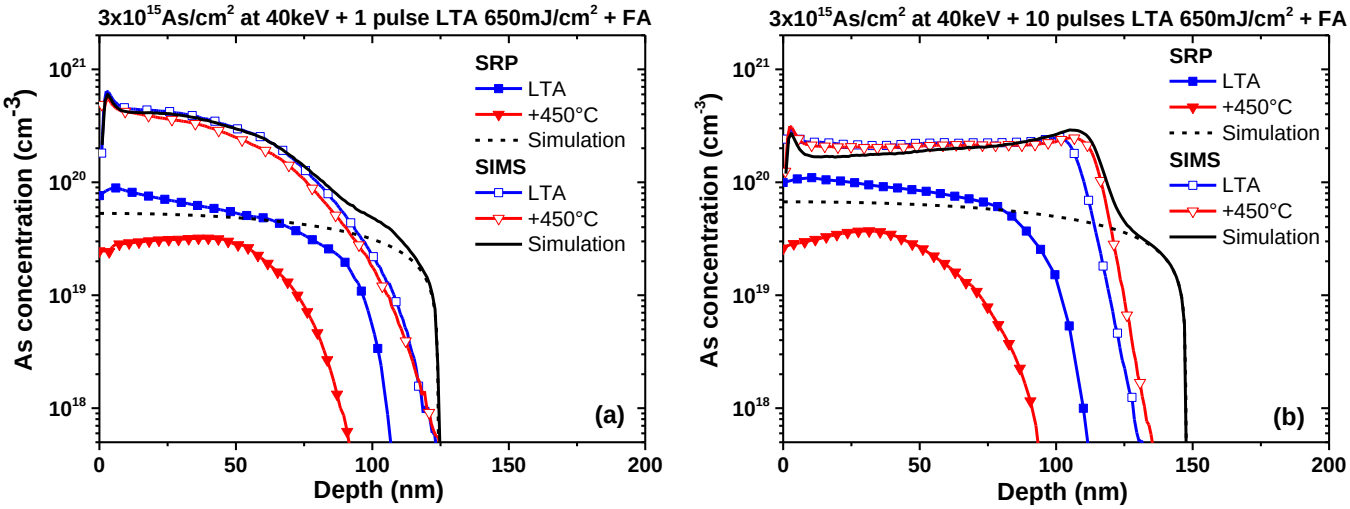

Fig.3.28 Chemical (open symbols) and carrier (closed symbols) concentration profiles as measured by SIMS and SRP respectively in samples implanted with 3×10^{15}As/cm^2 at 40keV and irradiated with LTA at 650mJ/cm^2 with single- (a) and multi-pulse (b). The corresponding profiles after conventional post-LTA thermal treatments at 450°C are also reported (reverse triangles). Simulations are also reported as explained in the text.

Quantitatively, even if clustering beyond the residual activation is included, more than 20nm-broadening would be expected in the SIMS profiles. Since As is known to diffuse via vacancy-mediated mechanism,[Chroneos2014] a first explanation for the lack of diffusion could be the AsV^- inhibition as a result of a lower population of vacancies. However, this is a remote hypothesis in conventional thermal annealing on the basis of the well-known prompt reinstatement of V equilibrium concentration via their injection from free surfaces[Chroneos2014] and, most of all, the suppression of AsV^- should also hinder the donor deactivation reaction, which is clearly occurring instead.

Therefore, a trapping mechanism reducing AsV^- effective diffusion is much likelier as responsible for both the abovementioned effects. Given this consideration, we can conclude that the carrier profile deactivation and shrinking, which is observed at 450°C, most probably occur at the early stages of the annealing, i.e. before any significant broadening of the profile. From another point of view, one might argue that the observed deactivation is not mediated by As diffusion, but that the reason should be searched somewhere else. A possible explanation might consider an excess of vacancies left by the LTA process close to the maximum melt depth,[Bruno2012] which quickly evolves by interacting with As atoms during post-LTA and promotes their clustering.

In order to get further insights, we performed APT investigation of the As 3D distribution. Fig. 3.29 reports the cluster count distributions as deduced by APT statistical analysis before and after post-LTA annealing at 450°C.

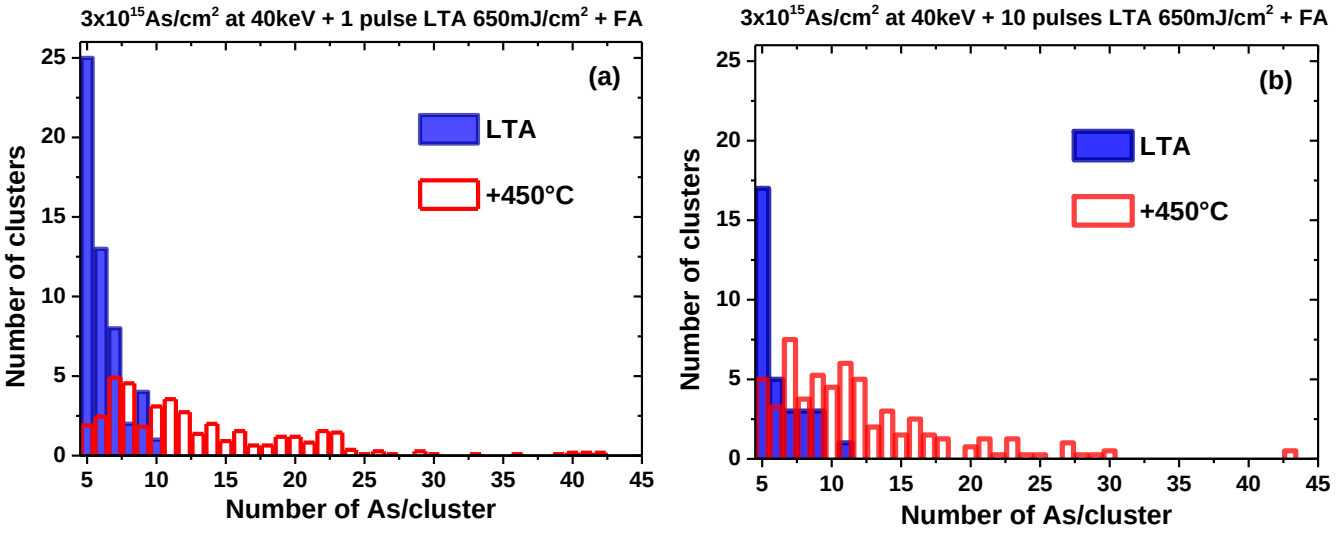

Fig.3.29 Cluster counts distribution as deduced by statistical analysis of APT on samples implanted with 3×10^{15}As/cm^2 at 40keV after LTA at 650mJ/cm^2 (filled bars) with single- (a) and multi-pulse (b) as well as the correspondent data after conventional post-LTA thermal treatments at 450°C are also reported (open bars).

Statistical analysis is necessary because clusters are not directly observed by the 3D reconstruction. Analogously as descripted in the previous section, the maximum separation method with the IVAS software is used after checking that the experimental nearest neighbor (NN) distributions of LTA samples are shifted toward lower values of distance compared with the respective random distribution (not shown), so confirming a short-range ordering between As atoms. Again, minimum number of As atoms defining a significant cluster was fixed to 5 (a sufficiently high value of atoms not to wrongly include smaller false clusters) and the maximum separation distance d_{max} is set as a variable.

With this method, due to the minimum 5 atoms per cluster cut-off, about 3-4% of the inactive As (as measured by SRP and SIMS) are detected in the form of clusters, consisting in bigger size tail of the cluster distribution. The obtained As/cluster distributions pre- and after FA are compared both for single and multipulse sample (fig.3.29). Clearly, a shift toward larger As/cluster values is observed, hence suggesting their dimension is growing along with the As deactivation. Indeed, the estimated density of the clusters is essentially unchanged, being $(1.2\pm0.3)\times10^{-3}nm^{-3}$ and $(0.9\pm0.3)\times10^{-3}nm^{-3}$ respectively for single- and multi-pulse after the thermal post-annealing, while $1.2\times10^{-3}nm^{-3}$ and $0.7\times10^{-3}nm^{-3}$ were measured just after LTA. These observations point towards a mechanism where, during the FA, more As atoms are added to the cluster ensemble formed just after LTA.

Under this hypothesis, the mean free path of the mobile specie AsV^- (λ_{AsV^-}) can be estimated as being reduced by the trapping of the clusters having density *Nc* and averaged capture radius *R* (assumed around 0.5nm):

$$\lambda_{AsV^-} = \frac{1}{\sqrt{\pi R N_c}} \qquad (3.14)$$

Actually, if the *Nc* provided by the APT is used, λ_{AsV^-} results on the order of ≈12nm. However, since the APT reveals only a fraction of the total amount of clusters, the real cluster density is expected to be one order of magnitude larger. In this case, the mean free path of AsV^- reduces to few nanometers. Thus, suggesting also a consequently inhibition of the long range As diffusion.

In order to gain more information on the clustering mechanism, *in situ* HRXRD around symmetrical (004) reciprocal lattice point have been performed. In particular, the RCs after each annealing cycle are obtained by the 5 RCs approximation method (described above in the experimental section). The results are reported in fig.3.30 together with the measurements just after the LTA.

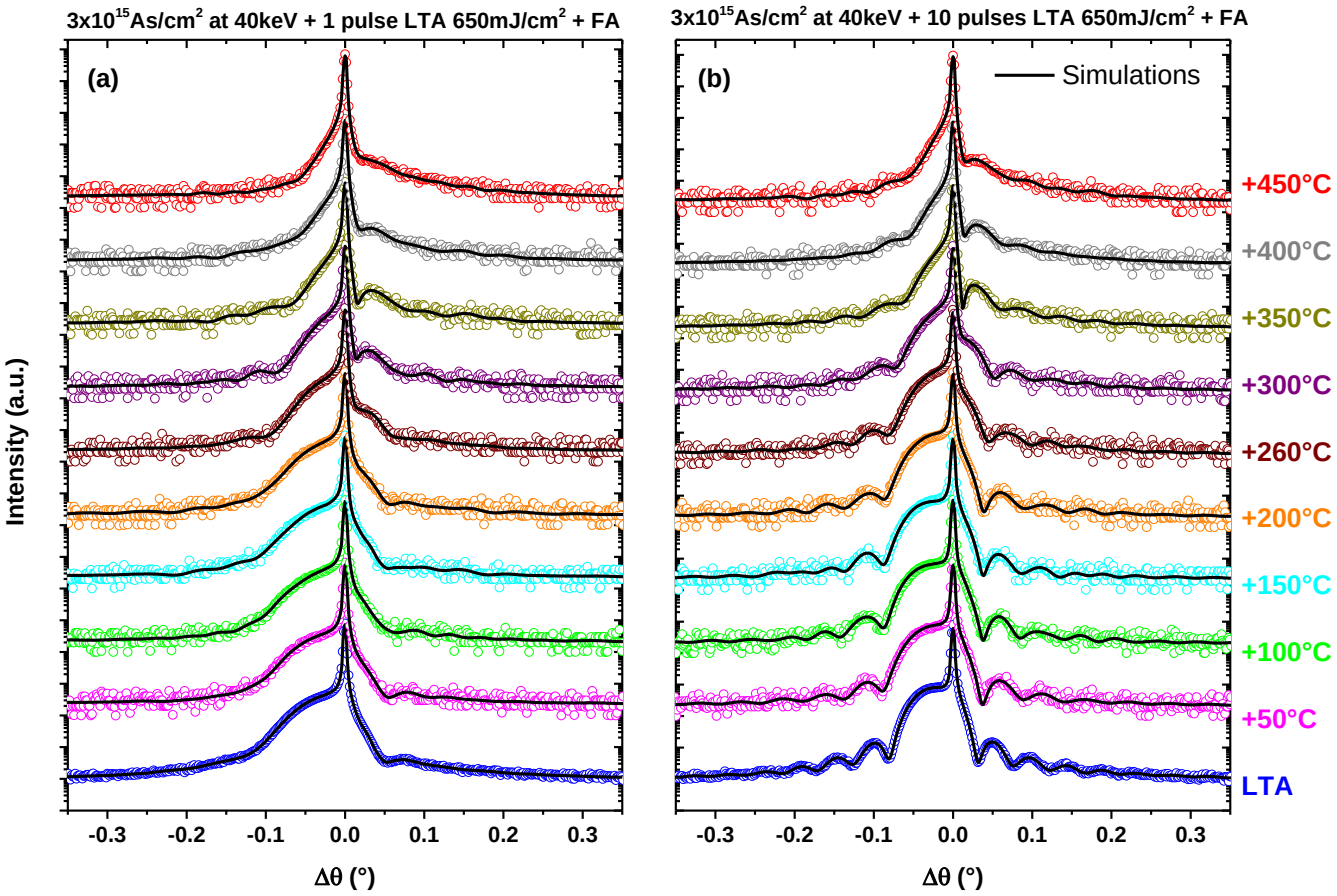

Fig.3.30 Thermal evolution of rocking curves for implanted with 3×10^{15}As/cm^2 at 40keV after LTA at 650mJ/cm^2 with single- (a) and multi-pulse (b) from RT to 450°C for 10 minute each (open circles). Solid lines represent the best and simulations of the HRXRD spectra.

The shoulder visible at negative angles clearly shifts towards positive angles by increasing the annealing temperature indicating a progressive change in the lattice parameter, particularly around 260°C. As long as the secondary peaks existence (interference fringes) in the RCs, epilayer pseudomorphicity vincula stability is suggested and accurately verified by recording no lateral mismatch on asymmetric RLM around (444) reflection at 450°C in the sample after 10 pulses (not reported). Thus, given the absence of any epitaxial constraint relaxation, the perpendicular strain $\varepsilon_{\perp}$ can be directly obtained by symmetrical measurements with the help of elasticity theory.

The simulations in the framework of dynamical theory are included in the same figure above (black lines). They have been obtained by starting from the strain profile measured just after LTA and letting the fitting procedure to minimize the residuals. In particular, the 15nm-sublayer partition has been kept constant and only the perpendicular strain was left free to vary. Only close to the maximum melt depth also the width was optimized, in order to be sensitive to a possible variation of the thickness of the strained region. It can be noticed that the best fits are of excellent quality and the obtained $\varepsilon_{\perp}$ profiles are shown above in fig.3.31.

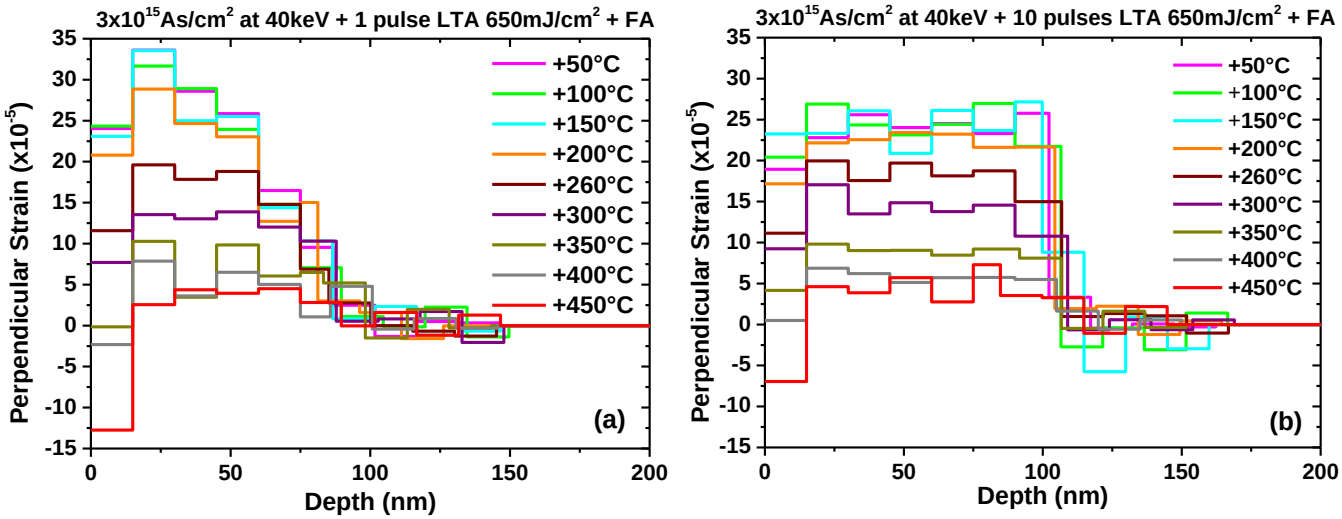

Fig.3.31 Thermal evolution of the perpendicular strain as extracted from the RC simulations for implanted with 3×10^{15}As/cm^2 at 40keV after LTA at 650mJ/cm^2 with single- (a) and multi-pulse (b) from RT to 450°C for 10 min each.

Clearly, a gradual perpendicular strain reduction is observed heating beyond 200°C both single and multiplulse irradiated sample, consistently with shift of the layer Bragg peak toward positive angle in the experimental RCs. Especially near the surface, a layer of pronounced reduction in the compressive strain is detected, becoming even of tensile nature beyond ~400°C. Correspondingly, a secondary interference fringe growing at $\Delta\theta$~+90arcsec with respect to the substrate is detected in the experimental RCs. Especially from the $\varepsilon_{\perp}$ profiles of the 10 pulses sample, no significant shrinkage of the strained region (within ~15nm) is evident, rather an homogeneous ~100nm-thick layer decreasing is observed.

Thus, in analogous way as done in the previous experiment, information obtained from the different techniques (chemical and carrier concentration) have been extracted at an intermediate depth (~20nm) and compared with the corresponding perpendicular strain as function of temperature (fig.3.32).

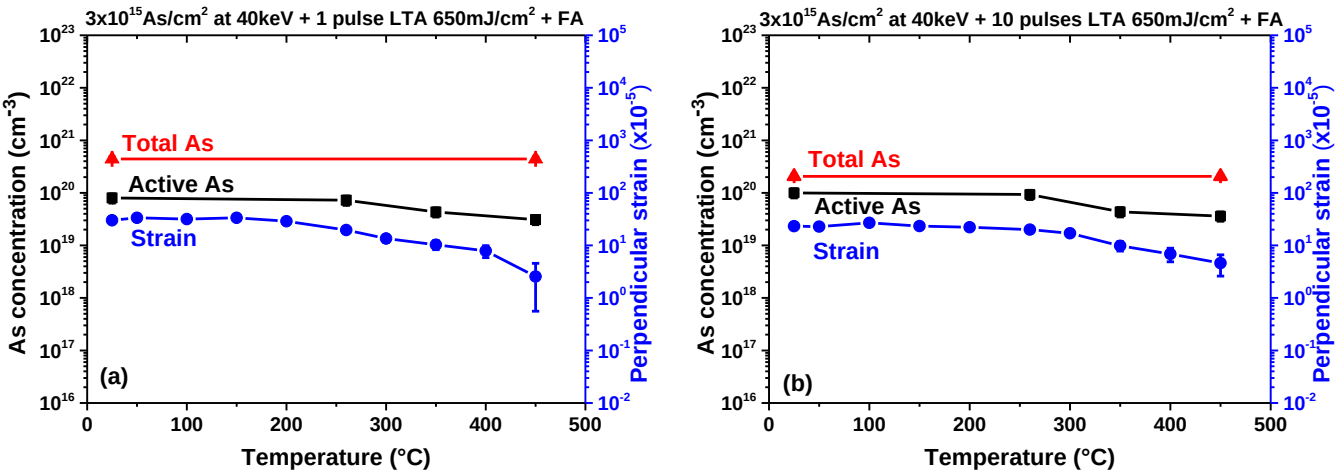

Fig.3.32 Temperature evolution of the perpendicular strain (circles) as well as chemical (triangles) and carrier (squares) concentration as measured by *in situ* HRXRD, SIMS and SRP respectively on the samples implanted with 3×10^{15}As/cm^2 at 40keV after LTA at 650mJ/cm^2 with single- (a) and multi-pulse (b).

Fig.3.32 clearly shows that both the electrical activation and the strain remain constant up to about ~250°C. Above this temperature they decrease monotonously by increasing the temperature. It can also be noted that the electrical activation tends to flatten at temperatures above ~350°C whereas the strain continues to decrease with a much steeper trend than the active As concentration. This is quite surprising considering that (substitutional) active As and clustered As have atomic lattice volume modification parameters, ΔV_{As_s} and ΔV_{As_cl} respectively of the same sign, as estimated in the previous section. Thus, the strain is expected to decrease with trend less steep than the active As. The observed opposite behavior indicates that ΔV_{As_cl} is decreasing by increasing the temperature. The temperature evolution of the clustered As lattice volume modification ΔV_{As_cl} is extracted, and reported in fig. 3.33 under the assumption that substitutional As atoms give always the same contribution to $\varepsilon_\perp$ as estimated in the previous section, i.e. ΔV_{As_s}=+8.8±0.6Å^3.

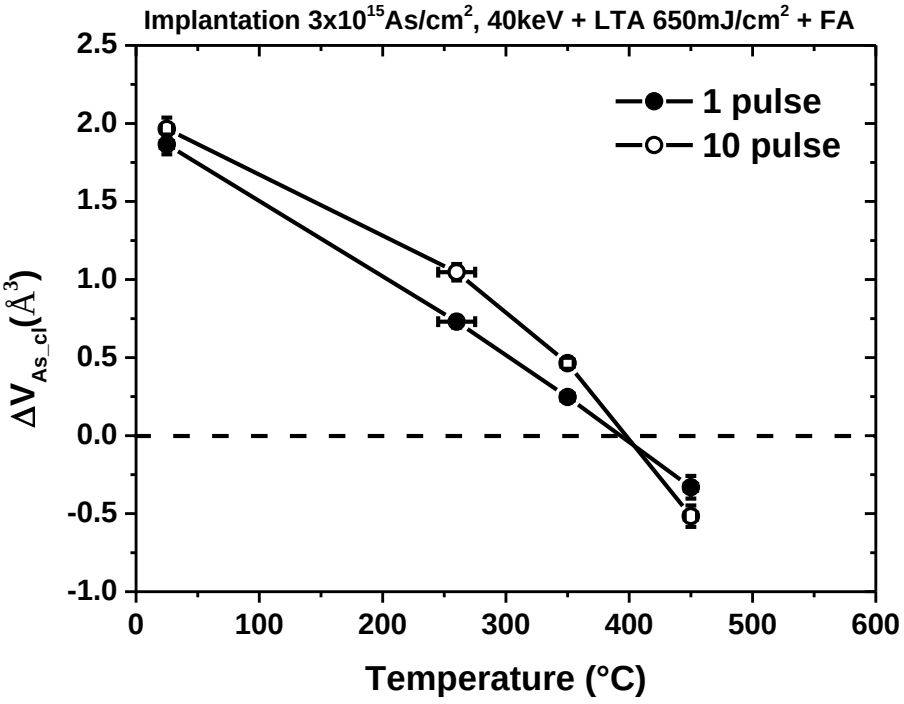

Fig.3.33 Temperature evolution of the lattice volume modification per clustered As atom obtained from *in situ* RCs on the samples implanted with 3×10^{15}As/cm^2 at 40keV after LTA at 650mJ/cm^2 with single- (closed symbols) and multi-pulse (open symbols).

A gradual decrease is observed of the initial value of ΔV_{As_cl}=+2.00±0.04Å^3 by increasing the temperature down to -0.42±0.09Å^3 after annealing at 450°C. Therefore, the growth of the clusters observed by APT in association with the thermal deactivation, is found also to change the nature of the clusters which pass from inducing compressive strain after LTA, to inducing tensile strain after additional thermal annealing at 450°C. Such a strain reversal is remarkable, and suggests that the increase of the number of As atoms per cluster during the growing is associated also with an increase in the amount of vacancies. This is reasonable by considering that DFT calculations report unfavorable As-As binding energy in the NN configuration, unless mediated by interaction with vacancies [Chroneos2007], which necessarily implies a larger quantity of Vs in the clusters.

In summary all the observation bring to the following picture of As deactivation mechanism under post annealing: free As diffuses most likely trough the AsV mechanism, but the high density of clusters still present in the sample is a very efficient trap for the mobile species that prevents the broadening of the overall profile. Diffusion and recapture onset start at about 260C° and bring to a growth of the cluster size without a significant variation of their density (no Oswald ripening). In the temperature range between 260° and 450 C° cluster grow and change their structure most likely by including more vacancies as deduced by evolution of specific volume.

3.5.2 Boron

Preliminary investigation of B samples was also performed. With the aim of dissolving the B clusters, so as to improve the electrical activation of the dopant, the sample with 1×10^{16}B/cm^2 at 20keV and then laser irradiated for 1 pulse was annealed, using a conventional FA, at 600°C for 1h, in N_2 atmosphere. It is worth to note that the selected temperature, i.e., 600°C, is quite high for Ge, indeed it corresponds to the temperature of ~940°C for Si, if referred to the respective melting temperatures of the two materials (the melting temperature of Ge is lower with respect to Si). The SRP is reported in fig.3.34 with open circles, together with the carrier concentration profiles shown above. It is clear that the applied thermal budget is not able to dissolve the B clusters, which are stable up to 600°C.

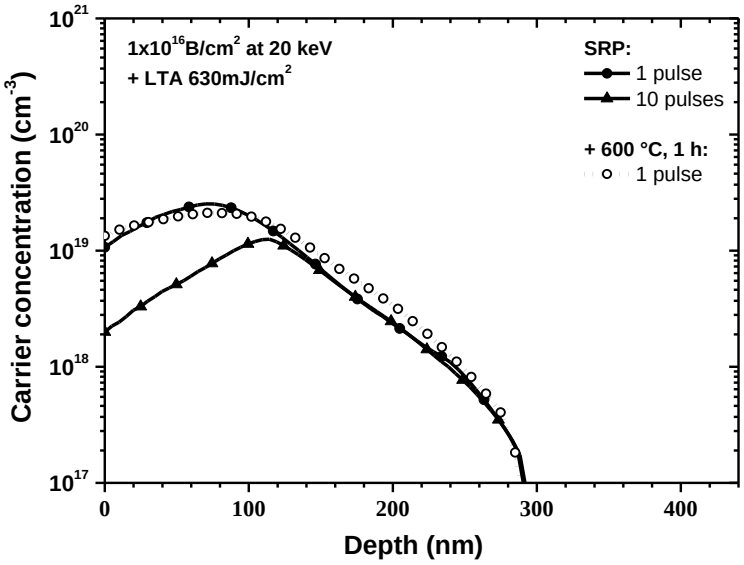

Fig.3.34 Carrier concentration profiles as measured by SRP after high B fluence implant plus LTA for 1 pulse (closed circles) or 10 pulses (closed triangles). Open circles indicate the carrier concentration profile in a sample subjected to LTA for 1 pulse plus a thermal annealing at 600°C for 1h.

From another point of view, B-doped Ge by LTA in the melting regime displayed a noteworthy thermal stability, despite the extremely low equilibrium solubility of B of 1×10^{18}B/cm^{-3}. Hence, indicating that *p*-type doping of Ge up to higher concentration by means of LTA on B-Ge system is still quite promising, if oxygen interaction and dopant precipitation issues are overcome.

3.5.3 Conclusions

In conclusion, an experiment on post-LTA by conventional thermal processing has been performed. An electrical deactivation of the Ge sample initially doped beyond the solid solubility (up to ~1×10^{20}As/cm^3) by ion-implantation and LTA was investigated by combining SRP, SIMS, APT and *in situ* HRXRD measurements.

As a result, we observed that temperature of ~350°C is sufficient to reduce the carrier concentration below ~4×10^{19}As/cm^2, i.e. under the As solid solubility in Ge (8×10^{19}As/cm^2), so suppressing the beneficial effects of LTA in terms of electrical activation. In addition, no redistribution of the dopant up to 450°C is detected, in spite of the high extrinsic regime. Those results are interpreted on the basis of inhibition of As long range diffusion by clusters nucleated just after LTA.

Consistently, APT measurements on the post-processed sample up to 450°C detected a clustering growth, which is suggested to be vacancy-assisted, if also HRXRD data are cross-checked. In particular, the extracted perpendicular strain profiles clearly indicate a reduction in the ΔV_{As_cl} contribution down to negative values at 450°C. Therefore, the clusters are most likely fed by the AsV^- species and so they prevent effectively As diffusion to occur, being very efficient sink for AsV and avoiding the mobile specie to escape from the doped zone

Besides, the high fluence B-implanted sample were subjected to an additional annealing at 600°C for 1 h, observing no significant changes in the SRP profile. Thus, the thermal stability of the inactive B complexes, but also of the active dopant, are demonstrated up to this temperature.

CONCLUSIONS

In this thesis the doping of germanium by LTA in the melting regime has been presented by reporting the experimental results on B- and As-implanted sample. In both of the case, two different fluences have been tested: namely B-implantation at 20keV with 1×10^{15} or 1×10^{16}B/cm^2, while As-implantation at 40keV with 2×10^{14}As/cm^2 or 3×10^{15}As/cm^2. Consequently, laser irradiations at 630mJ/cm^2 with 1, 3 and 10 pulses on B-, as well as at 530mJ/cm^2 or at 650mJ/cm^2 both in single and multipulse regime on As-implanted samples have been performed.

Similarly to silicon, accumulation of boron at the maximum melt depth has been observed and it has been effectively simulated by a unique diffusion mechanism, involving two diffusivity states. Therefore, the indirect observation of the second liquid phase formation during strong undercooling conditions is extended to germanium, thus confirming a general dependence on the crystallization into tetrahedral network. On the other hand, LTA on Ge implanted with arsenic results into a favorable box-like redistribution, which is similarly modeled by the anomalous l-Ge property. However, in this system the pile-up at the maximum melt depth is found hindered by the low equilibrium segregation coefficient of As, thus suggesting an intrinsic limitation on the melting laser annealing for dopants with smaller tetrahedral radii, such as boron.

Furthermore, the studies demonstrated that LTA is a more promising technique for the *n*-type doping, since a new record for arsenic activation (~1×10^{20}As/cm^3) has been achieved, without neither appreciable dose loss, nor formation of extended defect. Nevertheless, issues on partial activation and on the saturation in the active level still needs to be overcome. Instead, boron suffers of deactivation correlated to oxygen contaminants penetrating from the surface oxide as a result of laser irradiation. The former has been demonstrated by an increase of boron activation after GeO_2 etching, and the latter by changes in oxygen diffusion with respect to undoped Ge.

Residual strain after LTA on un- and implanted samples has been characterized by HRXRD as well as modeled by independent contribution of substitutional and clustered dopant in a wide range of experimental conditions, i.e. on varying implantation fluence, laser energy and number of pulses. The

developed methodology, combined with numerous DFT calculations available in the literature, suggests that LTA drives oxygen into interstitial configuration inside the unimplanted Ge, but its arrangement changes when dopants are introduced. In particular, the direct interaction with boron and with a vacancy supersaturation established through AsV slow recombination are proposed as explanations for strain compensation both for the oxygen and for the dopants. Beside, an intriguing parallelism between Si and Ge has been evidenced for the two investigated elements on clustering with point-defects, which also supports the hypothesis of V-mediated clustering of As and the formation of B-B precipitates in the pile-up region.

In addition, the same kinetic estimations also predict that an AsV-mediated deactivation takes over at higher fluence, thus assigned to the saturation trend observed in these samples. This hypothesis has been investigated by APT measurements, which have detected a significant amount of inactive As in the form As-rich clusters (about 2%), in agreement with the respective electrical activation, if random migration of the mobile dopant defect pair is assumed.

Last but not least, the compatibility of LTA with further processing steps has been tested. Additional thermal anneals have resulted ineffective in changing the active B concentration up to temperatures of 600°C for 1 hour. In the case of arsenic, even a loss of the laser annealing effect by favoring deactivation and growing of the As-V clusters is obtained above 350°C.

Despite the encouraging results, especially the temperature response prevents the laser annealing to be implemented in the actual large scale fabrication of ultra-shallow junctions before addressing and solving such issue. However, this study suggests that the residual vacancy defects after LTA are a possible cause for the quick As deactivation during post-LTA annealing. Thus, attempts can be made to optimize the LTA process, e.g. by changing the pulse duration and/or the pre-heating conditions. The resulting variations in the liquid/solid regrowth rate might alter the point defect generation during LTA and thus improve the As stability. The results presented in this work represent a step forward in the description of the phenomena involved in melting LTA, in particular for the previously unexplored B- and As-doping of Ge. As well as they provide a solid starting point for future studies.

Future perspectives include investigations on the effects of LTA on other elements implanted in Ge, e.g. phosphorous or Aluminum. P already showed good results after LTA, but his behavior has not been described in detail yet. Al has not been explored at all in Ge under laser annealing.

APPENDIX

EXPERIMENT ON LIQUID SELF-DIFFUSION OF SILICON UNDER MELTING LASER THERMAL ANNEALING AND ITS ROLE ON DOPANT ACTIVATION

The liquid phase behavior of tetrahedral network material has recently attracted many fundamental works,[Sastry2003, Katayama2000, Erringtон2001] particularly since the discovery of their liquid-liquid phase transition in the undercooled regime.[Franzese2000] Among the tetrahedral network materials, the most studied is indubitably silicon, which generally represent a prototype for many basic physic experiments and it is still the most used semiconductor. In this framework, the anomalous diffusion effects of dopants during LTA in Si are explained on the basis of two (fast and slow) diffusivity states the impurity introduced, correlated to the metallic and the covalent bond state of the matrix, respectively.[Fisicaro2013] In particular, the phase-field simulations predict that the strongest undercooling region is expected close to the maximum melt depth, where the pile-up is observed. Consistently, by studying the phenomena involved in the doping by melting laser annealing, the first evidence of similar anomalous redistribution effects also in Ge was given in this thesis, which confirms the importance of deeply understanding the transport properties of the liquid matrix, and especially if the pile-up phenomenon at the maximum melt depth wants to be quantitatively simulated.

However, not every dopant display an anomalous redistribution effect, depending on the concurrent tendency of the effective segregation coefficient to its equilibrium value k_0 in this region, which can hinder the pile-up for low value of k_0. So, in order to fully understand the anomalous diffusion of the impurities close to the l/s interface, fundamental studies are needed, so as to describe in detail the diffusion properties of the matrix itself, i.e. its self-diffusivity in this region.

In other words, if the anomalous diffusion of the dopants is due to anomalous properties of the matrix, this should be reflected also by an anomalous self-diffusion, since, k_0 of an isotope is 1 by definition, as a result of the perfect self-miscibility. Therefore, a "self-pile-up" phenomenon at the maximum melt depth should not be hindered and it would be interesting to correlate the behavior of the self-diffusion with pile-up of dopants typically showing this effect, such as boron or phosphorous.

Moreover, liquid self-diffusivity is a particularly challenging property to measure accurately due to systematic errors induced by convection and Marangoni effect, namely resulting from surface temperature gradients and temperature dependence of the surface tension.[Iida1993] It is worth noting that pulsed laser melting can minimize these phenomena, since instabilities leading to natural convection can occur if the Rayleigh number R>1700.[Roberts1966] Though, since R has a cubic dependence on the thickness of the liquid layer, the thin film geometry provides Ron the order of 10^{-11}, so making virtually impossible to establish convection currents. Besides, calculations of surface tension by using the Stokes solution for a suddenly accelerated flat plate in and infinite liquid[Roberts1966] indicates that the diffusive transport is 10^7 times faster than the Marangoni transport.

Nevertheless, atomistic simulation of Si systems are common, but there is a paucity of self-diffusion experiment, especially under laser annealing. As far as our knowledge, the only attempt is the study of Sanders and Aziz of 1999,[Sander1999] where the averaged liquid self-diffusivity was determined by performing pulsed laser annealing on ^{30}Si-isotope self-implanted sample. However, the melt depth has not been optimized in order to characterize the diffusion behavior close to l/s interface, namely being to very close to the implant range and uniform temperature has been assumed in the simulation of the SIMS profiles (figs.A.1 and A.2).

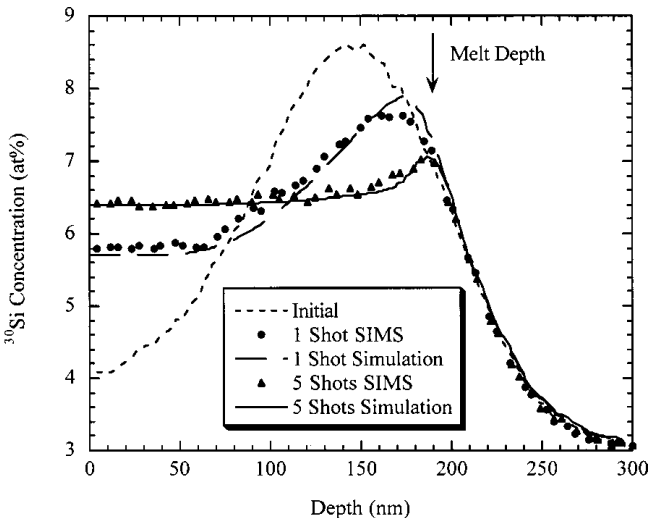

Fig.A.1 Agreement between experimental SIMS concentration profile and simulated diffusion profiles for one shot and five shots. The melt depth is shown to be approximately 190nm.[Sander1999]

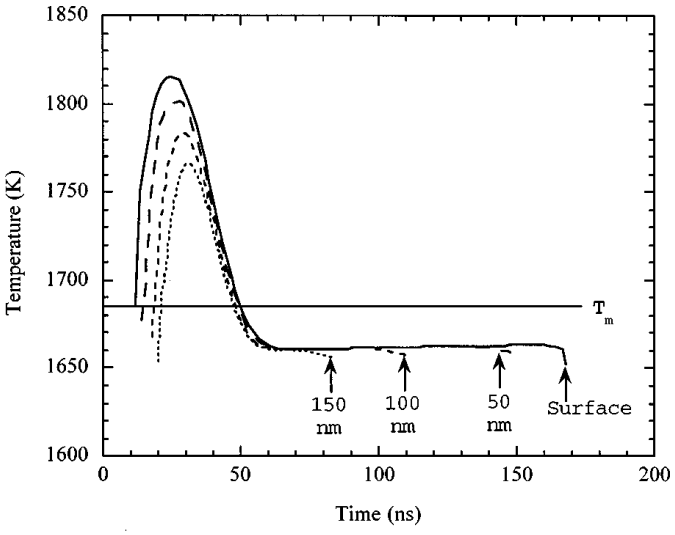

Fig.A.2 Liquid temperature temporal profiles at various depths determined by heat-flow calculations. The surface (solid line) melts first and freezes last, while material at 150nm depth (dotted curve) melts later and freezes earlier. When the solidification front passes a given depth, the corresponding temperature suddenly drops from the essentially steady-state value of 1660K during solidification (60–170ns).[Sander1999]

As specifically B has been extensively studied and modeled,[Fisicaro2013] an experiment to study the self-diffusion an its correlation with the pile-up of B in Si has been designed during this three years of Ph.D. Currently, the sample have been already grown and processed and they are going to be characterized soon.

In particular, by MBE the sample has been grown as follows: an inner 10nm-thin layer of natural abundance Si between two ^{28}Si layers at 40nm from the surface and 200nm from the substrate, respectively (fig.A3). Then, the sample was cut and a part was implanted with boron. Consequently, both the as-grown and the as implanted sample have been processed with LTA by means of a XeCl laser (λ=308nm) optimizing different energies (corresponding to different melt depths). Precisely, the samples have been irradiated with different energy densities corresponding to different maximum melt depths, both in single and multi-pulse regimes (fig.A4).

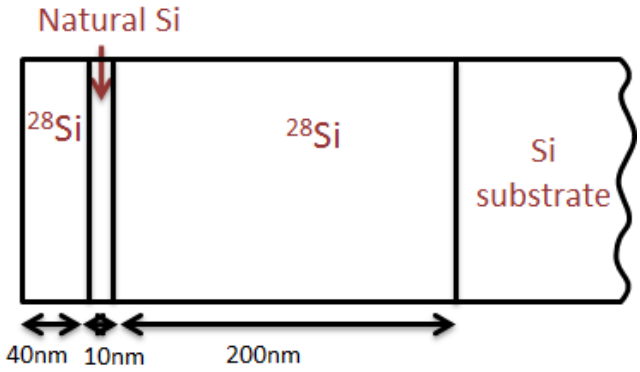

Fig.A3 Scheme of the MBE as-grown sample

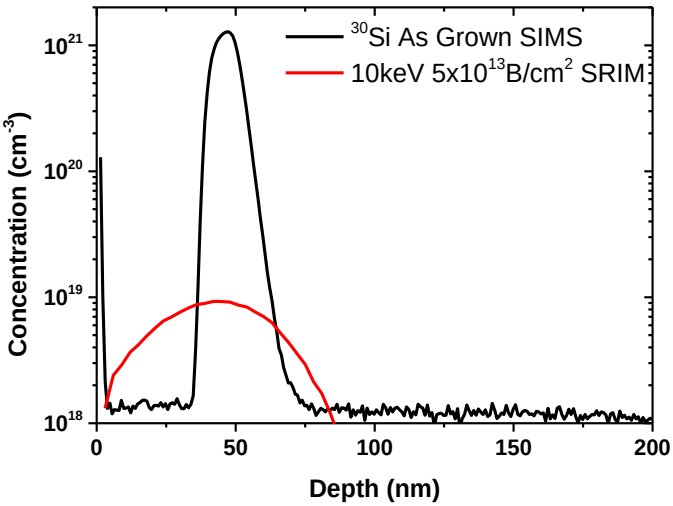

Fig.A4 SIMS characterization of the as-implanted sample (black line). The SRIM simulation of the implantation with 10keV, $5x10^{13}$ B/cm^2, 7° tilt, 30° twist is also reported (red line), together with the sketch of the expected maximum melt depth as a result of the optimized LTA processing.

^{30}Si and B depth profiles after LTA will give important information on the transport properties and on the nature of the liquid phase close to the Si melting temperature and on their link with the anomalous redistribution of B in the liquid phase.

LIST OF PUBLICATIONS

Publications in Peer-Reviewed Scientific Journals

- **B-doping in Ge by excimer laser annealing**

  G. Impellizzeri, E. Napolitani, S. Boninelli, G. Fisicaro, M. Cuscunà, R. Milazzo, A. La Magna, G. Fortunato, F. Priolo, and V. Privitera

  *Journal of Applied Physics, **113**, 113505, (2013)*

- **Role of oxygen on the electrical activation of B in Ge by excimer laser annealing**

  G. Impellizzeri, E. Napolitani, R. Milazzo, S. Boninelli, M. Cuscunà, G. Fisicaro, A. La Magna, G. Fortunato, F. Priolo, and V. Privitera

  *Physica Status Solidi (a), **211**, 122-125, (2014)*

- **Role of oxygen on the electrical activation of B in Ge by excimer laser annealing**

  R. Milazzo, E. Napolitani, G. Impellizzeri, G. Fisicaro, S. Boninelli, M. Cuscunà, D. De Salvador, M. Mastromatteo, M. Italia, A. La Magna, G. Fortunato, F. Priolo, V. Privitera, and A. Carnera

  *Journal of Applied Physics, **115**, 053501, (2014)*

Paper in Preparation for Peer-Reviewed Scientific Journals

- **Dopant and impurity interactions during melting Laser Thermal Annealing in Ge**

  R. Milazzo, E. Napolitani, G. Impellizzeri, M. Cuscunà, D. Piccinotti, D. De Salvador, M. Mastromatteo, A. La Magna, G. Fortunato, A. Portavoce, D. Mangelinck, F. Priolo, V. Privitera, and A. Carnera

- **Thermal stability of As-doped Ge by ion-implantation and Laser Thermal Annealing**

  R. Milazzo, E. Napolitani, G. Impellizzeri, M. Cuscunà, D. Piccinotti, D. De Salvador, M. Mastromatteo, M. Italia, G. Fortunato, A. Portavoce, D. Mangelinck, F. Priolo, V. Privitera, and A. Carnera

REFERENCES

[Atalla1959] M. M. Atalla, E. Tannenbaum and E. J. Scheibner, Bell Syst. Tech. J. **38**, 749–783 (1959);

[Benourhazi1992] K. Benourhazi, J. P. Ponpon, Nucl. Instrum. Methods B **71**, 406, (1992);

[Bisognin2006] G. Bisognin, D. De Salvador, E. Napolitani, A. Carnera, E. Bruno, S. Mirabella, F. Priolo and A. Mattoni, Semicond. Sci. Technol., **21**, L41, (2006);

[Bisognin2007] G. Bisognin, D. De Salvador, E. Napolitani, M. Berti, A. Carnera, S. Mirabella, L. Romano, M. G. Grimaldi, and F. Priolo, J. Appl. Phys. **101**, 093523 (2007);

[Bisognin2010] G. Bisognin, S. Vangelista, M. Berti, G. Impellizzeri, M. G. Grimaldi, J. Appl. Phys. **107**, 103512, (2010);

[Boninelli2012] S. Boninelli, G. Impellizzeri, A. Alberti, F. Priolo, F. Cristiano, and C. Spinella, Appl. Phys. Lett. **101**, 162103 (2012);

[Borot2007] G. Borot, L. Rubaldo, L. Clement, R. Pantel, D. Dutartre, K. Kuitunen, J. Slotte, F. Tuomisto, X. Mescot, M. Gri and G. Ghibaudo, J. Appl. Phys. **102**, 103505, (2007);

[Bracht2007] H. Bracht, H. H. Silvestri, I. D. Sharp, and E. E. Haller, Phys. Rev. B **75**, 035211, (2007);

[Brotzmann2008] S. Brotzmann, H. Bracht, J. Lundsgaard Hansen, A. Nylandsted Larsen, E. Simoen, E. E. Haller, J. S. Christensen, and P. Werner, Phys. Rev. B **77**, 235207, (2008);

[Bruno2010] E. Bruno, G. G. Scapellato, G. Bisognin, E. Carria, L. Romano, A. Carnera, and F. Priolo, J. Appl. Phys. **108**, 124902 (2010);

[Bruno2012] E. Bruno, G. G. Scapellato, A. La Magna, M. Cuscuna, E. Napolitani, S. Boninelli, F. Priolo, G. Fortunato, and V. Privitera, Appl. Phys. Lett. **101**, 172110 (2012);

[Chathoth2009] S. M. Chathoth, B. Damaschke, T. Unruh, and K. Samwer, Appl. Phys. Lett. **94**, 221906 (2009);

[Chroneos2007] A. Chroneos, R. W. Grimes, B. P. Uberuaga, S. Brotzmann, and H. Bracht, Appl. Phys. Lett. **91**, 192106, (2007);

[Chroneos2012] A. Chroneos, E. N. Sgourou, and C. A. Londos, J. Appl. Phys. **112**, 073706, (2012);

[Chroneos2014] A. Chroneos, and H. Bracht, Appl. Phys. Rev. **1**, 011301, (2014);

[Chui2003] C. O. Chui, K. Gopalakrishnan, P. B. Griffin, J. D. Plummer, and K. C. Saraswat, Appl. Phys. Lett, **83**, 3275, 2003;

[ClarysseAPL1990] T. Clarysse, W. Vandervorst, and A. Casel, Appl. Phys. Lett. **57**, 2856, (1990);

[Clarysse2006] T. Clarysse, P. Eyben, T. Jannsens, I. Hoflijk, D. Vanhearen, A. Satta, M. Meuris, W. Vandervorst, J. Bogdanowicz, and G. Raskin, J. Vac. Sci Tecnol. B **24**, 381 (2006);

[Clays2007] C. Clays and E. Simoen, Germanium-Based Technologies - From Materials to Devices (Elsevier, Amsterdam, 2007);

[Clays2008] C. Claeys, E. Simoen, K. Opsomer, D. P. Brunco, and M. Meuris, Mater. Sci. Eng. B, **49** 154–155, (2008);

[Contreras1985] G. Contreras, L. Tapfer, A. K. Sood, and M. Cardona, Phys. Stat. Sol. (b), **131**, 475, (1985);

[Coutinho2000] J. Coutinho, R. Jones, P. R. Briddon, S. Öberg, Phys. Rev. B **62**, 10824, (2000);
[Cowern1992] N. E. B. Cowern, G. F. A. van de Walle, P. C. Zalm, and D. J. Oostra Phys. Rev. Lett. **69**, 116, (1992);
[Edwards1968] W. D. Edwards, J. Appl. Phys. **39**, 1784 (1968);
[Errington2001] J. R. Errington, and P. G. Debenedetti, Nature, **409**, 318-321, (2001);
[Fisicaro2011] G. Fisicaro, A. La Magna, G. Piccitto, V. Privitera, Microelectronic Engineering **88**, 488-491, (2011);
[Fisicaro2013] G. Fisicaro, K. Huet, R. Negru, M. Hackenberg, P. Pichler, N. Taleb, and A. La Magna, Phys. Rev. Lett. **110**, 117801, (2013);
[Fistul2004] V. I. Fistul, *Impurities in Semiconductors: Solubility, Migration, and Interactions* (CRC Press, Florida, 2004), p.157.
[Franzese2000] G. Franzese, G. Malescio, A. Skibinsky, S. V. Buldyrev, and H. E. Stanley, Nature **409**, 692-695, (2000);
[Gao1988] Y. Gao, J. Appl. Phys. **64**, 3760 (1988)
[Hattangady1988] S. V. Hattangady, G. G. Fountain, E. H. Nicollian, R. J. Markunas, J. Appl. Phys. **63**, 68-74 (1988);
[HellingsEESL2011] G. Hellings, E. Rosseel, E. Simoen, D. Radisic, D. Hjorth Petersen, O. Hansen, P. Folmer Nielsen, G. Zschätzsch, A. Nazir, T. Clarysse, W. Vandervorst, Th. Y. Hoffmann, and K. De Meyer, Electrochem. Solid-State Lett. **14**, H39 (2011).
[HellingsME2011] G. Hellings, E. Rosseel, T. Clarysse, D. H. Petersen, O. Hansen, P. F. Nielsen, E. Simoen, G. Eneman, B. De Jaeger, T. Hoffmann, K. De Meyer, and W. Vandervorst, Microelectron. Eng. **88**, 347-350 (2011);
[Heo2006] S. Heo, S. Baek, D. Lee, M. Hasan, H. Jung, J. Lee, and H. Hwang, Electrochem. Solid State Lett. **9(4)**, G136 (2006);
[Huet2009] K. Huet, G. Fisicaro, J. Venturini, H. Besaucèle, and A. La Magna, Appl. Phys. Lett. **95**, 231901 (2009);
[Hüger2008] E. Hüger, U. Tietze, D. Lott, H. Bracht, D. Bougeard, E. E. Haller, and H. Schmidt, Appl. Phys. Lett. **93**, 162104, (2008);
[Hyde2011] J. M. Hyde, E. A. Marquis, K. B. Wilford, and T. J. Williams, Ultramicroscopy, **111**(6), 440–447, (2011);
[Iida1993] T. Iida, and R. I. L. Guthrie, *The Physical Properties of Liquid Metals*, p. 199, (Clarendon, Oxford, 1993);
[Impellizzeri2009] G. Impellizzeri, S. Mirabella, E. Bruno, A. M Piro, and M. G. Grimaldi, J. Appl. Phys. **105**, 063533, (2009);
[Impellizzeri2011] G. Impellizzeri, S. Boninelli, F. Priolo, E. Napolitani, C. Spinella, A. Chroneos, and H. Bracht, J. Appl. Phys. **109**, 113527 (2011);
[ioffe.ru] Ioffe Physico-Technical Institute of St. Petersburg, Semicond. Physical Properties of Semiconductors (online), url: http://www.ioffe.ru/SVA/NSM/Semicond/Ge/mechanic.html;
[ITRS2013] ITRS, 2013 edition (online) url: http://www.itrs.net;
[Janssens2006] T. Janssens, C. Huyghebaert, D. Vanhaeren, G. Winderickx, A. Satta, M. Meuris, and W. Vandervorst, J. Vac. Sci. Technol. B **24**, 510 (2006);
[Jones1981] K. S. Jones, and E. E. Haller J. Appl. Phys. **61**, 2469, (1981);
[Kahng1991] D. Kahng, Technical memorandum (Bell Laboratories, 16 January 1961); reprinted in Sze, S. M. (ed.) *Semiconductor Devices: Pioneering Papers* 583–596, World Scientific Publishing, (1991);

[Katayama2000] Y. Katayama, T. Mizutani, W. Utsumi, O. Shimomura, M. Yamakata, and K. Funakoshi, Nature **403**, 170-173, (2000);
[Koffel2013] S. Koffel, P. Pichler, J. Lorenz, G. Bisognin, E. Napolitani and D. De Salvador, IEEE-ESSDERC, 206-209, (2013);
[LaMagnaAPL2004] A. La Magna, P. Alippi, V. Privitera, S. Scalese, S. Pannitteri, G. Fortunato, M. Camalleri, Appl. Phys. Lett. **84**, 4738, (2004);
[LaMagnaJAP2004] A. La Magna, P. Alippi, V. Privitera, G. Fortunato, M. Camalleri, B. G. Svensson, J. Appl. Phys. **95**, 4806, (2004);
[LaMagna2007] A. La Magna, V. Privitera, G. Fortunato, M. Cuscunà, B. G. Svensson, E. Monakov, K. Kuitunen, J. Slotte, and F. Tuomisto, Phys. Rev. B **75**, 235201 (2007);
[Lopez2007] P. Lopez, L. Pelaz, L. A. Marqués, I. Santos, and J. A. Van den Berg, *Proceedings of the 6th Spanish Conference on Electron Devices*, IEEE 1-4244-0869-5/07 (2007);
[Magee2000] C. W. Magee, D. Jacobson, and H.-J. Gossmann, J. Vac. Sci. Technol. B **18**, 489, (2000);
[Mannino2005] G. Mannino, V. Privitera, A. La Magna, E. Rimini, E. Napolitani, G. Fortunato, and L. Mariucci, Appl. Phys. Lett. **86**, 051909 (2005);
[Marquis2010] E. A. Marquis and J. M. Hyde; Mat. Sci. Eng. R. **69**, 37-62, (2010);
[McDonald1975] P. J. McDonald, and D. W. Palmer, Inst. Phys. Conf. Ser., **23**(7), 504, (1975);
[Mirabella2008] S. Mirabella, G. Impellizzeri, A. M. Piro, E. Bruno, M. G. Grimaldi, Appl. Phys. Lett. **92**, 251909, (2008);
[Mistry2007] K. Mistry, C. Allen, C. Auth, B. Beattie, D. Bergstrom, M. Bost, M. Brazier, M. Buehler, A. Cappellani, R. Chau, C. H. Choi,G. Ding, K. Fischer, T. Ghani, R. Grover, W. Han, D. Hanken, M. Hattendorf, J. He, J. Hicks , R. Huessner, D. Ingerly, P. Jain, R. James, L. Jong, S. Joshi, C. Kenyon, K. Kuhn, K. Lee, H. Liu, J. Maiz, B. McIntyre, P. Moon, J. Neirynck, S. Pae, C. Parker, D. Parsons, C. Prasad, L. Pipes, M. Prince, P. Ranade, T. Reynolds, J. Sandford, L. Shifren, J. Sebastian, J. Seiple, D. Simon, S. Sivakumar, P. Smith, C. Thomas, T. Troeger, P. Vandervoorn, S. Williams, K. Zawadzki, Tech. Digest IEEE Electron Devices Meet. 247–250, (2007);
[Monakov2005] E. V. Monakhov, B. G. Svensson, M. K. Linnarsson, A. La Magna, M. Italia, V. Privitera, G. Fortunato, M. Cuscunà, and L. Mariucci, Appl. Phys. Lett. 87, 192109, (2005);
[Moody2008] M. P. Moody, L. T. Stephenson, A. V Ceguerra, and S. P. Ringer, Microsc. Res. Tech., **71**(7), 542–50, (2008);
[Moore2003] Moore, G. E., Digest Tech. Papers Int. Solid-State Circuits Conf. IEEE, 20-23, (2003);
[Morin1954] F. J. Morin and J.P. Maita, Phys. Rev. **94**, 1525 (1954);
[Napolitani2010] E. Napolitani, G. Bisognin, E. Bruno, M. Mastromatteo, G. G. Scapellato, S. Boninelli, D. De Salvador, S. Mirabella, C. Spinella, A. Carnera, and F. Priolo, Appl. Phys. Lett. **96**, 201906, (2010);
[Olesinski1985] R. W. Olesinski and G. J. Abbaschian, Bull. Alloy Phase Diagrams **6**(3), 250–254 (1985);
[Ong2006] K. K. Ong, K. L. Pey, P. S. Lee, A. T. S. Wee, X. C. Wang, and Y. F. Chong, Appl. Phys. Lett. **89**(17), 172111, (2006);
[Pillarisetty2011] R. Pillarisetty, Nature, **479**, 324-328, 2011;
[Poate1982] J. M. Poate and J. W. Mayer, *Laser Annealing of Semiconductors*, (Academic Press, New York, 1982);
[Poon2005] C. H. Poon, L. S. Tan, B. J Cho, A. Y. Du, J. Electrochem. Soc. **152**, G-895, (2005);
[Prabhakaran1995] K. Prabhakaran and T. Ogino, Surf. Sci. **325**, 263 (1995);
[Privitera1993] V. Privitera, W. Vandervorst, and T. Clarysse, J. Electrochem. Soc. **140**, 262 (1993);

[Privitera2007] V. Privitera, A. La Magna, G. Fortunato, L. Mariucci, M. Cuscunà, M. Camalleri, A. Magrì, B. G. Svensson, and F. Simon, IEEE Trans. Electron. Dev. **54**, 852, (2007);
[Pyykkö2012] Pyykkö, Phys. Rev. B **85**, 024115, (2012);
[Rimini1995] E. Rimini, *Ion-implantation: Basics to Device Fabrication* (Kluwer Academic Publishers, Boston, 1995), p. 102;
[Roberts1966] P. H. Roberts, *Non-Equilibrium Thermodynamics: Variational Techniques and Stability*, p. 126, (University of Chicago Press, Chicago, 1966);
[Romano2013] L. Romano, G. Impellizzeri, M. G. Grimaldi, Materials Letters **96**, 74-77, (2013);
[Sander1999] P. G. Sanders, and M. J. Aziz, , J. Appl. Phys. **86**, 4258 (1999);
[Sastry2003] S. Sastry, and C. A. Angell, Nat. Mater. **2**, 739-743, (2003);
[Satta2005] A. Satta, E. Simoen, T. Clarysse, T. Janssens, A. Benedetti, B. De Jaeger, M. Meuris, and W. Vandervorst, Appl. Phys. Lett. **87**, 172109, (2005);
[Schueler2000] B. W. Schueler, and D. F. Reich, J. Vac. Sci. Technol. B **18**, 496, (2000);
[Simoen2006] E. Simoen, A. Satta, A. D'Amore, T. Janssens, T. Clarysse, K. Martens, B. De Jaeger, A. Benedetti, I. Hoflijk, B. Brijs, M. Meuris, and W. Vandervorst, Mater. Sci. Semicond. Process. **9**, 634-639 (2006);
[Simoen2012] E. Simoen, J. Mitard, G. Hellings, G. Eneman, B. De Jaeger, L. Witters, B. Vincent, R. Loo, A. Delabie, S. Sioncke, M. Caymax, and C. Claeys, Mater. Sci. Semicond. Process. **15**, 588 (2012);
[Stephenson2007] L. T. Stephenson, M. P. Moody, P.V. Liddicoat and S. P. Ringer; Microsc. Microanal. **13**, 448-463, (2007);
[Suh2005] Y. S. Suh, M. S. Carroll, R. A. Levy, G. Bisognin, D. De Salvador, M. A. Sahiner, and C. A. King, IEEE Trans. Electron. Devices., 52, 2416, (2005);
[Treberspurg2012] W. Treberspurg, T. Bergauer, M. Dragicevic, J. Hrubec, M. Krammer and M. Valentan, J. Instrum., 7 (2012);
[Trumnore1960] F. A. Trumbore, Bell Syst. Tech. J. **39**, 205-233, (1960);
[Tsouroutas2006] P. Tsouroutas, D. Tsoukalas, A. Florakis, I. Zergioti, A. A. Serafetinides, N. Cherkashin, B. Marty, and A. Claverie, Mater. Sci. Semicond. Process. **9**, 644 (2006);
[Tsouroutas2009] P. Tsouroutas, D. Tsoukalas, I. Zergioti, N. Cherkashin, and A. Claverie, J. Appl. Phys. **105**, 094910 (2009);
[Uppal2001] S. Uppal, A. F. W. Willoughby, J. M. Bonar, A. G. R. Evans, N. E. B. Cowern, R. Morris, and, M. G. Dowsett, J. Appl. Phys. **90**, 4293, (2001);
[Van den Berg2001] J. A. Van den Berg, S. Zhang, S. Whelan, D. G. Armour, R. D. Golberg, P. Bailey, and T. C. Q. Noakes, Nucl. Instrum. Methods Phys. Res. B **183**, 154 (2001);
[Werner1985] M. Werner, H. Mehrer, and H. D. Hochheimer, Phys. Rev. B **32**, 3930, (1985);
[Wheeler1992] A. A. Wheeler, W. J. Boettinger, G. B. McFadden, Phys Rev. A **45**, 7424 (1992);
[Wood1981] R. F. Wood, J. R. Kirkpatrick, and G. E. Giles, Phys. Rev. B **23**, 5555, (1981);
[Wormington1999] M. Wormington, C. Panaccione, K. M. Matney, and K. Bowen, Philos.Trans. R. Soc. London, Ser. A **357**, 2827 (1999);

ACKNOWLEDGMENTS

Several individuals have provided support and guidance that contributed to the completion of the work within this dissertation. I would like to thank my supervisor, Prof. Enrico Napolitani for his guidance and patience throughout the duration of my work in the last three years and my co-supervisor, Prof. Davide De Salvador, for the knowledge he taught me, his willingness to answer my questions and the coffee provided at the conference. I am also grateful to Massimo Mastromatteo for trash-music competitions, for scientific and to any other discussion. He has been my example for three years. I need to thank Virginia Boldrini for her medicines provided in the most critical moment and Adriana Schiavon for the recharging breaks through coffee and chocolate. Thanks to other colleagues that create a pleasant work environment with jokes and parties together, among them I would like to the LaFSI team for their parties where it was an honor for me to be invited. Last but not least, I wish to thank Renzo Storti and Luca Bacci for their technical expert assistance and help.

I would like to thank my coworkers in Catania, Roma and Marseille for their precious contribution. Among them I am grateful to Giuliana Impellizzeri for the implantations, Massimo Cuscunà and Guglielmo Fortunato for the laser annealing, Giuseppe Fisicaro and Antonino La Magna for the simulations, Simona Boninelli for TEM, Marcus Italia for SRP, Alain Portavoce and Dominique Mangelinck for the APT measurements. In addition, I would like to thank Proff. Francesco Priolo, Vittorio Privitera and Alberto Carnera for their supervising.

Finally, I would also like to thank the students that had internship in our group and, particularly, the ones who had the misfortune to be victims of mine: Davide Piccinotti, Lucia Scapin and Elena Natale for their diligence and for their questions, which I tried to answer and thereby I learned a lot.

I thank warmly the friends who remained by my side through difficult hours of my life, especially in the last months. I do not name anyone in particular, because I cannot name them all here. However, I consider myself justified in making an exception in the case of Alicja. Fate gave me the happiness of being also her boyfriend and during this year she was an inexhaustible source of tenderness.